Development of Non-noble Multimetal-electrocatalysts and Application to Water-splitting Reaction

非貴金属系の多金属電気化学触媒の開発及び水分解反応への応用

Graduate School of Life Science and System Engineering

Kyushu Institute of Technology

Dissertation for the Degree of Doctor of Engineering

Author: Hanlin Chen

Supervisor: Professor Tingli Ma

April 2022

Abstract

Hydrogen evolution from electrochemical water-splitting is recognized as an effective and sustainable approach to producing hydrogen. Up to now, Ru and Pt-based electrocatalysts display superior oxygen evolution reaction (OER) and hydrogen evolution reaction (HER) activities and long-term stability. However, the high price and rare reserve on the earth limit their large-scale usage. In this thesis, we developed a series of non-noble transition multimetallic electrocatalysts. As we expected, the prepared electrocatalysts exhibited excellent both HER and OER activities. In addition, as the bifunctional electrocatalysts, the prepared electrocatalysts displayed outstanding electrochemical water-splitting activity and excellent electrocatalytic stability.

In chapter 1, the mechanism of OER and HER during the electrochemical water-splitting process, and the current development of transition metal electrocatalysts for OER and HER were introduced.

In chapter 2, a novel bimetallic heterojunction Fe_xS_y/WS_2 nanosheets (Fe_xS_y/WS_2 Ns) were prepared through interface engineering technology. The prepared Fe_xS_y/WS_2 Ns had an 8 nm thickness and a large diameter of ~1 μm. The Fe_xS_y/WS_2 Ns exhibited excellent HER activity with an overpotential of 118 mV at 10 mA cm^{-2} and a low Tafel slope of 87 mV dec^{-1}. In addition, by replacing OER with the urea oxidation reaction (UOR), the Fe_xS_y/WS_2 Ns as a bifunctional electrocatalyst could achieve energy-saving water-splitting process, in which the applied voltage could be decreased with147 mV.

In chapter 3, to further increase the electrocatalytic activity, we developed a series of non-noble transition metal electrocatalysts of unary Ni, binary NiFe, ternary NiFeCo, quaternary NiFeCoMn, and quinary NiFeCoMnCu by a facile critic acid chelating method. All the

electrocatalysts had been used as the bifunctional electrocatalysts to test the OER and HER activities. As the result, the NiFeCoMnCu high entropy alloys (NiFeCoMnCu HEAs) displayed excellent OER and HER activity with an overpotential of 240 mV and 165 mV at 10 mA cm^{-2} respectively.

In chapter 4, a high-efficiency overall electrochemical water-splitting process was enabled by the prepared NiFeCoMnCu HEAs electrocatalyst through a two-electrode system. During the water-splitting process, the NiFeCoMnCu HEAs electrocatalyst only required 1.53 V to reach 10 mA cm^{-2}. Meanwhile, almost 10 h continuous water-splitting process confirmed that the NiFeCoMnCu HEAs had an excellent stability. In addition, an electrochemical seawater-splitting reaction could also be enabled by the NiFeCoMnCu HEAs electrocatalyst with a current density of 10.5 mA cm^{-2} at 1.8 V for a continuous 10 h reaction process.

Finally, the general conclusions of this thesis and the further prospects were summarized. The strategy of mixing different active metal elements into one single electrocatalyst would provide a better solution for developing more multifunctional electrocatalysts. It is also the point we will focus on in the future.

Table of Contents

Chapter 1. Introduction

1.1 Background

With the development of human society, the overexploitation of fossil fuels to meet the increasing energy demand has led to a series of problems such as environmental degradation and energy shortage. The reduction of carbon dioxide into methane, formic acid, or hydrogen and oxygen produced by electrolysis of water through electrical energy is an ideal new energy source, which is not only conducive to solving the problem of the energy crisis but also alleviates the problem of global warming to a certain extent.

Water (H_2O) is composed of two elements, hydrogen, and oxygen. Under a suitable voltage, it will be decomposed into hydrogen and oxygen in a ratio of 2:2:1. As the early nineteenth century, Carlisel et al. used a voltaic stack to electrolyze water into gases, and one of them was identified as hydrogen for the first time.[1] As a fuel, hydrogen has an energy density three times that of gasoline, and the combustion product is water, which is non-polluting to the environment. Therefore, in the field of new energy, especially hydrogen-oxygen fuel cells, hydrogen has been widely sought after. Water electrolysis technology, which is an ideal source of hydrogen, has been continuously improved and developed since its inception. At present, the best performing water electrolysis catalysts are Ir/C and RuO_2 catalysts for oxygen evolution reaction (OER),[2-3] and Pt based catalysts for hydrogen evolution reaction (HER).[4-5] However, these noble metal catalysts are difficult to be commercialized for large-scale applications due to their high price and extremely low content on the earth. Therefore, developing a low-cost and high effective electrocatalyst for OER and HER is promised urgently.

1.2 Electrochemical water-splitting mechanism

1.2.1 The oxygen evolution reaction mechanism in alkaline solution

The oxygen evolution reaction (OER) occurs at the anode during the electrochemical water-splitting process. The total OER process follows the reaction equation, $4OH^- \rightarrow 2H_2O + O_2 + 4e^-$. According to the above equation, the OER possesses a four-electron transfer process during the electrochemical water-splitting reaction,[2-3, 6] which could exacerbate the complex degree of electrolysis and result in negligible energy during the electrochemical process. As we all know, some special species could be formed in the process of OER, such as $M\text{-}OOH^-$, $M\text{-}O^-$, and $M\text{-}OH^-$, in which the M represents the surface of the metal electrocatalyst.[6-8] The specific reaction processes of OER at the anode in alkaline solution were displayed in Figure 1.1a:

$$M + OH^- \rightarrow MOH + e^- \quad (1)$$

$$MOH + OH^- \rightarrow MO + e^- + H_2O \quad (2)$$

$$2MO \rightarrow O_2 + 2M \quad (3)$$

$$MO + OH^- \rightarrow MOOH + e^- \quad (4)$$

$$MOOH + OH^- \rightarrow O_2 + M + e^- + H_2O \quad (5)$$

The M is the surface-active metal site in the electrocatalyst. According to the above OER processes at the anode in alkaline solution, the oxygen was generated in two different ways,[9] which were the reaction processes (1), (2), and (3), while another approach was the reaction processes of (1), (2), (4) and (5). Specifically, the first reaction route generated oxygen by the direct dissociation of intermediate MO at the anode.[10] While the second reaction route generated oxygen by the process of forming and decomposing for the MOOH intermediate. Though these two different reaction routes suffered diverse approaches to generating oxygen, the surface metal species of

electrocatalyst (M) could be recognized as the active sites during these two reaction processes. Therefore, we could conclude that the M-O band such as M-OOH, M-O, and M-OH is a very important role in evaluating the electrocatalytic activity.[11-14] In fact, the activity of electrocatalysts was dependent on the strength of the M-O bond, because a high-intensity M-O bond could limit the rate of product decomposition, while a weak M-O bond could hinder the binding process between the intermediate and the surface of the electrocatalyst at the anode.[15-17] A "volcano-shaped" relationship could be formed between the electrocatalytic activity and the M-O bond according to the Sabatier principle.[18-19] The electrocatalysts with a suitable M-O bond strength are usually located on the top of the "volcano" with excellent electrocatalytic activity.[20] The electrocatalysts with a weak or high-intensity M-O bond strength are usually located on the foot of the "volcano" with poor electrocatalytic activity.[21-24]

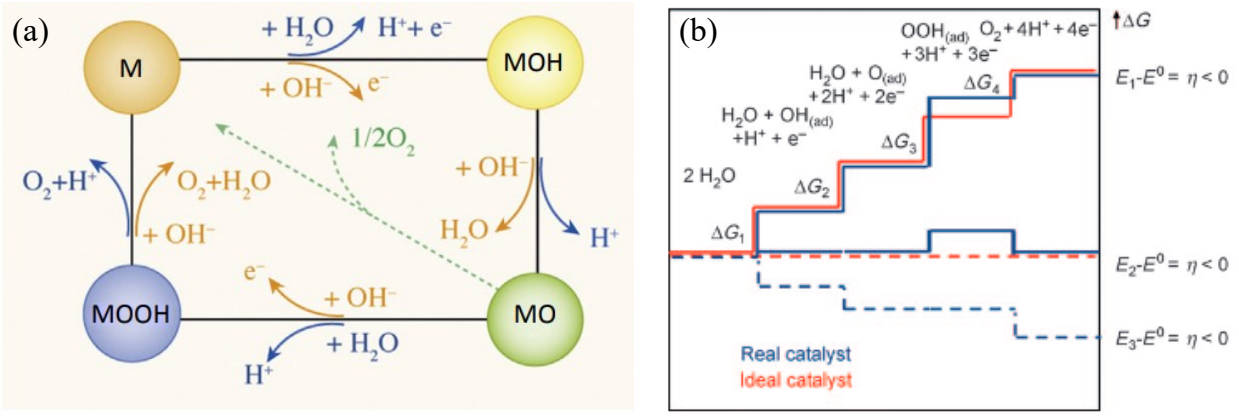

Figure 1.1. (a) The electron transfer steps of OER in alkaline electrolysis (red line). M represents the metal active site on the surface of electrocatalysts. M-OOH and M-OH represent the two different intermediates within pathways to generate oxygen.[18] Copyright 2019, Elsevier. (b) The Gibbs free energies of intermediates for each electron-transfer step in OER. The red line represents the Gibbs free energies of intermediates under ideal electrocatalysts, and the blue line

represents the Gibbs free energies of intermediates under ideal electrocatalysts.[19] Copyright 2021, John Wiley and Sons.

During the four-electron transfer process, the energetics at different applied potentials for the real electrocatalysts and real electrocatalysts were displayed in Figure 1.1b. In addition, the responding decomposition and adsorption of Gibbs energies ΔG_i during four-electron transfer process for every step were also provided:[6-7, 25]

$$\Delta G_1 = \Delta G_{MOH} + k_b T \ln a_{H^+} - \Delta G_M - eU \quad (6)$$

$$\Delta G_2 = \Delta G_{MO} + k_b T \ln a_{H^+} - \Delta G_{MOH} - eU \quad (7)$$

$$\Delta G_3 = \Delta G_{MOOH} + k_b T \ln a_{H^+} - \Delta G_{MO} - eU \quad (8)$$

$$\Delta G_4 = \Delta G_M + k_b T \ln a_{H^+} - eU \quad (9)$$

Where the responding decomposition and adsorption of Gibbs energies during each electron transfer process were represented with "ΔG_i". While "eU" is the change of energy under the applied voltage. The "a_{H^+}" is the proton activity and "k_b" is the Boltzmann constant. And "T" represents the room temperature (298 K). During the theoretic electrocatalyst process, each single electron transfer step should have the same Gibbs free energy and each reaction step should have the same chemisorption energy,[26-28] which is that all the Gibbs free energies during these four-electron transfer processes should be equal ($\Delta G_1 = \Delta G_2 = \Delta G_3 = \Delta G_4$). However, the responding decomposition and adsorption of Gibbs energies were different in a real electrocatalytic OER process, in which the actual relationship of Gibbs free energies between each single electron transfer step followed this sequence: $\Delta G_4 < \Delta G_1 = \Delta G_2 < \Delta G_3$.[29] According to this real Gibbs free energies relationship, the ΔG_3 suffered the highest Gibbs free energy than other Gibbs free energies, which indicated a more difficult process for the responding intermediate forming step.[30-33] This result also confirmed that the M-OOH has a weak bond between -OOH and M (metal active site

on the surface of electrocatalyst). Therefore, as the speed-limit step during the OER process, only decrease the responding decomposition and adsorption of Gibbs free energy of -OOH and M (ΔG_{MOOH}), the value of ΔG_{MOOH} could shift to a more negative value,[34-35] thus the intermediates could form a strong bond with the surface of electrocatalyst and get more favorable spaced reaction Gibbs free energy, and finally the OER activity of electrocatalyst could get a great promotion.

As the result, it is very important to control the binding energy of the M-O bond for the intermediates such as M-OH, M-O, and M-OOH, which could be a useful method to improve the OER activity of electrocatalysts.[36-37] In recent years, many reported works were focused on tuning the binding energy of intermediates during the OER process by structural and electronic engineering methods. However, Strasser and Rossmeisl reported a linear scaling relation between intermediates during the OER process,[38-41] in which the responding decomposition and adsorption energies of some intermediates are strongly intertwined. The intertwined bonding energy for intermediates at OER made it not suitable to just tune single Gibbs free of one reaction process during the OER process alone.[42-44] This also made it difficult to further improve the OER activity by the above-mentioned theoretical method. Therefore, developing unique electrocatalysts with universal application for an electrocatalytic system is still a challenging but a promised useful method to prepare the theory-guided electrocatalysts.

1.2.2 The hydrogen evolution reaction mechanism

As one-half of the electrochemical water-splitting reaction, the hydrogen evolution reaction (HER) occurs at the cathode. Usually, the HER could be enabled in acidic solution and alkaline solution. The Volmer-Tafel and Volmer-Heyrovsky mechanism theory could be recognized as a well explosion for the HER process at the cathode during the process of electrochemical water-

splitting[45-47] reaction. For the HER process in the acidic solution, the reaction processed are followed these equations:

$$H^+ + e^- \rightarrow M\text{-}H^* \quad (10)$$

$$M\text{-}H^* + H^+ + e^- \rightarrow H_2 \quad (11)$$

$$2M\text{-}H^* \rightarrow H_2 + 2M \quad (12)$$

Where the M-H* represents the hydrogen intermates adsorbed on the surface-active site of electrocatalysts (M). Firstly, the HER process began from a Volmer step (10) with the hydrogen intermates adsorption process,[48] in which the hydrogen intermates (H*) were generated on the surface of the electrocatalyst through the processes of proton and electron exchange, and the desorption step. Then the hydrogen could be generated by a desorption step of M-H* and followed a combination step of proton and electro shown in Heyrovsky step (11).[49-52] In addition, the combination of two M-H* on the surface of the electrocatalyst also generates hydrogen with the Tafel step (12). According to the above HER forces in acidic solution, the intermates H* occurred in each HER step, which indicated that the adsorption of H* played an important role during the whole HER process.[53] The Gibbs free energy of the H* (ΔG_{H^*}) could affect the adsorption reaction between H* and electrocatalysts, which could be recognized as a basic criterion to evaluate the speed rate of HER and the performance of HER electrocatalysts.[54-56] Therefore, the electrocatalyst with high activity is critical for promoting the efficiency of HER. With these results, an effective electrocatalyst should meet the requirement of a near-zero Gibbs free energy (ΔG_{H^*}) for thermal neutral hydrogen generated reaction.[57-58] Because a too negative ΔG_{H^*} for the adsorption reaction of H* and electrocatalyst will create a strong combination between H* and electrocatalyst, and thus result in a hard hydrogen release process. While a too positive ΔG_{H^*} for the adsorption reaction of H* and electrocatalyst will consume more energy to attract the H* to the surface of the

electrocatalyst, thus resulting in a high onset potential. Moreover, a superior electrocatalyst should also have a low Tafel slope, because of the high electron transfer rate.[59-61]

The HER process in the alkaline solution also follows the Volmer step, Heyrovsky step and Tafel step. And the reaction processed are followed these equations:

$$H_2O + e^- \rightarrow M\text{-}H^* + OH^- \quad (13)$$

$$H_2O + M\text{-}H^* + e^- \rightarrow H_2 + OH^- \quad (14)$$

$$2H_2O + 2e^- \rightarrow H_2 + 2OH^- \quad (15)$$

During the HER processes in the alkaline solution, the hydrogen intermates H* also played an important role, which the Gibbs free energy for the desorption reaction of H* and electrocatalyst (ΔG_{H^*}) also could evaluate the electrocatalytic activity for the HER.[62-64] However, different with the HER process in the acidic solution, the HER process in the alkaline solution started with the reaction process of decomposing H_2O to provide the H* (Volmer step) in equation (13). The next steps of equation (14) and equation (15) are the same as the HER process in acidic solution, which are the Heyrovsky (14) and Tafel slope (15) steps.[9, 65] Therefore, the high effective electrocatalysts for OER in the alkaline solution could be developed by controlling the ΔG_{H^*} of the water decomposing reaction. The ΔG_{H^*} of the water decomposing reaction should be close to thermoneutral because too positive or negative ΔG_{H^*} will result in waste energy for decomposing water reaction.

The electrocatalytic activity of catalysts for HER could be evaluated by the polarization curves and Tafel slope, which could be obtained by the electrochemical measurement and calculation. In attention, the Tafel slope and overpotential obtained from the polarization curves are the most important parameters to evaluate the HER electrocatalytic ability of catalysts and

could also reveal the HER kinetics and mechanisms. The polarization curves could be recognized as a useful method to understand the relationship between the applied potential of the electrocatalysts and the current density. This relationship between the applied potential of the electrocatalysts and the current density could be explored by the linear sweep voltammetry (LSV) measurement, where the current density and the responding applied potential of the electrocatalyst were recorded. Moreover, the recorded applied potential in LSV result usually was converted to the potential with reference to the hydrogen reversible (RHE). Among the recorded current density and the applied potential in LSV results, the overpotential was one of the most important parameters to evaluate the HER electrocatalytic ability of catalysts. Because of the energy loss and the reaction limitation for the kinetic in an actual electrocatalyst, the equilibrium theory overpotential (0 V) is hard to be achieved in the HER process. Therefore, different HER electrocatalysts could be compared with together with the overpotential at the same current density, which indicated the difference between the theory potential and the actual applied potential of the electrocatalyst.

The reaction kinetics within the HER process could be revealed by the Tafel slope. Tafel slope followed this equation: $\eta = a + b \log j$. Where the η represents the overpotential of the electrocatalyst, a is a constant, b represents the Tafel slope, and the j is the current density. The reaction pathway and the speed-limit step during the HER process could be indicated by the value of the Tafel slope. In addition, for the Tafel step, Heyrovsky and Volmer steps, the responding Tafel slope is calculated to 30, 40 and 120 mV dec^{-1} in a certain low current density and potential scale.[66-67] Therefore, the electrocatalysts owned a low Tafel slope are recognized as a high effective electrocatalyst towards HER and also represent a more favorable HER kinetic with high current density at a relatively low applied potential.

1.3 Interface engineering technology designed transition metal dichalcogenides electrocatalysts

As displayed in Figure 1.2, transition metal dichalcogenides (TMDs) were one kind of graphite like materials, which could be described as a common chemical formula with MX_2 (where M represents the transition metals such as W, Fe, Ni, etc., while X represents the chalcogen like Se or S).[68-72] The bulk TMDs have a unique layered structure, which is stacked by each ultrathin monolayer along a certain direction through a weak van der Waals forces between interlayers. Each ultrathin TMDs monolayer exhibits a specific sandwich crystal structure, which is consisted with one layer of transition metal and two layers of chalcogen. More specifically, this special sandwich structure could be described as X-M-X, where one transition metal layer is located at the centra between two layers of chalcogen.[73-75] Different with the weak van der Waals force between interlayers, the transition metal atoms are combined with each other tightly by the atomic force through the transition metal crystal plane, while the chalcogen atoms are combined with each other tightly by the covalent bond through the chalcogen crystal plane. This unique property of TMDs make it easy to prepare the TMDs nanosheets with ultrathin thickness less than 10 nm. Up to now, two different methods were used to prepare ultrathin TMDs nanosheets. One kind method is top-down method. The top-down method is to exfoliate the bulk TMDs into nanosheets. The main principle of top-down method is to destroy the weak van der Waals forces between interlayer, thus the stacked layers will be separated to form thin layers.[76-80] For example, the liquid exfoliation method is using organic surface-active agents or metal ions with small diameter to insert into the interlayers, and the monolayer will be separated under the sonication process. Electrochemical exfoliation process is using the applied voltage to force the charged ion to insert into the interlayers, and the monolayer will be separated under the gas pressure from the reduction or oxidation process

of charged ion. Another method to prepare TMDs nanosheets is bottom-up approach. The bottom-up method prepares TMDs nanosheets from the precursors. For example, hydrothermal method could be recognized as an efficient way to produce TMDs nanosheets. In addition, chemical vapor deposition (CVD) method is usually to produce TMDs nanosheets with high crystal degree and large diameter.[81-84]

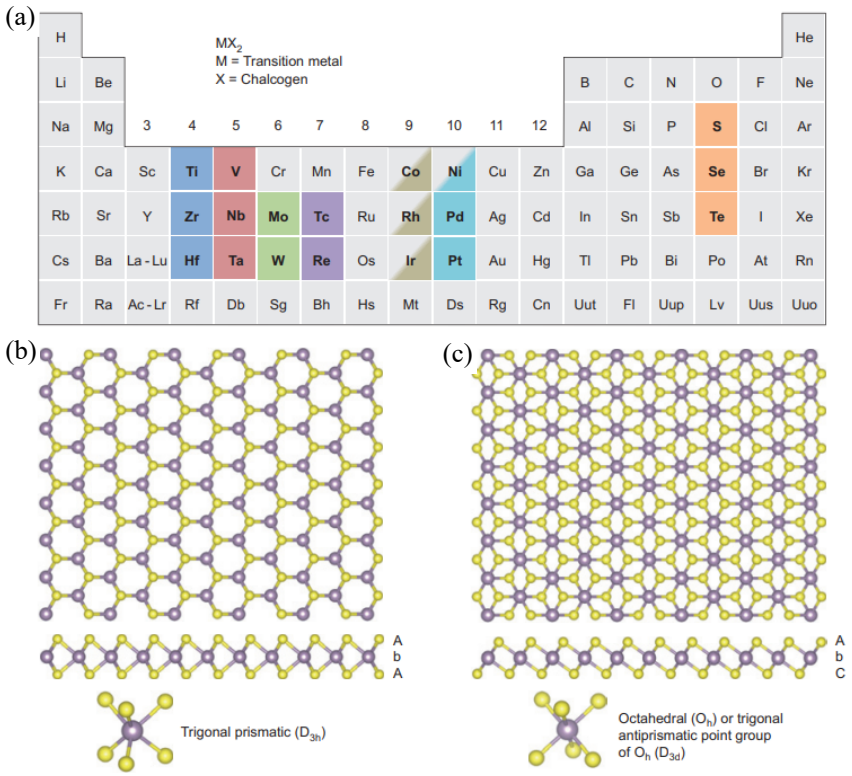

Figure 1.2. (a) Almost of 40 kinds of TMDs species in the periodic table. The tradition metal elements and chalcogen elements were also highlighted. (b, c) The structure of single monolayer of TMDs nanosheets and 1T, 2H phases structures respectively.[85] Copyright 2018, American Chemical Society.

The multicrystal structure of TMDs nanosheets is also an important property. Transition metal chalcogens have different arrangements and stacked sequence between metal layers and chalcogen

layers. For example, the S and Mo atoms have three different arrangements, which results in three different crystal phases (3R rhombohedral, 2H hexagonal, and 1T trigonal). These differences of crystal structures also result in different electronic property and electrocatalytic activity. By exfoliating bulk WS_2 into ultrathin nanosheets, the WS_2 phase transferred from 2H to 1T phase. During this phase transformation process, the previous electronic and crystal structure were destroyed and the ratio zigzag-like strain in interlayers increased. Many previous experiments and theory calculations have confirmed that the unoccupied density of states (DOS) of ultrathin WS_2 nanosheets near the Fermi level. This important discovery suggesting that the ultrathin TMDs nanosheets could be more favorable in electrocatalytic HER reaction because the DOS with the value near the Fermi level takes positive effect in ΔG_{H^*} during HER process. In addition, previous reported theory calculations and experiments demonstrated that the X sites of TMDs is crucial towards the electrocatalytic activity. Density functional theory (DFT) calculations and experiments indicated the X sites located at the edge of TMDs interlayers could be recognized as the active site towards electrocatalytic activity rather than the X sites located on the basal plane. Moreover, experiments and DFT calculation results also confirmed that the metal element doping,[86-88] and no-metal element doping could also enhance the TMDs HER activity. For example, Ni, Fe, Co and B, O, N doping could efficiently promote the TMDs HER activity.

According to the experiment and calculation results, many useful methods were used to develop more exposed active site and high effective TMDs electrocatalysts. Among methods of detect engineering, lateral size design and element doping, the interface engineering technology received great attention due to advantages of easy operation, energy-saving, and high efficiency.[88-92] Through the interface engineering technology, the heterostructure could be constructed in the electrocatalyst, which exhibited outstanding electrocatalytic activity and unique chemical and

physical properties. The heterojunction in the electrocatalysts could result in strong electronic interaction and synergy effect between different elements at the interface of electrocatalyst, which could significantly enhance the HER electrocatalytic activity.

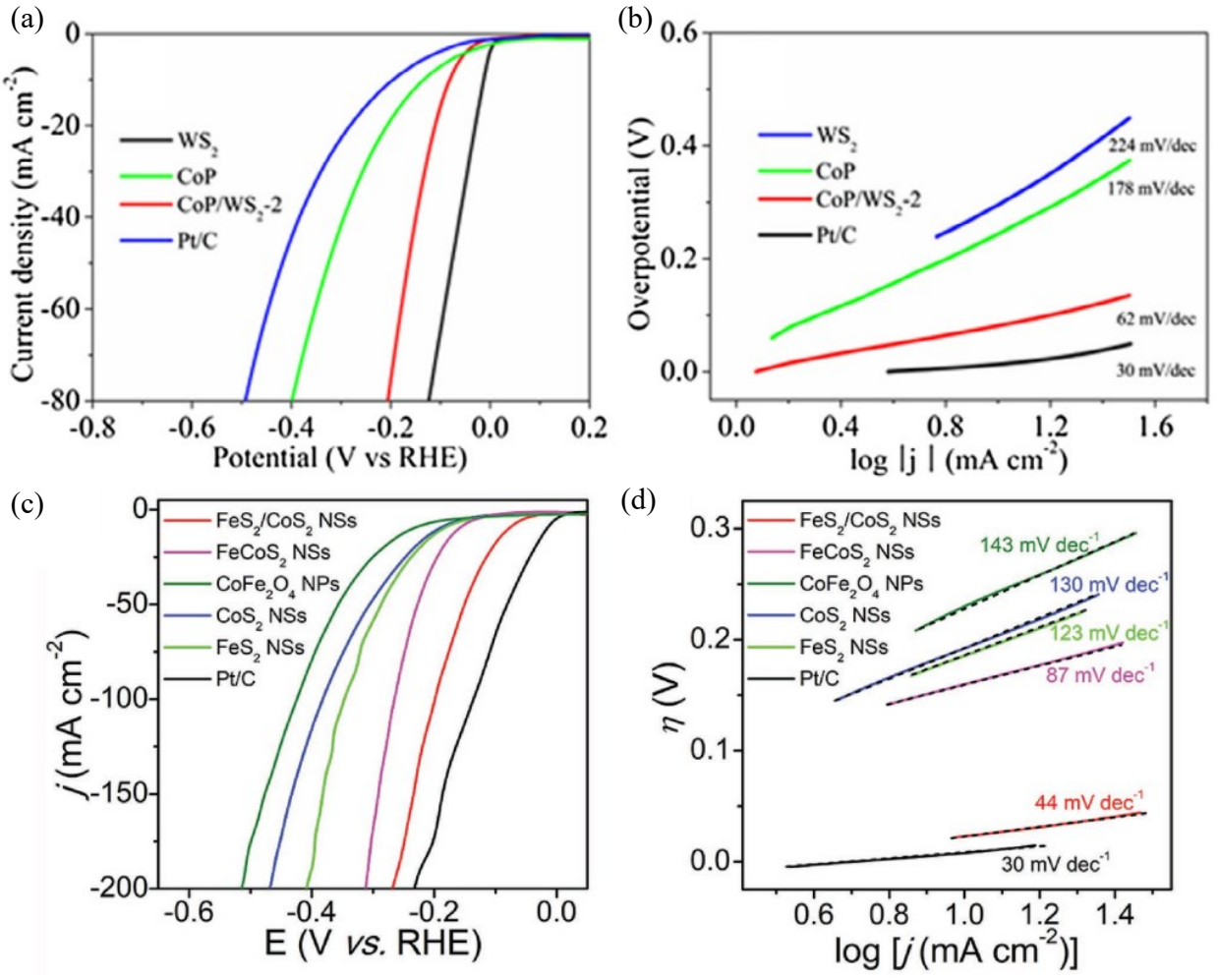

Figure 1.3. (a) The HER LSV measurements of heterojunction CoP/WS_2 and the responding single materials. Copyright 2018, Elsevier. (b) The Tafel slope of heterojunction FeS_2/CoS_2 and the responding single materials and (c) the HER LSV measurements of heterojunction FeS_2/CoS_2 and the responding single materials.[93] Copyright 2018, John Wiley and Sons.

Specifically, the different element heterojunctions in electrocatalysts could result in different synergy effects for electrocatalytic reaction. However, the synergy effect resulted from different elements always exhibit more superior electrocatalytic activity to that of their single element. In fact, during the electrocatalytic reaction process, the specific reaction step was completed by the relative element. The each of element with high effective electrocatalytic activity could remarkably accelerate the reaction speed, therefore resulted in huge promoted electrocatalytic activity. For example, as shown in Figure 1.3a, the heterojunction CoP/WS_2 electrocatalyst exhibited excellent HER activity, which was much superior to that of single WS_2 and CoP electrocatalysts. Tafel slope results also demonstrated that the heterojunction CoP/WS_2 electrocatalyst enabled more favorable HER kinetic reaction. Moreover, by constructing FeS_2/CoS_2 heterojunction, the developed FeS_2/CoS_2 electrocatalyst exhibited much superior HER activity,[94-98] which had a lower overpotential than that of single FeS_2 and CoS_2 electrocatalysts. The Tafel slope results also confirmed that the heterojunction exhibited excellent HER performance compared the responding single materials. Therefore, the synergy effect in the heterojunction provided more active sites during electrocatalytic process. And the interface engineering technology also provided more useful opportunity for TMDs to further improve the electrocatalytic activity.

1.4 High entropy alloys for electrocatalysts

Among various metal-based electrocatalysts, noble metal-based electrocatalysts, such as Pt, Pd, Rh, Ru and Ir etc., exhibited the highest electrocatalytic activity toward HER and OER respectively.[99-101] However, the high price and rare reserve on the earth limit their large-scale application. In the past years of experiments, tradition metals and their alloys were demonstrated to have a good electrocatalytic activity and chemical stability. In addition, the low-cost and various kinds of compounds also make them an ideal electrocatalyst to replace the noble metal based

electrocatalysts. Many previous experiments and calculations indicated the transition metal could be recognized as the active sites, which is favorable for adsorbing and desorbing intermediates during electrocatalytic reaction process. Therefore, an excellent electrocatalyst should meet the points of possessing suitable active sites and favorable adsorbing and desorbing energy for the intermediates during reaction.[102-104] According to this above result, we should control and optimize the relationship of interface and surface atoms and also to create the coordination synergy effect in the catalyst. However, it is very difficult to integrate all kinds of different metal elements into one electrocatalyst due to the different electronic structure of metal elements. Up to now, the excellent electrocatalysts with high electrocatalytic activity usually comprise less than three metal elements. Therefore, developing an effective and unconventional alloy system with in various metal active sites inside for electrocatalysts is promised and urgent.

Recently, high entropy alloys (HEAs) are widely used for electrocatalysts due to the multicomponent property.[105] In addition, HEAs are also more favorable for designing multifunctional electrocatalysts, because the HEAs could provide numerous metal elements composition. As we all know, there are two different ways to define the HEAs, which are composition and entropy ways respectively.[106] Generally, the entropy way is that the HEAs should have at least five different metal elements and the atomic ratio of each single metal element must be between 5% and 35%. Another entropy definition way is to evaluate the whole entropy of the HEAs. The mixed entropy of the HEAs could be evaluated by the entropy for the mixed configuration (ΔS_{mix}). The HEAs mixed configuration entropy could be calculated by the following equation:

$$\Delta S_{mix} = -R \sum_{i=1}^{n} x_i \ln x_i \quad (16)$$

Where the R represents the gas constant, and the x_i is the molar amount of each metal element in the HEAs. Moreover, the ΔS_{mix} of HEAs could also be calculated by the followed equation when all each single metal element has the same atomic molar concentration:[105, 107-108]

$$\Delta S_{mix} = R \ln n \quad (17)$$

Where the n is the full number of each metal element species of HEAs. For example, if the $n \geq 5$, the mixed configuration entropy of the HEAs was calculated to $\Delta S_{mix} \geq 1.609R$, which indicated a high entropy alloy. However, when the number of each metal element species decreased to four, the mixed configuration entropy of the quaternary alloy was calculated to $\Delta S_{mix} \geq 1.386R$. Though the ΔS_{mix} of the quaternary alloy is smaller than the ΔS_{mix} of quinary alloy, the quaternary alloy could also be recognized to the HEAs but a medium entropy rather than the high entropy. Most of HEAs could be well defined by the above mentioned two definitions.

The unique characteristics and properties of HEAs were fully understood by previous reported experiments and research. There are three main effects for extensive exploration: 1. the high entropy effect; 2. the sluggish diffusion effect; 3. the lattice distortion effect.[109-110]

1. High entropy effect. The high entropy effect is an internal property of the HEAs, of which the effect could increase with the sequence of increasing number of the metal element species. Specifically, according to equations of 16 and 17, the total mixed configuration entropy of HEAs will increase when the number of the near atomic ratio for metal element compounds increase. Under the high temperature, all the near equimolar metal element species will be formed to a single phase, which results from the process of lowing the responding free energy. This high entropy effect is benefitting to stable the structure of HEAs. Moreover, this high

entropy effect is also favorable for adjusting the electronic relationship between all kinds of metal atoms, which is beneficial to regulate and optimize the property of electrocatalysts.

2. Sluggish diffusion effect. Different of the common binary and ternary alloys, the HEAs possess various metal atoms, which results in different free energies of various metal species. This property leads to a varying diffusion rates of various metal elements in HEAs, which could result in a slow process of phase change and slow kinetics of atoms diffusion. However, we can use the sluggish diffusion effect to control the nanocrystalline structure of HEAs during the prepare process, because the diffusion of atoms located on the surface of HEAs could be intervened easily during the synthetic steps. Therefore, this property of HEAs is beneficial to control the nanocrystalline structure of HEAs, and thus influence the electrocatalytic activity for HEAs.

3. Lattice distortion effect. The lattice distortion effect in HEAs is on account of the prominent difference of the sizes for different various metal elements. This lattice distortion effect is beneficial to improve the mechanical property of HEAs, because this severest lattice distortion could arise an intensive lattice strain, which could avoid crystalline dislocation slipping in HEAs. Moreover, the phonon scattering could be increased by the defects between inter metal atoms, which resulted from the distortion effect. The thermal binding energies and electronic conductivity in HEAs could be decreased due to this lattice distortion effect. Therefore, the energy barrier and adsorption or desorption for intermediates during reaction process could be decreased in HEAs electrocatalysts.

With these above unique properties, the HEAs as electrocatalysts could decrease the cost as well as remaining high effective electrocatalytic activity. As shown in Figure 1.4a and b, the fcc

single phase HEAs prepared at 800 ºC exhibited low HER Tafel slope, which was lower than that of commercial Pt electrocatalyst and the dual phase alloy prepared at 1100 ºC. A low HER overpotential of 64 mV at current density of 10 mA cm^{-2} could be achieved by the FeCoPdIrPt HEAs in 1.0 M KOH, which was even smaller than that of Pt/C electrocatalyst (Figure 1.4c). The compound of FeCoPdIrPt HEAs and GO (FeCoPdIrPt@GO) exhibited outstanding electrocatalytic stability for HER for over 150 h at 10 mA cm^{-2} (Figure 1.4d). In addition, Liu and

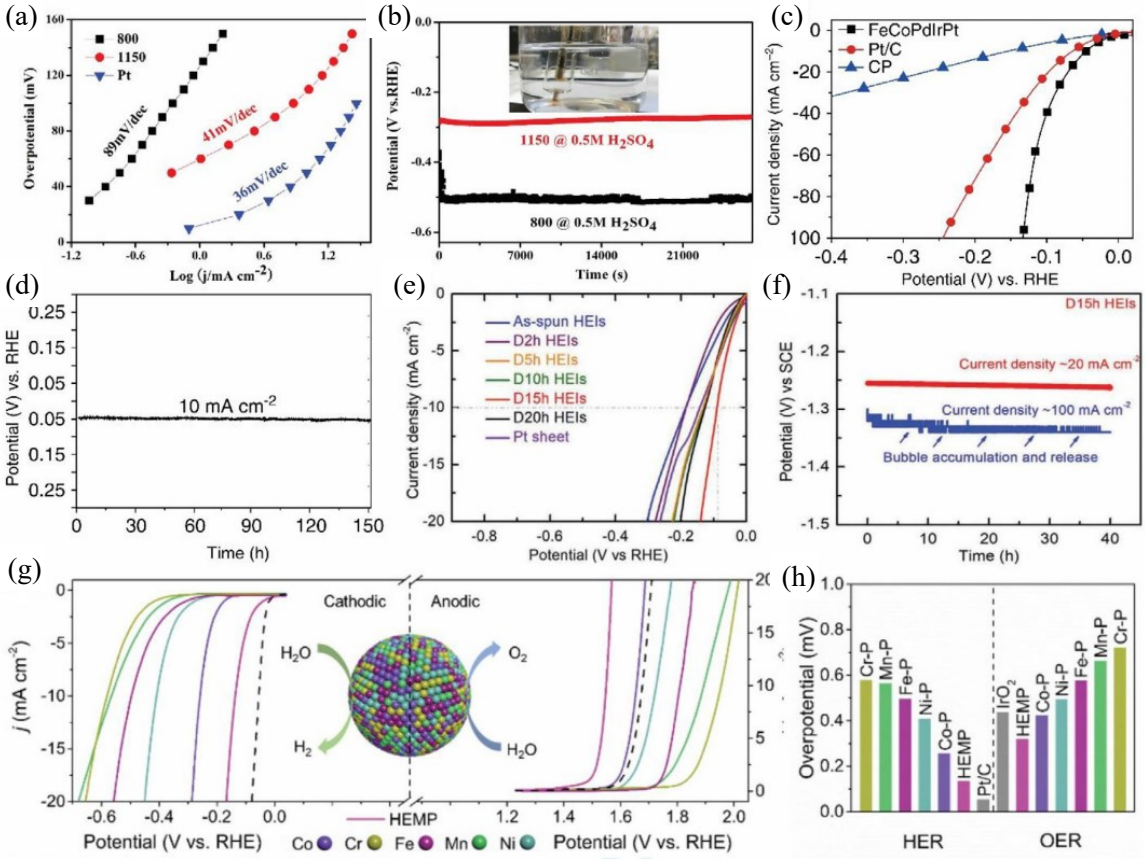

Figure 1.4. (a) Tafel slopes and (b) electrocatalytic HER stability measurements of NiFeMoCoCr HEAs.[111] (c) The HER LSV curves of FeCoPdIrPt@GO and compared Pt/C electrocatalyst and (d) the electrocatalytic HER stability measurement of FeCoPdIrPt@GO at 10 mA cm^{-2}.[112] (e) LSV curves for HER in 0.5 M H_2SO_4 solution and (f) the electrocatalytic HER stability measurements of D15 HEAs at 20 and 100 mA cm^{-2} respectively.[113] (g) HER and OER

LSV curves of CoCrFeMnNiP HEAs in 1.0 M KOH and (h) the overpotentials at current density of 10 mA cm^{-2}.[114]

coworkers reported a high entropy intermetallic with the FeCoNiAlTi by the melt spinning method. The FeCoNiAlTi HEAs exhibited a low HER overpotential of 88.2 mV at 10 mA cm^{-2} and a low Tafel slope of 40.1 mV dec^{-1} with a good stability (Figure 1.4e and f). By introducing P into the CoCrFeMnNi HEAs, the prepared CoCrFeMnNiP HEAs exhibited excellent HER activity kinetic and fast charge transfer rate, due to the synergy effect and more active sites in CoCrFeMnNiP HEAs (Figure 1.4g and h).[108, 115-117]

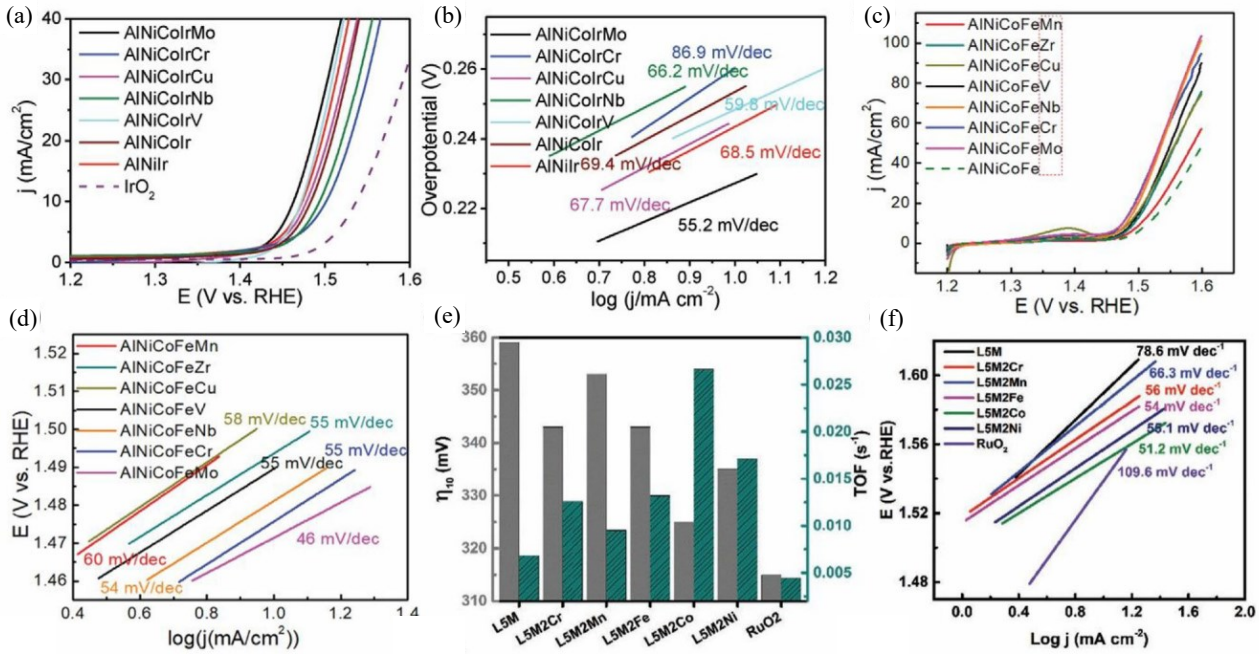

Figure 1.5. (a) The OER LSV curves and (b) Tafel slopes of AlCoNiTr HEAs in 0.5 M H_2SO_4.[118] (c) The OER LSV curves and (d) Tafel slopes of AlNiCoFe HEAs.[119] (e) The OER overpotential and TOF result of the HEPO and (f) the responding Tafel slopes.[120]

Besides the outstanding HER performance, the HEAs electrocatalysts are also promised high effective OER catalysts. Figure 1.5a and b exhibited an excellent OER activity with a low

overpotential at current density of 10 mA cm^{-2} for 233 mV and a Tafel slope with 55.2 mV dec^{-1}. Moreover, a various metal elements HEAs without noble metal of AlCoNiFeX HEAs (Figure 1.5c and d), where X is Nb, Cu, Cr, V, Zr, Mn, or Mo, were reported an excellent OER activity, in which the AlCoNiFeX HEAs were covered by hydroxide surface. The AlCoNiFeX HEAs displayed an overpotential of 240 mV toward OER at 10 mA cm^{-2}. At the same time, Ting and coworkers reported a kind of high entropy perovskite oxide (HEPO), which was consisted with at least five first row of transition metals (Fe, Co, Ni, Cr, and Mn). Specifically, the prepared HEPO exhibited excellent OER activity with overpotential of 245 mV and a low Tafel slope with 54 mV dec^{-1}.

1.5 Research motivation and main content of this thesis

Developing transition metal sulfides electrocatalysts with high efficiency for hydrogen evolution reaction (HER) is highly expected to promote the development of hydrogen energy. Herein, a novel iron tungsten sulfide heterojunction nanosheets (Fe_xS_y/WS_2 Ns) with petal-like structure were prepared by a facile hydrothermal method. The prepared petal-like Fe_xS_y/WS_2 Ns owned a large diameter size of ~1 μm and thickness of 8 nm for each flak. The developed Fe_xS_y/WS_2 Ns exhibited excellent HER activity with overpotential of 118 mV at 10 mA cm^{-2} and a low Tafel slop of 87 mV dec^{-1} in 0.5 M H_2SO_4, which was much better than that of single Fe_xS_y and WS_2 (> 420 mV at 10 mA cm^{-2}). This advanced HER activity owned to the unique thin structure and more exposed active sites provided by defects between crystal interface of Fe_xS_y and WS_2. Furthermore, the Fe_xS_y/WS_2 Ns as bifunctional electrocatalyst could achieve energy-saving water-splitting by replacing oxygen evolution reaction of urea oxidation reaction to decrease the applied voltage of 147 mV.

To further improve the electrocatalytic activity, a non-noble metal NiFeCoMnCu high entropy alloy (HEAs) were synthesized by a facile citric acid chelating method. Moreover, the unary Ni, binary NiFe, ternary NiFeCo, and quaternary NiFeCoMn electrocatalysts were also prepared and characterized for comparison. Specially, prepared NiFeCoMnCu HEAs possessed an fcc single-phase structure and dispersed uniformly on the carbon structure with a diameter size of ~ 80 nm. Benefiting from the high-entropy effect, the NiFeCoMnCu HEAs exhibited outstanding oxygen evolution reaction (OER) and hydrogen evolution reaction (HER) activity with an overpotential of 240 mV and 165 mV at 10 mA cm^{-2} in 1.0 M KOH respectively. The enhancement of electrocatalytic activity with the sequence of increasing metal species number demonstrated that the synergy effect between metal elements in HEAs resulted in the excellent activity.

With this excellent activity for OER and HER, the NiFeCoMnCu HEAs as the bifunctional electrocatalyst were applied for the water-splitting reaction through a two-electrode system in 1.0 M KOH solution. The current density of electrochemical water-splitting only required 1.53 V to reach 10 mA cm^{-2}, which was much lower than that of Pt/C-RuO_2 electrocatalysts (1.65 V). Almost 10 h continuous electrochemical water-splitting process also confirmed the excellent stability of the bifunctional NiFeCoMnCu HEAs electrocatalyst. In addition, an electrochemical seawater-splitting reaction could be also enabled by the bifunctional NiFeCoMnCu HEAs electrocatalyst with current density of 10.5 mA cm^{-2} at 1.8 V for continuous 10 h reaction process.

In this thesis, we developed different seven non-noble metal electrocatalysts, which specifically were the bimetal heterojunction Fe_xS_y/WS_2 nanosheets, the unary Ni, binary NiFe, ternary NiFeCo, quaternary NiFeCoMn, and quinary NiFeCoMnCu HEAs multimetalic electrocatalytic activities of HER in acidic and alkalic solution and OER activity for these multimetalic electrocatalysts were explored. In addition, the prepared multimetalic electrocatalysts

were used for bifunctional catalysts to execute electrochemical water-splitting reaction. The experiments demonstrated that the prepared multimetalic electrocatalysts possessed excellent electrochemical water-splitting activity. In addition, the NiFeCoMnCu HEAs also exhibited stable seawater-splitting activity for 10 h continuous reaction.

References

1. Xiong, B.; Chen, L.; Shi, J., Anion-Containing Noble-Metal-Free Bifunctional Electrocatalysts for Overall Water Splitting. *ACS Catalysis* **2018,** *8* (4), 3688-3707.

2. Yu, J.; He, Q.; Yang, G.; Zhou, W.; Shao, Z.; Ni, M., Recent Advances and Prospective in Ruthenium-Based Materials for Electrochemical Water Splitting. *ACS Catalysis* **2019,** *9* (11), 9973-10011.

3. Lu, H.; Tournet, J.; Dastafkan, K.; Liu, Y.; Ng, Y. H.; Karuturi, S. K.; Zhao, C.; Yin, Z., Noble-Metal-Free Multicomponent Nanointegration for Sustainable Energy Conversion. *Chem Rev* **2021,** *121* (17), 10271-10366.

4. Feng, C.; Faheem, M. B.; Fu, J.; Xiao, Y.; Li, C.; Li, Y., Fe-Based Electrocatalysts for Oxygen Evolution Reaction: Progress and Perspectives. *ACS Catalysis* **2020,** *10* (7), 4019-4047.

5. Zhang, Y.-C.; Han, C.; Gao, J.; Pan, L.; Wu, J.; Zhu, X.-D.; Zou, J.-J., NiCo-Based Electrocatalysts for the Alkaline Oxygen Evolution Reaction: A Review. *ACS Catalysis* **2021,** *11* (20), 12485-12509.

6. Ding, H.; Liu, H.; Chu, W.; Wu, C.; Xie, Y., Structural Transformation of Heterogeneous Materials for Electrocatalytic Oxygen Evolution Reaction. *Chem Rev* **2021,** *121* (21), 13174-13212.

7. You, B.; Sun, Y., Innovative Strategies for Electrocatalytic Water Splitting. *Acc Chem Res* **2018,** *51* (7), 1571-1580.

8. Wang, P.; Wang, B., Designing Self-Supported Electrocatalysts for Electrochemical Water Splitting: Surface/Interface Engineering toward Enhanced Electrocatalytic Performance. *ACS Appl Mater Interfaces* **2021,** *13* (50), 59593-59617.

9. Si, J.; Zheng, Q.; Chen, H.; Lei, C.; Suo, Y.; Yang, B.; Zhang, Z.; Li, Z.; Lei, L.; Hou, Y.; Ostrikov, K. K., Scalable Production of Few-Layer Niobium Disulfide Nanosheets via

Electrochemical Exfoliation for Energy-Efficient Hydrogen Evolution Reaction. *ACS Appl Mater Interfaces* **2019,** *11* (14), 13205-13213.

10. Sarma, P. V.; Vineesh, T. V.; Kumar, R.; Sreepal, V.; Prasannachandran, R.; Singh, A. K.; Shaijumon, M. M., Nanostructured Tungsten Oxysulfide as an Efficient Electrocatalyst for Hydrogen Evolution Reaction. *ACS Catal.* **2020,** *10* (12), 6753-6762.

11. Dresp, S.; Dionigi, F.; Klingenhof, M.; Strasser, P., Direct Electrolytic Splitting of Seawater: Opportunities and Challenges. *ACS Energy Letters* **2019,** *4* (4), 933-942.

12. Kou, T.; Wang, S.; Li, Y., Perspective on High-Rate Alkaline Water Splitting. *ACS Materials Letters* **2021,** *3* (2), 224-234.

13. Yuan, C.-Z.; Hui, K. S.; Yin, H.; Zhu, S.; Zhang, J.; Wu, X.-L.; Hong, X.; Zhou, W.; Fan, X.; Bin, F.; Chen, F.; Hui, K. N., Regulating Intrinsic Electronic Structures of Transition-Metal-Based Catalysts and the Potential Applications for Electrocatalytic Water Splitting. *ACS Materials Letters* **2021,** *3* (6), 752-780.

14. Zheng, M.; Du, J.; Hou, B.; Xu, C. L., Few-Layered $Mo_{(1-x)}W_xS_2$ Hollow Nanospheres on Ni3S2 Nanorod Heterostructure as Robust Electrocatalysts for Overall Water Splitting. *ACS Appl Mater Interfaces* **2017,** *9* (31), 26066-26076.

15. Bai, J.; Meng, T.; Guo, D.; Wang, S.; Mao, B.; Cao, M., Co_9S_8@MoS_2 Core-Shell Heterostructures as Trifunctional Electrocatalysts for Overall Water Splitting and Zn-Air Batteries. *ACS Appl. Mater. Interfaces* **2018,** *10* (2), 1678-1689.

16. Han, A.; Zhang, H.; Yuan, R.; Ji, H.; Du, P., Crystalline Copper Phosphide Nanosheets as an Efficient Janus Catalyst for Overall Water Splitting. *ACS Appl. Mater. Interfaces* **2017,** *9* (3), 2240-2248.

17. Jian, J.; Yuan, L.; Qi, H.; Sun, X.; Zhang, L.; Li, H.; Yuan, H.; Feng, S., Sn-Ni3S2 Ultrathin Nanosheets as Efficient Bifunctional Water-Splitting Catalysts with a Large Current Density and Low Overpotential. *ACS Appl. Mater. Interfaces* **2018,** *10* (47), 40568-40576.

18. Kumar, A.; Bhattacharyya, S., Porous NiFe-Oxide Nanocubes as Bifunctional Electrocatalysts for Efficient Water-Splitting. *ACS Appl. Mater. Interfaces* **2017,** *9* (48), 41906-41915.

19. Li, J.; Li, J.; Zhou, X.; Xia, Z.; Gao, W.; Ma, Y.; Qu, Y., Highly Efficient and Robust Nickel Phosphides as Bifunctional Electrocatalysts for Overall Water-Splitting. *ACS Appl. Mater. Interfaces* **2016,** *8* (17), 10826-10834.

20. Liu, P. F.; Yang, S.; Zhang, B.; Yang, H. G., Defect-Rich Ultrathin Cobalt-Iron Layered Double Hydroxide for Electrochemical Overall Water Splitting. *ACS Appl. Mater. Interfaces* **2016,** *8* (50), 34474-34481.

21. Luo, P.; Zhang, H.; Liu, L.; Zhang, Y.; Deng, J.; Xu, C.; Hu, N.; Wang, Y., Targeted Synthesis of Unique Nickel Sulfide (Ni_S, NiS_2) Microarchitectures and the Applications for the Enhanced Water Splitting System. *ACS Appl. Mater. Interfaces* **2017,** *9* (3), 2500-2508.

22. Sun, W.; Zhou, Z.; Zaman, W. Q.; Cao, L.-m.; Yang, J., Rational Manipulation of IrO_2 Lattice Strain on α-MnO_2 Nanorods as a Highly Efficient Water-Splitting Catalyst. *ACS Appl. Mater. Interfaces* **2017,** *9* (48), 41855-41862.

23. Tao, Z.; Wang, T.; Wang, X.; Zheng, J.; Li, X., MOF-Derived Noble Metal Free Catalysts for Electrochemical Water Splitting. *ACS Appl. Mater. Interfaces* **2016,** *8* (51), 35390-35397.

24. Wang, P.; Pu, Z.; Li, Y.; Wu, L.; Tu, Z.; Jiang, M.; Kou, Z.; Amiinu, I. S.; Mu, S., Iron-Doped Nickel Phosphide Nanosheet Arrays: An Efficient Bifunctional Electrocatalyst for Water Splitting. *ACS Appl. Mater. Interfaces* **2017,** *9* (31), 26001-26007.

25. Wang, Z.; Zeng, S.; Liu, W.; Wang, X.; Li, Q.; Zhao, Z.; Geng, F., Coupling Molecularly Ultrathin Sheets of NiFe-Layered Double Hydroxide on $NiCo_2O_4$ Nanowire Arrays for Highly Efficient Overall Water-Splitting Activity. *ACS Appl. Mater. Interfaces* **2017,** *9* (2), 1488-1495.

26. Xuan, C.; Wang, J.; Xia, W.; Peng, Z.; Wu, Z.; Lei, W.; Xia, K.; Xin, H. L.; Wang, D., Porous Structured Ni-Fe-P Nanocubes Derived from a Prussian Blue Analogue as an Electrocatalyst for Efficient Overall Water Splitting. *ACS Appl. Mater. Interfaces* **2017,** *9* (31), 26134-26142.

27. Yu, J.; Li, Q.; Chen, N.; Xu, C.-Y.; Zhen, L.; Wu, J.; Dravid, V. P., Carbon-Coated Nickel Phosphide Nanosheets as Efficient Dual-Electrocatalyst for Overall Water Splitting. *ACS Appl. Mater. Interfaces* **2016,** *8* (41), 27850-27858.

28. Du, C.; Yang, L.; Yang, F.; Cheng, G.; Luo, W., Nest-like NiCoP for Highly Efficient Overall Water Splitting. *ACS Catal.* **2017,** *7* (6), 4131-4137.

29. Spanos, I.; Auer, A. A.; Neugebauer, S.; Deng, X.; Tueysuez, H.; Schloegl, R., Standardized Benchmarking of Water Splitting Catalysts in a Combined Electrochemical Flow Cell/Inductively Coupled Plasma-Optical Emission Spectrometry (ICP-OES) Setup. *ACS Catal.* **2017,** *7* (6), 3768-3778.

30. Xiong, B.; Chen, L.; Shi, J., Anion-Containing Noble-Metal-Free Bifunctional Electrocatalysts for Overall Water Splitting. *ACS Catal.* **2018,** *8* (4), 3688-3707.

31. Yang, Y.; Lin, Z.; Gao, S.; Su, J.; Lun, Z.; Xia, G.; Chen, J.; Zhang, R.; Chen, Q., Tuning Electronic Structures of Nonprecious Ternary Alloys Encapsulated in Graphene Layers for Optimizing Overall Water Splitting Activity. *ACS Catal.* **2017,** *7* (1), 469-479.

32. You, B.; Jiang, N.; Sheng, M.; Bhushan, M. W.; Sun, Y., Hierarchically Porous Urchin-Like Ni2P Superstructures Supported on Nickel Foam as Efficient Bifunctional Electrocatalysts for Overall Water Splitting. *ACS Catal.* **2016,** *6* (2), 714-721.

33. Yu, J.; He, Q.; Yang, G.; Zhou, W.; Shao, Z.; Ni, M., Recent Advances and Prospective in Ruthenium-Based Materials for Electrochemical Water Splitting. *ACS Catal.* **2019,** *9* (11), 9973-10011.

34. Zhang, X.; Xu, H.; Li, X.; Li, Y.; Yang, T.; Liang, Y., Facile Synthesis of Nickel-Iron/Nanocarbon Hybrids as Advanced Electrocatalysts for Efficient Water Splitting. *ACS Catal.* **2016,** *6* (2), 580-588.

35. Duan, J.; Chen, S.; Vasileff, A.; Qiao, S. Z., Anion and Cation Modulation in Metal Compounds for Bifunctional Overall Water Splitting. *ACS Nano* **2016,** *10* (9), 8738-8745.

36. Gu, Y.; Chen, S.; Ren, J.; Jia, Y. A.; Chen, C.; Komarneni, S.; Yang, D.; Yao, X., Electronic Structure Tuning in Ni3FeN/r-GO Aerogel toward Bifunctional Electrocatalyst for Overall Water Splitting. *ACS Nano* **2018,** *12* (1), 245-253.

37. Ji, Y.; Yang, L.; Ren, X.; Cui, G.; Xiong, X.; Sun, X., Full Water Splitting Electrocatalyzed by NiWO4 Nanowire Array. *ACS Sustainable Chem. Eng.* **2018,** *6* (8), 9555-9559.

38. Yan, X.; Tian, L.; Atkins, S.; Liu, Y.; Murowchick, J.; Chen, X., Converting $CoMoO_4$ into CoO/MoO_x for Overall Water Splitting by Hydrogenation. *ACS Sustainable Chem. Eng.* **2016,** *4* (7), 3743-3749.

39. Masa, J.; Weide, P.; Peeters, D.; Sinev, I.; Xia, W.; Sun, Z.; Somsen, C.; Muhler, M.; Schuhmann, W., Amorphous Cobalt Boride (Co_2B) as a Highly Efficient Nonprecious Catalyst for Electrochemical Water Splitting: Oxygen and Hydrogen Evolution. *Adv. Energy Mater.* **2016,** *6* (6).

40. Ai, G.; Li, H.; Liu, S.; Mo, R.; Zhong, J., Solar Water Splitting by TiO_2/CdS/Co-Pi Nanowire Array Photoanode Enhanced with Co-Pi as Hole Transfer Relay and CdS as Light Absorber. *Adv. Funct. Mater.* **2015,** *25* (35), 5706-5713.

41. Kuang, M.; Han, P.; Wang, Q.; Li, J.; Zheng, G., CuCo Hybrid Oxides as Bifunctional Electrocatalyst for Efficient Water Splitting. *Adv. Funct. Mater.* **2016,** *26* (46), 8555-8561.

42. Li, J.; Yan, M.; Zhou, X.; Huang, Z.-Q.; Xia, Z.; Chang, C.-R.; Ma, Y.; Qu, Y., Mechanistic insights on ternary $Ni_{2-x}Co_xP$ for hydrogen evolution and their hybrids with graphene as highly efficient and robust catalysts for overall water splitting. *Adv. Funct. Mater.* **2016,** *26* (37), 6785-6796.

43. Wang, X.; Li, W.; Xiong, D.; Petrovykh, D. Y.; Liu, L., Bifunctional Nickel Phosphide Nanocatalysts Supported on Carbon Fiber Paper for Highly Efficient and Stable Overall Water Splitting. *Adv. Funct. Mater.* **2016,** *26* (23), 4067-4077.

44. Wu, Y.; Li, G.-D.; Liu, Y.; Yang, L.; Lian, X.; Asefa, T.; Zou, X., Overall Water Splitting Catalyzed Efficiently by an Ultrathin Nanosheet-Built, Hollow Ni_3S_2-Based Electrocatalyst. *Adv. Funct. Mater.* **2016,** *26* (27), 4839-4847.

45. Gao, X.; Zhang, H.; Li, Q.; Yu, X.; Hong, Z.; Zhang, X.; Liang, C.; Lin, Z., Hierarchical $NiCo_2O_4$ Hollow Microcuboids as Bifunctional Electrocatalysts for Overall Water-Splitting. *Angew. Chem., Int. Ed.* **2016,** *55* (21), 6290-6294.

46. Shi, H.; Liang, H.; Ming, F.; Wang, Z., Efficient Overall Water-Splitting Electrocatalysis Using Lepidocrocite VOOH Hollow Nanospheres. *Angew. Chem., Int. Ed.* **2017,** *56* (2), 573-577.

47. Zhang, J.; Wang, T.; Pohl, D.; Rellinghaus, B.; Dong, R.; Liu, S.; Zhuang, X.; Feng, X., Interface Engineering of MoS_2/Ni_3S_2 Heterostructures for Highly Enhanced Electrochemical Overall-Water-Splitting Activity. *Angew. Chem., Int. Ed.* **2016,** *55* (23), 6702-6707.

48. Zhu, M.; Sun, Z.; Fujitsuka, M.; Majima, T., Z-Scheme Photocatalytic Water Splitting on a 2D Heterostructure of Black Phosphorus/Bismuth Vanadate Using Visible Light. *Angew. Chem., Int. Ed.* **2018,** *57* (8), 2160-2164.

49. Liu, Y.; Wygant, B. R.; Kawashima, K.; Mabayoje, O.; Hong, T. E.; Lee, S.-G.; Lin, J.; Kim, J.-H.; Yubuta, K.; Li, W.; Li, J.; Mullins, C. B., Facet Effect on the Photoelectrochemical performance of a $WO_3/BiVO_4$ Heterojunction Photoanode. *Applied Catalysis B: Environmental* **2019,** *245*, 227-239.

50. Sun, L.; Geng, J.; Gao, M.; Zheng, D.; Jing, Z.; Zhao, Q.; Lin, J., Novel WS_2 /$Fe_{0.95}S_{1.05}$ Hierarchical Nanosphere as a Highly Efficient Electrocatalyst for Hydrogen Evolution Reaction. *Chemistry* **2021**.

51. Yang, X. F.; Li, J.; Yang, X. M.; Li, C. X.; Li, F.; Li, B.; He, J. B., High-performance Bifunctional Ni-Fe-S Catalyst in situ Synthesized within Graphite Intergranular Nanopores for overall Water Splitting. *ChemSusChem* **2021**.

52. Paloukis, F.; Zafeiratos, S.; Drakopoulos, V.; Neophytides, S. G., Electronic Structure Modifications and HER of Annealed Electrodeposited Ni overlayers on Mo Polycrystalline Surface. *Electrochimica Acta* **2008,** *53* (27), 8015-8025.

53. Moniz, S. J. A.; Shevlin, S. A.; Martin, D. J.; Guo, Z.-X.; Tang, J., Visible-light Driven Heterojunction Photocatalysts for Water Splitting - a Critical Review. *Energy Environ. Sci.* **2015,** *8* (3), 731-759.

54. Schaefer, H.; Sadaf, S.; Walder, L.; Kuepper, K.; Dinklage, S.; Wollschlaeger, J.; Schneider, L.; Steinhart, M.; Hardege, J.; Daum, D., Stainless Steel Made to Rust: a Robust Water-splitting Catalyst with Benchmark Characteristics. *Energy Environ. Sci.* **2015,** *8* (9), 2685-2697.

55. Stern, L.-A.; Feng, L.; Song, F.; Hu, X., Ni_2P as a Janus Catalyst for Water Splitting: the Oxygen Evolution Activity of Ni_2P Nanoparticles. *Energy Environ. Sci.* **2015,** *8* (8), 2347-2351.

56. Tan, Y.; Wang, H.; Liu, P.; Shen, Y.; Cheng, C.; Hirata, A.; Fujita, T.; Tang, Z.; Chen, M., Versatile Nanoporous Bimetallic Phosphides towards Electrochemical Water Splitting. *Energy Environ. Sci.* **2016,** *9* (7), 2257-2261.

57. Che, W.; Cheng, W.; Yao, T.; Tang, F.; Liu, W.; Su, H.; Huang, Y.; Liu, Q.; Liu, J.; Hu, F.; Pan, Z.; Sun, Z.; Wei, S., Fast Photoelectron Transfer in (Cring)-C_3N_4 Plane Heterostructural Nanosheets for Overall Water Splitting. *J. Am. Chem. Soc.* **2017,** *139* (8), 3021-3026.

58. Duan, H.; Li, D.; Tang, Y.; He, Y.; Ji, S.; Wang, R.; Lv, H.; Lopes, P. P.; Paulikas, A. P.; Li, H.; Mao, S. X.; Wang, C.; Markovic, N. M.; Li, J.; Stamenkovic, V. R.; Li, Y., High-Performance Rh2P Electrocatalyst for Efficient Water Splitting. *J. Am. Chem. Soc.* **2017,** *139* (15), 5494-5502.

59. Feng, L.-L.; Yu, G.; Wu, Y.; Li, G.-D.; Li, H.; Sun, Y.; Asefa, T.; Chen, W.; Zou, X., High-Index Faceted Ni_3S_2 Nanosheet Arrays as Highly Active and Ultrastable Electrocatalysts for Water Splitting. *J. Am. Chem. Soc.* **2015,** *137* (44), 14023-14026.

60. Iwase, A.; Yoshino, S.; Takayama, T.; Ng, Y. H.; Amal, R.; Kudo, A., Water Splitting and CO_2 Reduction under Visible Light Irradiation Using Z-Scheme Systems Consisting of Metal Sulfides, CoO_x-Loaded $BiVO_4$, and a Reduced Graphene Oxide Electron Mediator. *J. Am. Chem. Soc.* **2016,** *138* (32), 10260-10264.

61. Li, J.; Wang, Y.; Zhou, T.; Zhang, H.; Sun, X.; Tang, J.; Zhang, L.; Al-Enizi, A. M.; Yang, Z.; Zheng, G., Nanoparticle Superlattices as Efficient Bifunctional Electrocatalysts for Water Splitting. *J. Am. Chem. Soc.* **2015,** *137* (45), 14305-14312.

62. Seo, J.; Takata, T.; Nakabayashi, M.; Hisatomi, T.; Shibata, N.; Minegishi, T.; Domen, K., Mg-Zr Cosubstituted Ta_3N_5 Photoanode for Lower-Onset-Potential Solar-Driven Photoelectrochemical Water Splitting. *J. Am. Chem. Soc.* **2015,** *137* (40), 12780-12783.

63. Tang, T.; Jiang, W.-J.; Niu, S.; Liu, N.; Luo, H.; Chen, Y.-Y.; Jin, S.-F.; Gao, F.; Wan, L.-J.; Hu, J.-S., Electronic and Morphological Dual Modulation of Cobalt Carbonate Hydroxides by Mn Doping toward Highly Efficient and Stable Bifunctional Electrocatalysts for Overall Water Splitting. *J. Am. Chem. Soc.* **2017,** *139* (24), 8320-8328.

64. Willinger, E.; Massue, C.; Schloegl, R.; Willinger, M. G., Identifying Key Structural Features of IrOx Water Splitting Catalysts. *J. Am. Chem. Soc.* **2017,** *139* (34), 12093-12101.

65. Sun, C.; Zhang, J.; Ma, J.; Liu, P.; Gao, D.; Tao, K.; Xue, D., N-doped WS_2 Nanosheets: a High-performance Electrocatalyst for the Hydrogen Evolution Reaction. *J. Mater. Chem. A* **2016,** *4* (29), 11234-11238.

66. Cao, S.; Liu, T.; Hussain, S.; Zeng, W.; Peng, X.; Pan, F., Hydrothermal Synthesis of Variety Low Dimensional WS_2 Nanostructures. *Materials Letters* **2014,** *129*, 205-208.

67. Lei, H.; Tan, S.; Ma, L.; Liu, Y.; Liang, Y.; Javed, M. S.; Wang, Z.; Zhu, Z.; Mai, W., Strongly Coupled $NiCo_2O_4$ Nanocrystal/MXene Hybrid through In Situ Ni/Co-F Bonds for Efficient Wearable Zn-Air Batteries. *ACS Appl Mater Interfaces* **2020**.

68. Xu, W.; Wang, R.; Zheng, B.; Wu, X.; Xu, H., New Family of Two-Dimensional Ternary Photoelectric Materials. *ACS Appl Mater Interfaces* **2019,** *11* (15), 14457-14462.

69. Guan, M.; Zhao, K.; Qiu, P.; Ren, D.; Shi, X.; Chen, L., Enhanced Thermoelectric Performance of Quaternary $Cu_{2-2x}Ag_{2x}Se_{1-x}S_x$ Liquid-like Chalcogenides. *ACS Appl. Mater. Interfaces* **2019,** *11* (14), 13433-13440.

70. Jiang, X.; Han, Y.; Zhang, H.; Liu, H.; Huang, Q.; Wang, T.; Sun, Q.; Li, Z., Cu-Fe-Se Ternary Nanosheet-Based Drug Delivery Carrier for Multimodal Imaging and Combined Chemo/Photothermal Therapy of Cancer. *ACS Appl. Mater. Interfaces* **2018,** *10* (50), 43396-43404.

71. Kong, F.; Ren, Z.; Norouzi Banis, M.; Du, L.; Zhou, X.; Chen, G.; Zhang, L.; Li, J.; Wang, S.; Li, M.; Doyle-Davis, K.; Ma, Y.; Li, R.; Young, A.; Yang, L.; Markiewicz, M.; Tong, Y.; Yin, G.; Du, C.; Luo, J.; Sun, X., Active and Stable Pt–Ni Alloy Octahedra Catalyst for Oxygen Reduction via Near-Surface Atomical Engineering. *ACS Catalysis* **2020,** *10* (7), 4205-4214.

72. Chao, D.; Liang, P.; Chen, Z.; Bai, L.; Shen, H.; Liu, X.; Xia, X.; Zhao, Y.; Savilov, S. V.; Lin, J.; Shen, Z. X., Pseudocapacitive Na-Ion Storage Boosts High Rate and Areal Capacity of

Self-Branched 2D Layered Metal Chalcogenide Nanoarrays. *ACS Nano* **2016,** *10* (11), 10211-10219.

73. Fan, K.; Zou, H.; Lu, Y.; Chen, H.; Li, F.; Liu, J.; Sun, L.; Tong, L.; Toney, M. F.; Sui, M.; Yu, J., Direct Observation of Structural Evolution of Metal Chalcogenide in Electrocatalytic Water Oxidation. *ACS Nano* **2018,** *12* (12), 12369-12379.

74. Mehta, R. J.; Karthik, C.; Singh, B.; Teki, R.; Borca-Tasciuc, T.; Ramanath, G., Seebeck Tuning in Chalcogenide Nanoplate Assemblies by Nanoscale Heterostructuring. *ACS Nano* **2010,** *4* (9), 5055-5060.

75. Moon, G. D.; Ko, S.; Xia, Y.; Jeong, U., Chemical Transformations in Ultrathin Chalcogenide Nanowires. *ACS Nano* **2010,** *4* (4), 2307-2319.

76. Smith, D. K.; Luther, J. M.; Semonin, O. E.; Nozik, A. J.; Beard, M. C., Tuning the Synthesis of Ternary Lead Chalcogenide Quantum Dots by Balancing Precursor Reactivity. *ACS Nano* **2011,** *5* (1), 183-190.

77. Tosun, M.; Chuang, S.; Fang, H.; Sachid, A. B.; Hettick, M.; Lin, Y.; Zeng, Y.; Javey, A., High-Gain Inverters Based on WSe2 Complementary Field-Effect Transistors. *ACS Nano* **2014,** *8* (5), 4948-4953.

78. Trivedi, T.; Roy, A.; Movva, H. C. P.; Walker, E. S.; Bank, S. R.; Neikirk, D. P.; Banerjee, S. K., Versatile Large-area Custom-feature van der Waals Epitaxy of Topological Insulators. *ACS Nano* **2017,** *11* (7), 7457-7467.

79. Wang, M.; Wu, J.; Lin, L.; Liu, Y.; Deng, B.; Guo, Y.; Lin, Y.; Xie, T.; Dang, W.; Zhou, Y.; Peng, H., Chemically Engineered Substrates for Patternable Growth of Two-Dimensional Chalcogenide Crystals. *ACS Nano* **2016,** *10* (11), 10317-10323.

80. Zhao, W.; Zhang, C.; Geng, F.; Zhuo, S.; Zhang, B., Nanoporous Hollow Transition Metal Chalcogenide Nanosheets Synthesized via the Anion-Exchange Reaction of Metal Hydroxides with Chalcogenide Ions. *ACS Nano* **2014,** *8* (10), 10909-10919.

81. Qiao, Y.; Yuan, P.; Hu, Y.; Zhang, J.; Mu, S.; Zhou, J.; Li, H.; Xia, H.; He, J.; Xu, Q., Sulfuration of an Fe-N-C Catalyst Containing Fe_xC/Fe Species to Enhance the Catalysis of Oxygen Reduction in Acidic Media and for Use in Flexible Zn-Air Batteries. *Adv Mater* **2018,** *30* (46), e1804504.

82. Han, C.; Sun, Q.; Li, Z.; Dou, S. X., Thermoelectric Enhancement of Different Kinds of Metal Chalcogenides. *Adv. Energy Mater.* **2016,** *6* (15), n/a.

83. Li, Y.; Xu, Y.; Wang, Z.; Bai, Y.; Zhang, K.; Dong, R.; Gao, Y.; Ni, Q.; Wu, F.; Liu, Y.; Wu, C., Stable Carbon-Selenium Bonds for Enhanced Performance in Tremella-Like 2D Chalcogenide Battery Anode. *Adv. Energy Mater.* **2018,** *8* (23).

84. Tian, H.; Yu, X.; Shao, H.; Dong, L.; Chen, Y.; Fang, X.; Wang, C.; Han, W.; Wang, G., Unlocking Few-layered Ternary Chalcogenides for High-performance Potassium-ion Storage. *Adv. Energy Mater.* **2019,** *9* (29), n/a.

85. Late, D. J.; Liu, B.; Matte, H. S. S. R.; Rao, C. N. R.; Dravid, V. P., Rapid Characterization of Ultrathin Layers of Chalcogenides on SiO_2/Si Substrates. *Adv. Funct. Mater.* **2012,** *22* (9), 1894-1905.

86. Mio, A. M.; Konze, P. M.; Meledin, A.; Kuepers, M.; Pohlmann, M.; Kaminski, M.; Dronskowski, R.; Mayer, J.; Wuttig, M., Impact of Bonding on the Stacking Defects in Layered Chalcogenides. *Adv. Funct. Mater.* **2019,** *29* (37).

87. Perumal, P.; Ulaganathan, R. K.; Sankar, R.; Liao, Y.-M.; Sun, T.-M.; Chu, M.-W.; Chou, F. C.; Chen, Y.-T.; Shih, M.-H.; Chen, Y.-F., Ultra-thin Layered Ternary Single Crystals [$Sn(S_xSe_{1-x})_2$] with Bandgap Engineering for High Performance Phototransistors on Versatile Substrates. *Adv. Funct. Mater.* **2016,** *26* (21), 3630-3638.

88. Wang, F.; Li, J.; Wang, F.; Shifa, T. A.; Cheng, Z.; Wang, Z.; Xu, K.; Zhan, X.; Wang, Q.; Huang, Y.; Jiang, C.; He, J., Enhanced Electrochemical H_2 Evolution by Few-Layered Metallic $WS_{2(1-x)}Se_{2x}$ Nanoribbons. *Adv. Funct. Mater.* **2015,** *25* (38), 6077-6083.

89. Yu, Y.; Cagnoni, M.; Cojocaru-Miredin, O.; Wuttig, M., Chalcogenide Thermoelectrics Empowered by an Unconventional Bonding Mechanism. *Adv. Funct. Mater.* **2020,** *30* (8), 1904862.

90. Zhang, S.; Xu, R.; Duan, W.; Zou, X., Intrinsic Half-Metallicity in 2D Ternary Chalcogenides with High Critical Temperature and Controllable Magnetization Direction. *Adv. Funct. Mater.* **2019,** *29* (14), 1808380.

91. Tiwari, A. P.; Kim, D.; Kim, Y.; Prakash, O.; Lee, H., Highly Active and Stable Layered Ternary Transition Metal Chalcogenide for Hydrogen Evolution Reaction. *Nano Energy* **2016,** *28*, 366-372.

92. Xia, C.; Jiang, Q.; Zhao, C.; Beaujuge, P. M.; Alshareef, H. N., Asymmetric Supercapacitors with Metal-like Ternary Selenides and Porous Graphene Electrodes. *Nano Energy* **2016,** *24*, 78-86.

93. Zhang, X.; Peng, N.; Liu, T.; Zheng, R.; Xia, M.; Yu, H.; Chen, S.; Shui, M.; Shu, J., Review on Niobium-based Chalcogenides for Electrochemical Energy Storage Devices: Application and Progress. *Nano Energy* **2019,** *65*, 104049.

94. Zhou, C.; Dun, C.; Wang, K.; Zhang, X.; Shi, Z.; Liu, G.; Hewitt, C. A.; Qiao, G.; Carroll, D. L., General Method of Synthesis Ultrathin Ternary Metal Chalcogenide Nanowires for Potential Thermoelectric Applications. *Nano Energy* **2016,** *30*, 709-716.

95. Cha, J. J.; Koski, K. J.; Huang, K. C. Y.; Wang, K. X.; Luo, W.; Kong, D.; Yu, Z.; Fan, S.; Brongersma, M. L.; Cui, Y., Two-Dimensional Chalcogenide Nanoplates as Tunable Metamaterials via Chemical Intercalation. *Nano Lett.* **2013,** *13* (12), 5913-5918.

96. Shi, L.; Tao, K.; Kawabata, T.; Shimamura, T.; Zhang, X. J.; Tsubaki, N., Surface Impregnation Combustion Method to Prepare Nanostructured Metallic Catalysts without Further Reduction: As-Burnt Co/SiO_2 Catalysts for Fischer–Tropsch Synthesis. *ACS Catalysis* **2011,** *1* (10), 1225-1233.

97. Zuo, T.; Gao, M. C.; Ouyang, L.; Yang, X.; Cheng, Y.; Feng, R.; Chen, S.; Liaw, P. K.; Hawk, J. A.; Zhang, Y., Tailoring Magnetic Behavior of CoFeMnNiX (X= Al, Cr, Ga, and Sn) High Entropy Alloys by Metal Doping. *Acta Materialia* **2017,** *130*, 10-18.

98. Kim, J.; Ko, W.; Yoo, J. M.; Paidi, V. K.; Jang, H. Y.; Shepit, M.; Lee, J.; Chang, H.; Lee, H. S.; Jo, J.; Kim, B. H.; Cho, S. P.; van Lierop, J.; Kim, D.; Lee, K. S.; Back, S.; Sung, Y. E.; Hyeon, T., Structural Insights into Multi-Metal Spinel Oxide Nanoparticles for Boosting Oxygen Reduction Electrocatalysis. *Adv Mater* **2021**, e2107868.

99. Wang, X.; Dong, Q.; Qiao, H.; Huang, Z.; Saray, M. T.; Zhong, G.; Lin, Z.; Cui, M.; Brozena, A.; Hong, M.; Xia, Q.; Gao, J.; Chen, G.; Shahbazian-Yassar, R.; Wang, D.; Hu, L., Continuous Synthesis of Hollow High-Entropy Nanoparticles for Energy and Catalysis Applications. *Adv Mater* **2020,** *32* (46), e2002853.

100. Zhao, F.; Zheng, L.; Yuan, Q.; Yang, X.; Zhang, Q.; Xu, H.; Guo, Y.; Yang, S.; Zhou, Z.; Gu, L.; Wang, X., Ultrathin PdAuBiTe Nanosheets as High-Performance Oxygen Reduction Catalysts for a Direct Methanol Fuel Cell Device. *Adv Mater* **2021,** *33* (42), e2103383.

101. Cui, M.; Yang, C.; Li, B.; Dong, Q.; Wu, M.; Hwang, S.; Xie, H.; Wang, X.; Wang, G.; Hu, L., High-Entropy Metal Sulfide Nanoparticles Promise High-Performance Oxygen Evolution Reaction. *Advanced Energy Materials* **2020,** *11* (3), 2002887.

102. Li, T.; Yao, Y.; Ko, B. H.; Huang, Z.; Dong, Q.; Gao, J.; Chen, W.; Li, J.; Li, S.; Wang, X.; Shahbazian-Yassar, R.; Jiao, F.; Hu, L., Carbon-Supported High-Entropy Oxide Nanoparticles as Stable Electrocatalysts for Oxygen Reduction Reactions. *Advanced Functional Materials* **2021,** *31* (21), 2010561.

103. Bondesgaard, M.; Broge, N. L. N.; Mamakhel, A.; Bremholm, M.; Iversen, B. B., General Solvothermal Synthesis Method for Complete Solubility Range Bimetallic and High-Entropy Alloy Nanocatalysts. *Advanced Functional Materials* **2019,** *29* (50), 1905933.

104. Nguyen, T. X.; Su, Y. H.; Lin, C. C.; Ting, J. M., Self-Reconstruction of Sulfate-Containing High Entropy Sulfide for Exceptionally High-Performance Oxygen Evolution Reaction Electrocatalyst. *Advanced Functional Materials* **2021**, 2106229.

105. Lou, X. D., Synergetic Cobalt-Copper-Based Bimetal-Organic Framework Nanoboxes toward Efficient Electrochemical Oxygen Evolution. *Angew Chem Int Ed Engl* **2021**, *60* (50), 26397-26402.

106. Amiri, A.; Shahbazian-Yassar, R., Recent Progress of High-entropy Materials for Energy Storage and Conversion. *Journal of Materials Chemistry A* **2021,** *9* (2), 782-823.

107. Lai, D.; Kang, Q.; Gao, F.; Lu, Q., High-entropy Effect of a Metal Phosphide on Enhanced overall Water Splitting Performance. *Journal of Materials Chemistry A* **2021,** *9* (33), 17913-17922.

108. Fang, G.; Gao, J.; Lv, J.; Jia, H.; Li, H.; Liu, W.; Xie, G.; Chen, Z.; Huang, Y.; Yuan, Q.; Liu, X.; Lin, X.; Sun, S.; Qiu, H.-J., Multi-component Nanoporous Alloy/(oxy)hydroxide for Bifunctional Oxygen Electrocatalysis and Rechargeable Zn-air Batteries. *Applied Catalysis B: Environmental* **2020,** *268*, 118431.

109. Ye, Q.; Feng, K.; Li, Z.; Lu, F.; Li, R.; Huang, J.; Wu, Y., Microstructure and Corrosion Properties of CrMnFeCoNi High Entropy Alloy Coating. *Applied Surface Science* **2017,** *396*, 1420-1426.

110. Turchi, P. E. A.; Kaufman, L.; Liu, Z.-K., Modeling of Ni–Cr–Mo Based Alloys: Part I—phase stability. *Calphad* **2006,** *30* (1), 70-87.

111. Li, H.; Lu, G.; Wang, Y.; Yin, Z.; Cong, C.; He, Q.; Wang, L.; Ding, F.; Yu, T.; Zhang, H., Mechanical Exfoliation and Characterization of Single- and Few-Layer Nanosheets of WSe_2, TaS_2, and $TaSe_2$. *Small* **2013,** *9* (11), 1974-1981.

112. Wang, F.; Zhang, Y.; Gao, Y.; Luo, P.; Su, J.; Han, W.; Liu, K.; Li, H.; Zhai, T., 2D Metal Chalcogenides for IR Photodetection. *Small* **2019,** *15* (30),1901347.

113. Zeng, Q.; Wang, H.; Fu, W.; Gong, Y.; Zhou, W.; Ajayan, P. M.; Lou, J.; Liu, Z., Band Engineering for Novel Two-Dimensional Atomic Layers. *Small* **2015,** *11* (16), 1868-1884.
114. Zhu, H.; Lai, Z.; Fang, Y.; Zhen, X.; Tan, C.; Qi, X.; Ding, D.; Chen, P.; Zhang, H.; Pu, K., Ternary Chalcogenide Nanosheets with Ultrahigh Photothermal Conversion Efficiency for Photoacoustic Theranostics. *Small* **2017,** *13* (16).
115. Liang, Q.; Zheng, Y.; Du, C.; Luo, Y.; Zhang, J.; Li, B.; Zong, Y.; Yan, Q., General and Scalable Solid-State Synthesis of 2D MPS_3 (M = Fe, Co, Ni) Nanosheets and Tuning Their Li/Na Storage Properties. *Small Methods* **2017,** *1* (12).
116. Xu, X.; Xu, W.; Zhang, L.; Liu, G.; Wang, X.; Zhong, W.; Du, Y., Interface engineering heterostructured MoS_2/WS_2-reduced graphene Oxide for enhanced hydrogen Evolution electrocatalysts. *Separation and Purification Technology* **2021,** *278*, 119569.
117. Kim, H.-U.; Kanade, V.; Kim, M.; Kim, K. S.; An, B.-S.; Seok, H.; Yoo, H.; Chaney, L. E.; Kim, S.-I.; Yang, C.-W.; Yeom, G. Y.; Whang, D.; Lee, J.-H.; Kim, T., Wafer-Scale and Low-Temperature Growth of 1T-WS_2 Film for Efficient and Stable Hydrogen Evolution Reaction. *Small* **2020,** *16* (6), 1905000.
118. Li, Y.; Yin, J.; An, L.; Lu, M.; Sun, K.; Zhao, Y. Q.; Gao, D.; Cheng, F.; Xi, P., FeS_2 /CoS_2 Interface Nanosheets as Efficient Bifunctional Electrocatalyst for Overall Water Splitting. *Small* **2018,** *14* (26), e1801070.
119. Leong, S. X.; Mayorga-Martinez, C. C.; Chia, X.; Luxa, J.; Sofer, Z.; Pumera, M., 2H --> 1T Phase Change in Direct Synthesis of WS_2 Nanosheets via Solution-Based Electrochemical Exfoliation and Their Catalytic Properties. *ACS Appl Mater Interfaces* **2017,** *9* (31), 26350-26356.
120. Shi, X.; Fields, M.; Park, J.; McEnaney, J. M.; Yan, H.; Zhang, Y.; Tsai, C.; Jaramillo, T. F.; Sinclair, R.; Noerskov, J. K.; Zheng, X., Rapid Flame Doping of Co to WS_2 for Efficient Hydrogen Evolution. *Energy Environ. Sci.* **2018,** *11* (8), 2270-2277.

Chapter 2. Bimetal heterojunction Fe_xS_y/WS_2 nanosheets electrocatalyst for energy-saving HER and water-splitting

2.1 Introduction

Hydrogen as one kind of energy source has advantages of high mass energy density and sustainable development, which has huge, promised prospect in clean energy source. Hydrogen evolution from electrochemical water-splitting method with environment friendly and recyclable usage characterizes has been recognized as a promised technology to replace traditional fossil fuels. Up to date, platinum based electrocatalysts exhibit excellent activity towards hydrogen evolution reaction (HER). However, the rare reserve on earth and exorbitant price of platinum makes it unsustainable and limit its wide application. Therefore, developing abundant and low-cost electrocatalysts with high efficiency for HER is promising urgent.

Tradition metal dichalcogenides (TMDs) with unique chemical and physical properties have received extensive focus to replace platinum as noble-meta-free HER electrocatalysts.[1-4] TMDs are a specific group of layered structure materials, which their layers are stacked together through weak van der Waal's forces and each layer consists of metal and sulfur or selenium atoms combined by covalent bond. Among the TMDs electrocatalysts, tungsten disulfide (WS_2) especially trigonal 1T phase WS_2 due to high-efficiency electrochemical properties are widely used as HER catalysts. However, many of common issues caused by the bulk structure limit further improving HER activity, which specifically including few exposed active sites, low electron conductivity and poor electrical contact with electrolyte. Numerous computational and experiments have been confirmed the HER catalytical active sites are located on the edges of two-dimensional (2D) WS_2 layers rather than the basal surfaces.[5-7] Many strategies have been taken to

further promote the HER activity of WS_2, such as exfoliating bulk WS_2 into WS_2 nanosheets to exposed more active sites[8] and other element atoms like N, Co[9] or Fe doping into WS_2 nanosheets to modify the electronic property. Though the above effects played role in further improving the WS_2 HER activity, the difficulty in operation, low production and high energy consumption limit the large-scale production. Very recently, interface engineering technology have been applied to develop high efficiency 2D compound TMDs electrochemical catalysts by constructing heterojunction structure.[10-13] It has been confirmed that the FeS_2/CoS_2[14] interface nanosheets electrocatalyst exhibited promoted HER activity compared with single FeS_2 and CoS_2, which is own to the rich defects of S vacancies in the heterojunction of FeS_2 and CoS_2. In addition, by constructing FeS_2/NiS_2 heterojunction, the fast electron transition could be realized between the interface of FeS_2 and NiS_2, which significantly improved the oxygen reduction reaction activity compared with single FeS_2 and NiS_2.[15-17] First-principle calculations had also demonstrated that the Gibbs free energy were reduced during HER process due to the strong interfacial interaction between the MoS_2/CoS_2 nanosheets heterointerfaces. In fact, the heterojunction could create an integrated electric field, which could facile the electron transfer between interfaces and the heterostructure could also optimize and active their activity by electronic modulation. Among the studied transition metals, Fe-based electrocatalysts were widely used because the abundant reserve and high efficiency.[18-20] Moreover, the high-spin d orbital of Fe could receive the π electron from the occupied low-spin d orbital of W in ferrotungsten sulfide, which could improve the HER activity. So far, it is rarely to reported iron and tungsten sulfides heterojunction catalyst for HER. Therefore, developing a facile method to prepared iron and tungsten sulfides heterojunction to further improve HER activity is promised.

Herein, we developed a novel iron tungsten sulfide heterojunction nanosheets (Fe_xS_y/WS_2 Ns) electrocatalyst by a facile hydrothermal method The obtained Fe_xS_y/WS_2 Ns showed a petal-like morphology with diameter of ~1 μm and 8 nm thickness of each flak. Benefitting from the thin structure and exposed active sites between interfaces, the Fe_xS_y/WS_2 Ns exhibited remarkable HER activity of overpotential for 118 mV at 10 mA cm^{-2} and a low Tafel slop of 87 mV dec^{-1} in 0.5 M H_2SO_4. Besides, an energy-saving 147 mV HER process could be achieved by replacing oxygen evolution reaction with urea oxidation reaction using Fe_xS_y/WS_2 Ns as bifunctional catalysts.

2.2 Materials and characterization information

2.2.1 Materials

Table 2.1 Experiment materials

Materials	Purity	Company
$FeCl_3 \cdot 6H_2O$	99.9%	Wako
CH_3CSNH_2	99.9%	Wako
WCl_6	99.9%	Wako
CH_2OHCH_2OH	99.9%	Wako
Deionized water	18.6 MΩ	Homemade
NH_2CONH_2	99.9%	Wako
KOH	99.9%	Wako

H_2SO_4	95 w%	Wako
Nafion	5 w% solution	Wako
CH_3CH_2OH	99.9%	Wako
$CH_3CHOHCH_3$	99.9%	Wako
Pt/C	20 w%	Wako

All the above-mentioned materials in Table S1 were purchased from the Wako. The regents and the relative solvent were directly used for the experiment without any change.

2.2.2 Materials characterization information

The scanning electron microscopy (SEM) and Energy-dispersive X-ray spectroscopy (EDS) characterizations were carried out on a field emission scanning electron microscope (Merlin, Germany). The transmission electron microscopy (TEM, JEOL JEM-F200) was used to take TEM images. X-ray diffraction (XRD) patterns were required from a Axis Petro analytical powder diffractometer by a Co Kα radiation. X-ray photoelectron spectroscopy (XPS) measurements were carried out by a Shimadzu AXIS-His instrument to determine the valance state of the materials. Raman spectra was carried out by a Laser Confocal Raman Microspectroscopy (wavelength = 532 nm, LabRAM HR Evolution).

2.2.3 Electrochemical characterization information

All the HER measurements of the electrocatalysts were explored by dropping the electrocatalysts ink on the surface of glass carbon. Specifically, 5 mg of electrocatalyst was added

into 500 μL ethanol and IPA aqueous solution, in which the volume ratio of ethanol, IPA, water and Nafion was 60: 15: 15: 10. The total concentration of the electrocatalyst is 10 mg mL^{-1}. After sonicating at room temperature for 2 h, the well dispersed electrocatalyst ink with high stability was prepared. For preparing the electrode for HER activity, 2 μL of the electrocatalyst ink was dropped slowly on the surface of glass carbon electrode and then the electrocatalyst ink dried under the infrared lamp. The diameter of the glass carbon electrode is 3 mm, thus, the loading amount of the electrocatalyst is about 0.3 mg cm^{-2}. For the energy-saving water-splitting reaction measurement, the electrodes were prepared by dropping 30 μL electrocatalyst ink onto the surface of carbon paper. The area of carbon paper is 1 cm^2. Therefore, the electrocatalyst loading amount is about 0.3 mg cm^{-2}.

For the HER activity measurement, a typical three-electrode system was allied to explore linear sweep voltammetry curve (LSV) and cyclic voltammetry (CV) curves, where a carbon rode was used for the counter electrode and Ag/Cl was used as the reference electrode. The LSV was carried out in the 0.5 M H_2SO_4 electrolyte with scan rate of 5 mV s^{-1}. Before the LSV measurement, 50 circles of CV process were carried out firstly to active the work electrode with scan rate of 5 mV s^{-1}. Electrochemical impedance spectroscopies (EIS) were investigated beginning 0.01 Hz toward 100 kHz. Electrochemical surface area (ECSA) measurements were carried out with different scan rates of 120, 100, 80, 60, 40, 20 mV s^{-1} with specific potential scale (- 0.08 V to - 0.18 V). The UOR measurement was the same with the HER measurement method.

For the urea oxidation reaction (UOR) measurement, the electrolysis was 1.0 M KOH with 0.5 M urea. The LSV curves were carried out with different scan rates of 5 mV s^{-1}, 20 mV s^{-1}, 40 mV s^{-1}, 60 mV s^{-1}, and 100 mV s^{-1}.

For the energy-saving water-splitting measurement, the process was carried in a two-electrode system, where both work electrode and counter electrode were the homemade carbon paper electrode with loading the responding electrocatalysts.

All the electrochemical measurements were recorded by the electrochemical work station CHI 760E.

2.3 Materials synthesis process

The process of synthesis was displayed in Figure 2.1. In details, 40 mL glycol aqueous solution (40 v%) was saturated with nitrogen gas for 30 min to remove oxygen. The 0.05 mmol of $FeCl_3 \cdot 6H_2O$ and 1 mmol of CH_3CSNH_2 (TAA) were added into the above solution and stirred for 30 min. The 0.1 mmol of WCl_6 was dissolved into above solution immediately and stirred for 30 min under the nitrogen atmosphere. The above solution after stirring was sealed into Teflon autoclave and heated to 195 °C for 20 h. After cooling into room temperature, the obtained samples were washed by centrifuging with carbon disulfide, ethanol, and water for several times. Finally, the bimetal heterojunction Fe_xS_y/WS_2 nanosheets were obtained after annealing process at 500 °C for 30 min. The temperature increasing rate of annealing process is 5 °C min^{-1}. Furthermore, the electrocatalysts with different ratio Fe and W were also prepared for the comparison. Different Fe and W ratios of 1:1 and 2:1 have also been taken to prepare Fe_xS_y/WS_2-1 and Fe_xS_y/WS_2-2. The pure WS_2 and Fe_xS_y were also prepared by the same experiment process only with difference of the single corresponding metal precursors.

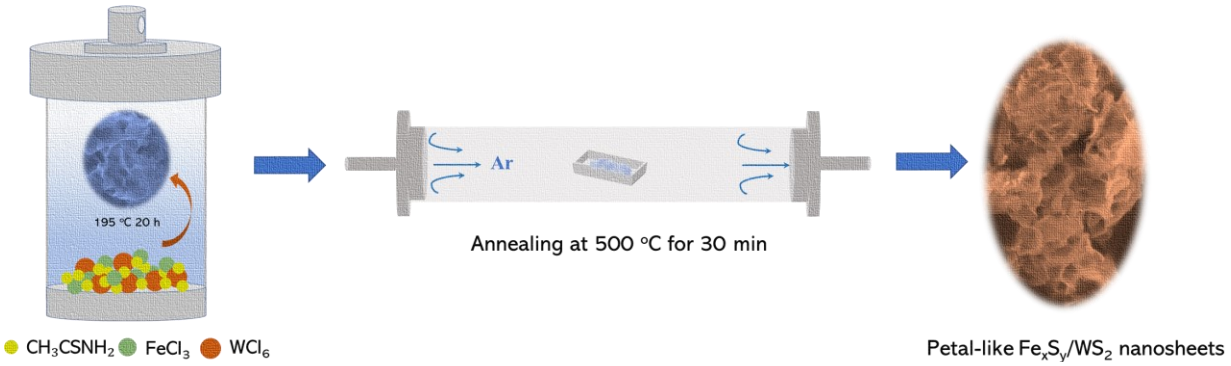

Figure 2.1. Schematic illustrations of preparing Fe_xS_y/WS_2 Ns.

Fe and W precursors reacted with TAA to form metal sulfides. Because S could be recognized as a bridge between metal sulfides, the Fe-S-W bond could be easy to form. Therefore, under the atmosphere of high temperature and pressure, the metal sulfides owned a high diffusion rate and combined with together to form Fe_xS_y/WS_2 interface. After hydrothermal process, the obtained materials were annealed at 500 °C and finally obtained Fe_xS_y/WS_2 Ns.

2.4 Morphonology and composition analysis results

2.4.1 Morphonology characterization results

The morphonology of prepared $FexS_2/WS_2$ as well as Fe_xS_y/WS_2-1 and Fe_xS_y/WS_2-2 were explored respectively. The scanning electron microscopy (SEM) images revealed that the prepared Fe_xS_y/WS_2 Ns owned a petal-like morphology with diameter of ~1 μm and 8 nm thickness of each flack (Figure 2.2a, b). The further obversion by transmission electron microscopy (TEM) was carried out to confirm the thin layered structure of obtained Fe_xS_y/WS_2 Ns. As shown in Figure 2.2c, the highly transparent area in TEM image for Fe_xS_y/WS_2 Ns showed a thin layer structure and the black grids on the surface of Fe_xS_y/WS_2 Ns which could be recognized as the specific petal structure, which also demonstrated that the obtained Fe_xS_y/WS_2 Ns owned a petal-like structure

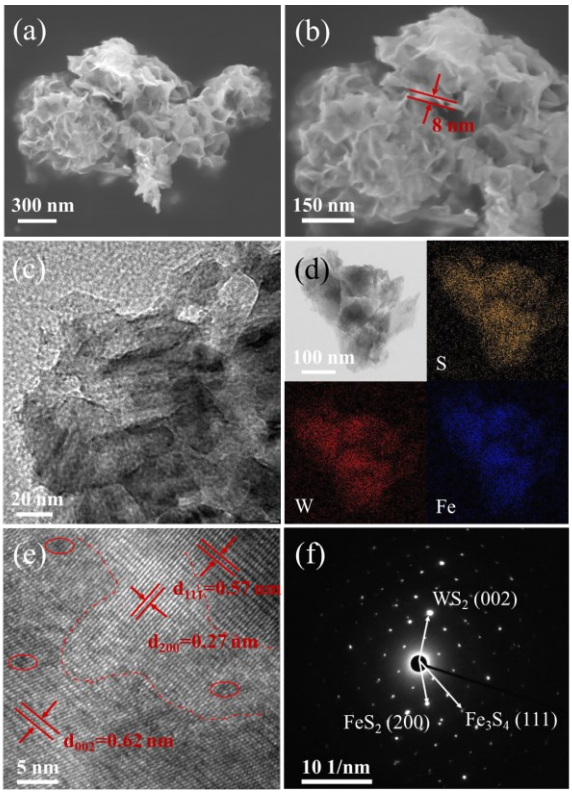

Figure 2.2. (a, b) SEM images of Fe_xS_y/WS_2 Ns. (c) TEM image of Fe_xS_y/WS_2 Ns. (d) TEM image and corresponding element mapping (S, W and Fe) for Fe_xS_y/WS_2 Ns. (e) HRTEM image of Fe_xS_y/WS_2 Ns. (f) SEAD image of Fe_xS_y/WS_2 Ns.

with thin layers. Energy-dispersive X-ray elemental mapping image shown in Figure 2.2d exhibited a uniform Fe, W and S dispersion throughout the Fe_xS_y/WS_2 Ns. The ratio of Fe, W and S was also confirmed to 1:1.85:11.98 by Energy-dispersive X-ray spectroscopy (EDS) shown in Figure 2.3. In order to further confirm the details of internal heterostructure in Fe_xS_y/WS_2 Ns, high-resolution TEM (HRTEM) images were carried out. As shown in Figure 2.2e, the distinct lattice fringes of Fe_xS_y/WS_2 Ns were displayed, indicating a high degree of crystallinity. Moreover, the lattice fringes with interplanar distance of 0.62 nm could be assign to the (002) plane of WS_2, while the lattice fringes with interplanar distance of 0.27 nm and 0.57 nm could be attributed to (200) plane of FeS_2 and (111) plane of Fe_3S_4 respectively. The boundary of different kinds of crystals

can be found clearly and marked by red dashed lines. Besides, some defects can be detected along with the lattice fringes, which were marked with red circle. Similar with HRTEM image, the selected area electron diffraction (SAED) pattern (Figure 2.2f) also exhibited regular and obvious electron diffraction points, which can be assigned to (002) plane of WS_2, (200) plane of FeS_2 and (111) plane of Fe_3S_4 respectively. The results directly demonstrated that the heterojunction was prepared successfully in Fe_xS_y/WS_2 Ns.

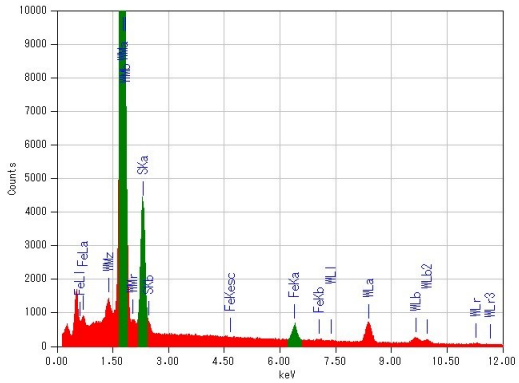

Elements	Electron energy (keV)	Wright %	Atom %
S K	2.307	32.57	80.761
Fe K	6.398	9.47	6.737
W M	1.774	57.96	12.502

Figure 2.3. The EDS spectra of Fe_xS_y/WS_2 Ns.

The morphonology of materials with different Fe, W ratios (Fe_xS_y/WS_2-1 and Fe_xS_y/WS_2-2) were also explored. As shown in Figure 2.4a and Figure 2.4b, the Fe_xS_y/WS_2-1 and Fe_xS_y/WS_2-2 also exhibited layered structure. However, the layers of Fe_xS_y/WS_2-1 and Fe_xS_y/WS_2-2 were aggregated and bulk structure compared that of the Fe_xS_y/WS_2 Ns (Figure 2.4c).

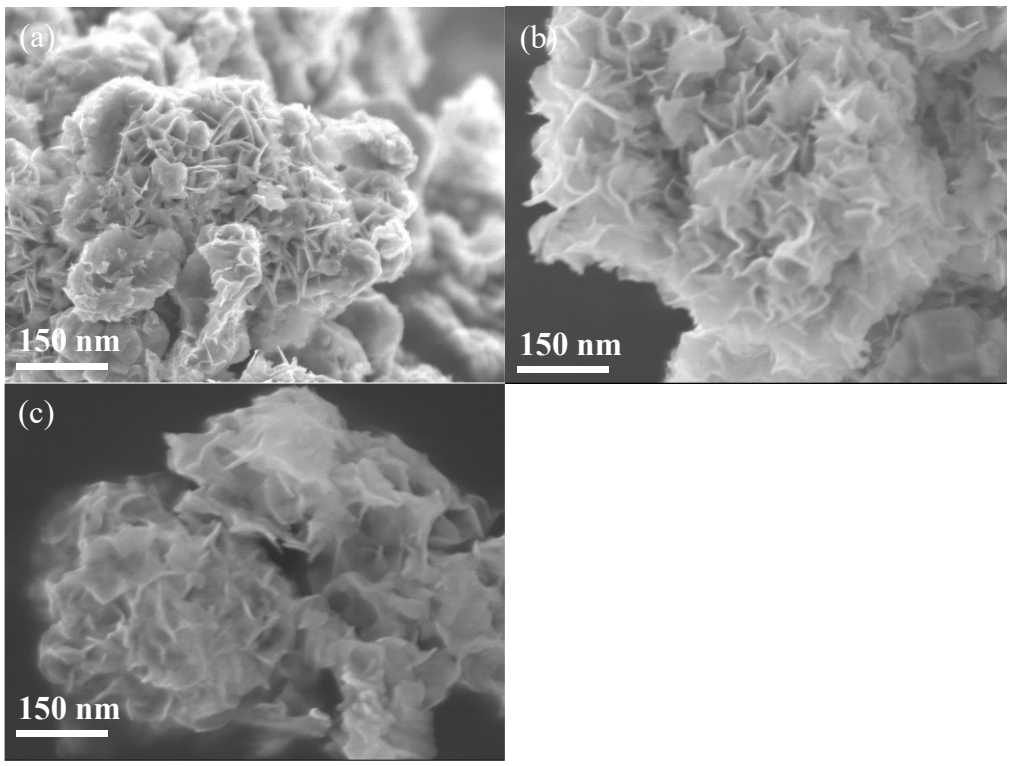

Figure 2.4. SEM images of (a) Fe_xS_y/WS_2-1, (b) Fe_xS_y/WS_2-2 and (c) Fe_xS_y/WS_2 Ns.

In addition, different with the layered structure of Fe_xS_y/WS_2 Ns, the SEM images of the Fe_xS_y (Figure 2.5a) and WS_2 (Figure 2.5b, c, and d) exhibited a bulk and aggregative morphonology. The SEM image with high magnification indicated that the materials with bulk morphology were formed by stacking numerous small, layered flakes along same direction (Figure 2.5b). SEM images (Figure 2.5c, d) also confirmed the morphology of WS_2 was layered flake structure but agglomerated together seriously. The insertion of Fe species weakened the electrostatic interaction with negatively charged of $[WS_2]^-$ species and decreased the entropy and surface energy of the hybrid system,[9, 21-24] thus prevented the agglomeration of WS_2 and finally prepared a uniform petal-like Fe_xS_y/WS_2 Ns. This similar phenomenon could also be reported in previous references. For example, the MoS_2/WS_2 exhibited nanoflower-like nanosheets

morphology, while WS_2 without Mo exhibited bulk and agglomerated flakes morphology (The introducing of Fe could increase the area of WS_2 nanosheets.

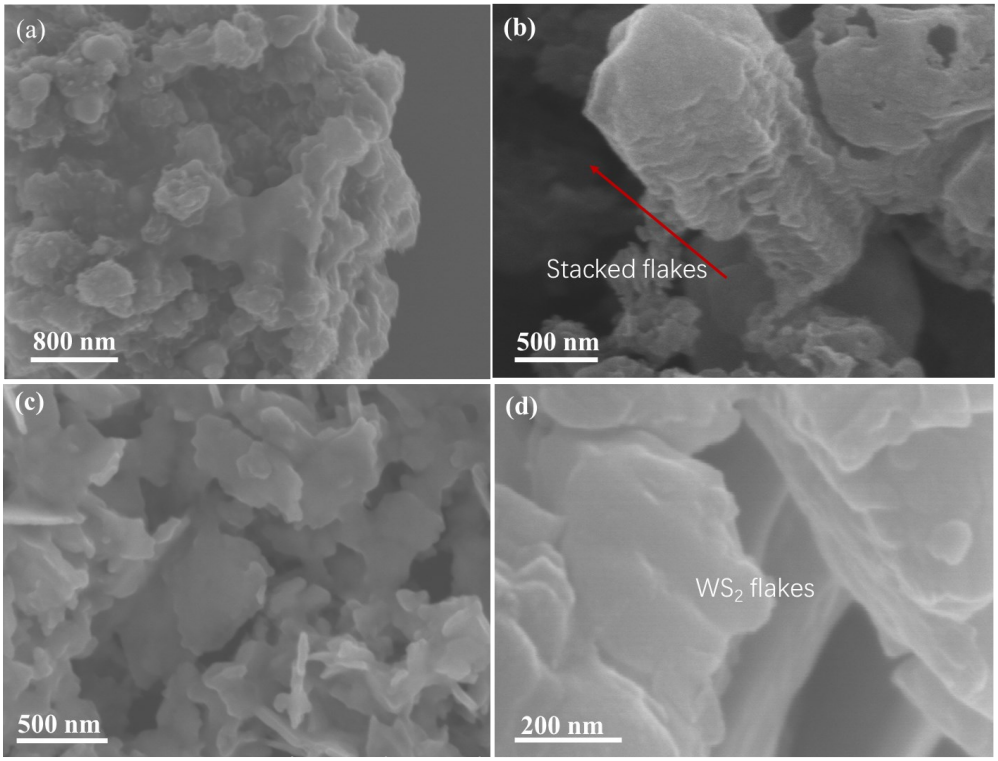

Figure 2.5. (a) SEM images of Fe_xS_y. (b-d) SEM images of WS_2.

In fact, as one of transition metal dichalcogenides (TMDs), the construction of WS_2 is is formed by stacking monolayer together along certain direction through van der Waals. Therefore, during the hydrothermal process, the WS_2 was easy to agglomerate and resulted in thick bulk morphology. By introducing different surfactants, WS_2 with different morphologies as well as thin layer nanosheets structure could be produced. However, in this work, we focused on introducing Fe specie to prepare heterojunction nanosheets. With the help of Fe, the prepared Fe_xS_y/WS_2 Ns exhibited thin and uniform petal-like structure compared with that of bulk and agglomerated morphology of Fe_xS_y and WS_2. At the same time of decreasing the thickness of WS_2, the Fe could also be recognized as active sites and further promoted the HER activity.

The above SEM images demonstrated that the prepared material possessed a thin layered structure with thickness of only 8 nm. The HRTEM image of the prepared material directly demonstrated that the heterojunction of WS_2 and Fe_xS_y (FeS_2 and Fe_3S_4) were prepared successfully. Therefore, the bimetal heterojunction Fe_xS_y/WS_2 Ns was prepared successfully.

2.4.2 Composition analysis results

To further understand the composition and the relationship of Fe, W, and S in Fe_xS_y/WS_2 Ns, the X-ray diffraction (XRD), Raman spectra and X-ray photoelectron spectroscopy (XPS) measurements were also performed (Figure 2.6).

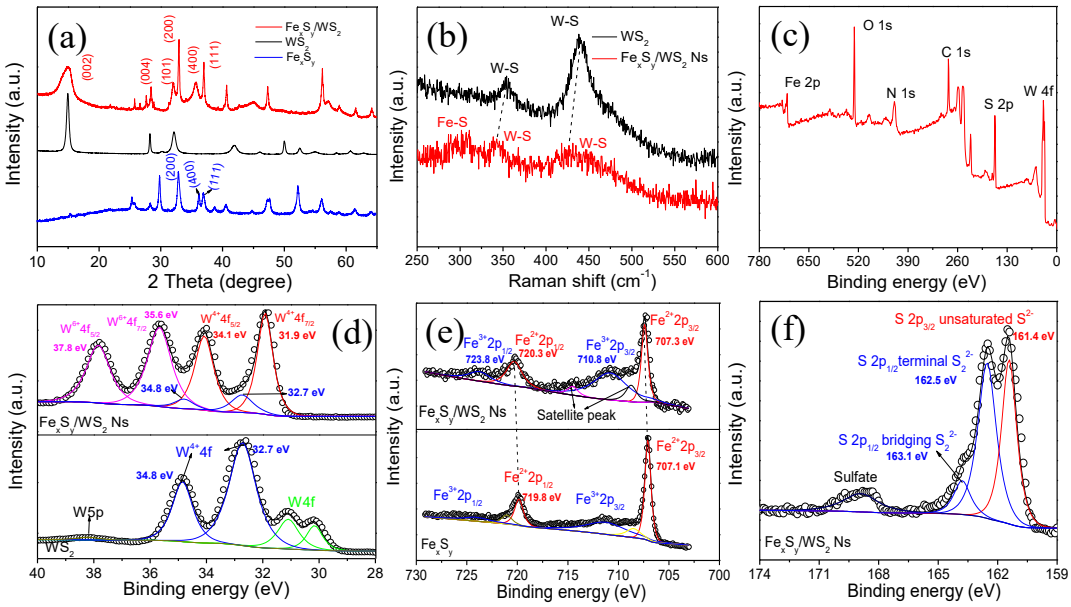

Figure 2.6. (a) XRD patterns of Fe_xS_y/WS_2 Ns, Fe_xS_y and WS_2. (b) Raman spectra of Fe_xS_y/WS_2 Ns. (c) XPS survey spectra of Fe_xS_y/WS_2 Ns. (d) High resolution W 4f XPS spectra of Fe_xS_y/WS_2 Ns and WS_2. (e) High resolution Fe 2p XPS spectra of Fe_xS_y/WS_2 Ns and Fe_xS_y. (f) High resolution S 2p XPS spectra of Fe_xS_y/WS_2 Ns.

The XRD diffraction peaks of Fe_xS_y/WS_2 Ns located at 32.9°, 35.6° and 37.1° were ascribed to Fe_xS_y. In fact, the Fe_xS_y was composed of FeS_2 and Fe_3S_4, because that the XRD diffraction peaks located at 32.9° and 32.9° were belonged to the (200) and (400) planes of FeS_2 and the XRD diffraction peak located at 37.1° was belonged to (111) plane of Fe_3S_4, which more specifically, The XRD pattern of Fe_xS_y matched well with that of FeS_2 (PDF#42-1340 and PDF#37-0475) and Fe_3S_4 (PDF#16-0713), indicated that the sample of Fe_xS_y was the composition of FeS_2 and Fe_3S_4. (Figure 2.7). The XRD diffraction peaks of Fe_xS_y/WS_2 Ns located at 14.8°, 28.3° and 32.2° can be attributed to (002), (004) and (101) planes of WS_2, which matched well that of WS_2 XRD pattern. The (002) planes of WS_2 were stacked with each other tightly along *c*-cix, which resulting in a strong XRD diffraction intensity. However, the intensity of XRD diffraction peak for (002) plane decreased in Fe_xS_y/WS_2 Ns compared with that of WS_2 XRD pattern, indicating the thin layer structure of Fe_xS_y/WS_2 Ns.[25=29]

Figure 2.6b displayed the specific series of Raman spectra of Fe_xS_y/WS_2 Ns and WS_2. The Raman spectra of Fe_xS_y/WS_2 Ns exhibited typical vibration of W-S with high wavenumbers of around 330 cm^{-1} and 440 cm^{-1}, which indicating the in-plane (E_{2g}^1) and out-of-plane (A_g^1) vibration of WS_2 Compared with the corresponding Raman spectra of WS_2, the blue shifted peaks with weak intensity of Fe_xS_y/WS_2 Ns also indicated the thin structure of Fe_xS_y/WS_2 Ns. In addition, a Fe-S with wavenumbers of 310 cm^{-1} can be found in Raman spectra of Fe_xS_y/WS_2 Ns, which was absent in WS_2 Raman spectra. The XRD results also confirmed the heterojunction of Fe_xS_y/WS_2 was prepared successfully. And the Raman spectra result also demonstrated the prepared Fe_xS_y/WS_2 exhibited a thin layered structure and a synergy effect between Fe and W species.

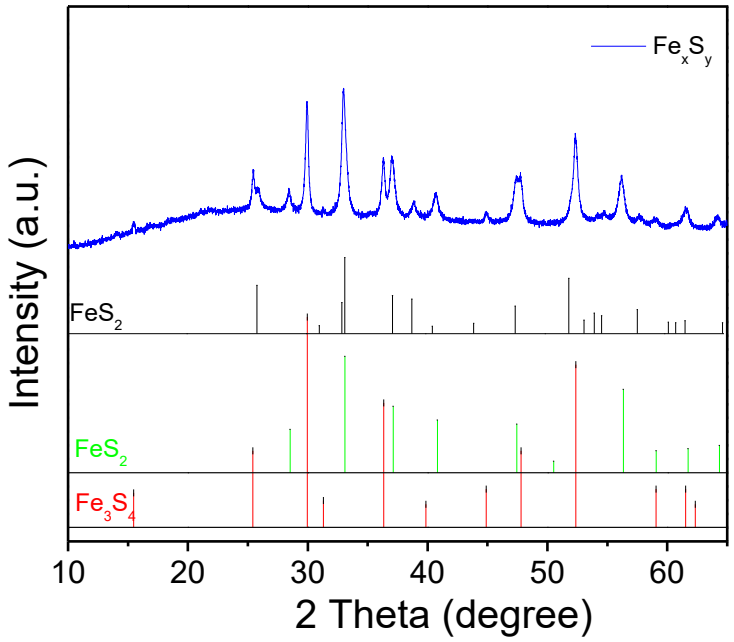

Figure 2.7. XRD pattern of Fe_xS_y

The XPS survey spectrum (Figure 2.6c) discovered the presence of W, Fe, O and S elements besides of C in Fe_xS_y/WS_2 Ns. As shown in Figure 2.6d, the high-resolution XPS spectra of W 4f for Fe_xS_y/WS_2 Ns mainly displayed tungsten species with two different states, which were the W^{4+} and W^{6+} respectively. A pair of peaks with lower binding energy centered at 31.9 eV and 34.1 eV were attributed to the W 4f of W^{4+} (31.9 eV for W $4f_{7/2}$ and 34.1 eV for W$4f_{5/2}$) in 1T WS_2. The doublet peaks of W 4f with higher binding energy located at 35.6 eV and 37.8 eV could be associated with W$4f_{7/2}$ and W $4f_{5/2}$ of W^{6+} respectively, which could be from the surface tungsten oxides caused by exposing under air atmosphere. Moreover, double peaks located at 34.8 eV and 32.7 eV could also be ascribed to the W 4f, which were the core levels of W $4f_{5/2}$ and W $4f_{7/2}$ in 2H phase WS_2. Compared with the W 4f XPS spectra of WS_2, the strong intensity and large area W 4f peaks of 1T WS_2 in Fe_xS_y/WS_2 Ns indicated that the Fe_xS_y/WS_2 Ns owned more ratio of electrocatalyst-efficiency 1T WS_2. The Fe intercalation with $[WS_2]^-$ during hydrothermal process played important role to the stabilization of 1T WS_2, in which the added Fe weakened the

electrostatic interaction with negatively charged of $[WS_2]^-$ species, thus cannot prevent its transformation to the thermodynamically stable 2H phase. That is the reason of different phase composition in Fe_xS_y/WS_2 Ns. The Fe 2p XPS spectra of Fe_xS_y/WS_2 Ns was displayed in Figure 2.6e, which exhibited that the 2p low spin orbital were divided into $2p_{1/2}$ and $2p_{2/3}$ respectively. Specifically, the double peaks located at binding energy of 707.3 eV (Fe $2p_{3/2}$) and 720.3 eV (Fe $2p_{1/2}$) were attributed to Fe^{2+}, while the peaks with higher binding energy centered at 710.8 eV (Fe $2p_{3/2}$) and 723.8 eV (Fe $2p_{1/2}$) were assigned with Fe^{3+}. These results indicated the Fe_xS_y/WS_2 Ns the valence species of Fe^{3+} and Fe^{2+}. As the contrast, the binding energies of Fe 2p (707.1 eV for Fe $2p_{3/2}$ and 719.8 eV for Fe $2p_{1/2}$) for Fe_xS_y were little downshifted than that of Fe_xS_y/WS_2 Ns, which indicating a strong interaction effect between Fe_xS_y and WS_2. The electron density of Fe_xS_y decreased in the Fe_xS_y/WS_2 Ns, suggesting the electrons transferred from Fe_xS_y to WS_2 at the interface, thus resulting in the binding energy increase of Fe 2p in Fe_xS_y/WS_2 Ns.

The S 2p XPS spectra of Fe_xS_y/WS_2 Ns shown in Figure 2.6f exhibited different sulfur atoms in various environments. Deconvoluted S 2p spectra showed three doublets shown in Figure 3e. Actually, one peak located at binding energy of 161.4 eV could be attributed to S $2p_{3/2}$, while other two peaks at binding energy of 162.5 eV and 163.1 eV could be attributed to S $2p_{1/2}$. To understand the specific sulfur surrounding in Fe_xS_y/WS_2 Ns, the kind of sulfur atom was investigated. The S2p peaks with binding energy of 161.4 eV, 162.5 eV and 163.1 eV were attributed unsaturated S^{2-}, terminal S_2^{2-} and bridging S_2^{2-} ligands, while peak with higher binding energy of 169.1 eV is attributed to surface oxide sulfate. However, the peak of bridging S_2^{2-} was not found besides the peaks of unsaturated S^{2-} (S $2p_{3/2}$) and terminal S_2^{2-} (S $2p_{1/2}$) in XPS spectra of Fe_xS_y and WS_2, which further confirmed the presence of Fe-S-W.[25, 30-31] Moreover, the increasing of the intensity

and area for the bridging S_2^{2-} ligands peaks in Fe_xS_y/WS_2 Ns suggested the presence of Fe-S-W, which are not found in the S2p XPS spectrums of Fe_xS_y and WS_2 (Figure 2.8).

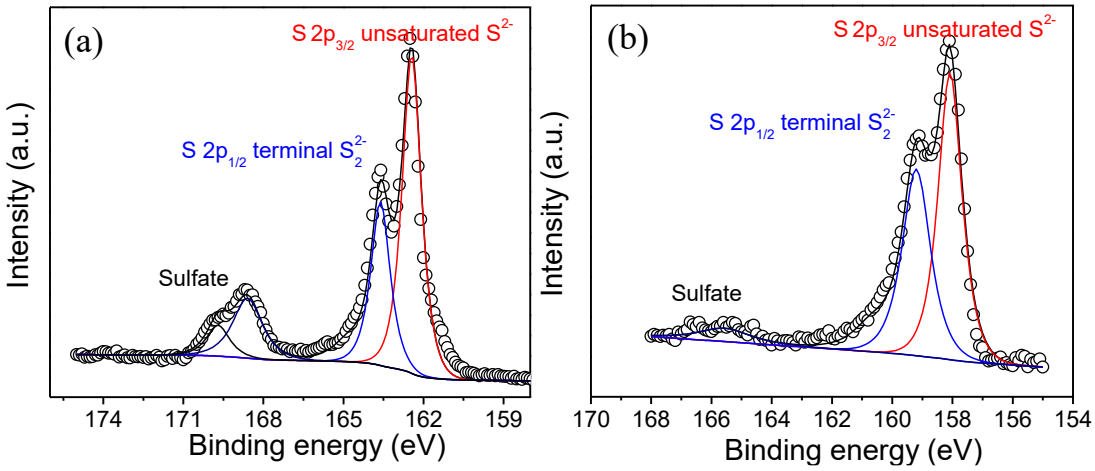

Figure 2.8. High resolution S 2p XPS spectra of (a) Fe_xS_y and (b) WS_2.

2.5 Electrochemical measurements results

2.5.1 HER performance in acidic solution

The HER activities of Fe_xS_y/WS_2 Ns, as well as the compared electrocatalysts (Fe_xS_y/WS_2-1, Fe_xS_y/WS_2-2, Fe_xS_y, WS_2, and Pt/C) were explored in 0.5 M H_2SO_4 by a typical three-electro system. All the mentioned potentials were converted into value versus RHE. As shown in Figure 2.9a, the linear sweep voltammetry (LSV) curves indicated the significantly promoted HER activity of Fe_xS_y/WS_2 Ns compared with that of Fe_xS_y and WS_2. Specifically, the overpotential at 10 mA cm^{-2} of Fe_xS_y/WS_2 Ns was 118 mV, while Fe_xS_y and WS_2 required a huge overpotential (>450 mV) to reach the current density of 10 mA cm^{-2}, suggesting the superior HER activity toward Fe_xS_y/WS_2 heterojunction in Fe_xS_y/WS_2 Ns. Moreover, the Fe_xS_y/WS_2 Ns with such low overpotential was favorably compared with those of recently reported electrocatalysts (Table S2.2).

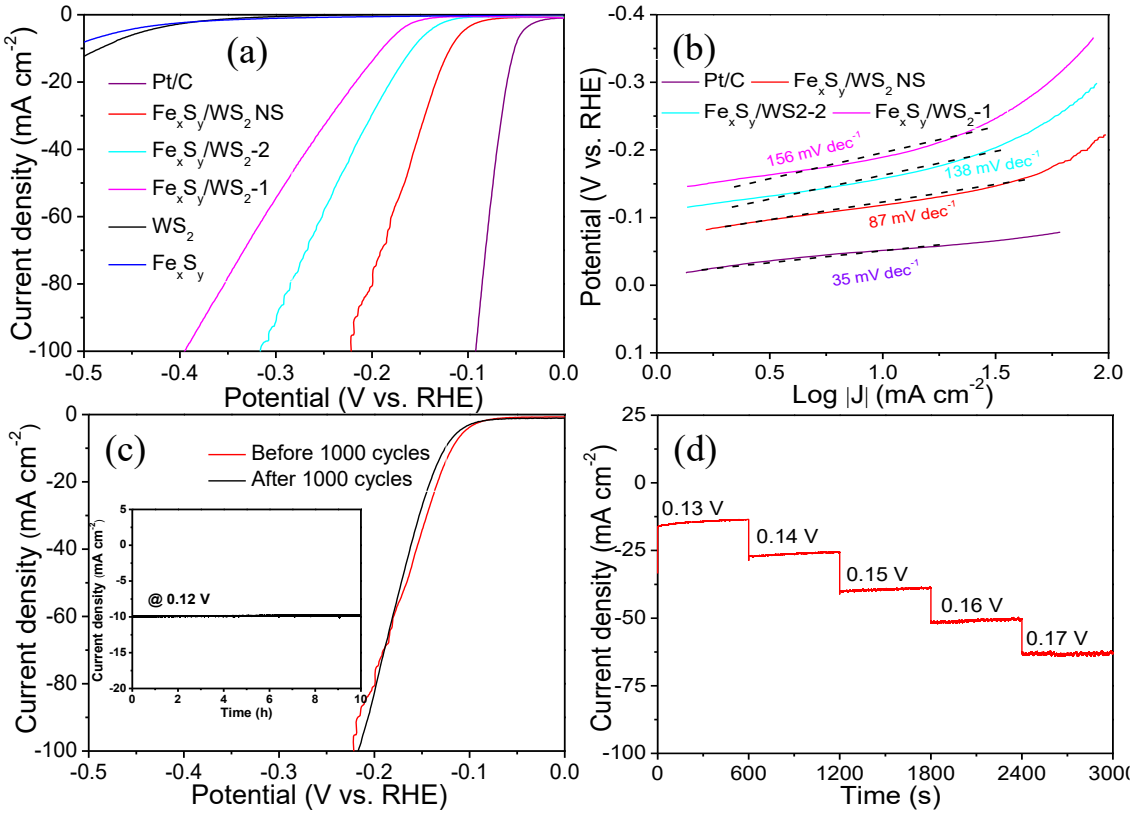

Figure 2.9. (a) Polarization curves of Fe_xS_y/WS_2 Ns, Fe_xS_y/WS_2-1, Fe_xS_y/WS_2-2, Fe_xS_y and WS_2. (b) Tafel slops Fe_xS_y/WS_2 Ns. Fe_xS_y/WS_2 Ns, Fe_xS_y/WS_2-1, Fe_xS_y/WS_2-2.. (c) Polarization curves of Fe_xS_y/WS_2 Ns before and after 3000 CV cycles. Insert: chronopotentiometric curve of e_xS_y/WS_2 Ns at a potential of -0.12 V. (d) Multistep-voltage curve of Fe_xS_y/WS_2 Ns.

At the same time, the HER performances of samples for Fe_xS_y/WS_2-1 and Fe_xS_y/WS_2-2 with Fe and W ratios of 1:1 and 2:1 respectively were also investigated. Though the HER activities of Fe_xS_y/WS_2-1 and Fe_xS_y/WS_2-2 have been promoted compared with Fe_xS_y and WS_2, the overpotentials at 10 mA cm^{-2} for Fe_xS_y/WS_2-1 and Fe_xS_y/WS_2-2 (191 and 157 mV respectively) were much higher than that of Fe_xS_y/WS_2 Ns (118 mV). The decreased overpotential of Fe_xS_y/WS_2 Ns demonstrated that the thin layered structure was more favorable for HER, while the layers of Fe_xS_y/WS_2-1 and Fe_xS_y/WS_2-2 were thick and aggregated (Figure 2.5). The Tafel slops were

calculated from the LSV curves (Figure 2.9b), which could be recognized as a crucial intrinsic property to investigate the HER performance. The Fe_xS_y/WS_2 Ns exhibited extremely low Tafel slop of 87 mV dec^{-1}, while 138 mV dec^{-1} and 156 mV dec^{-1} for Fe_xS_y/WS_2-2 and Fe_xS_y/WS_2-1 respectively, which indicating excellent electrocatalytic activity and favorable kinetics of Fe_xS_y/WS_2 Ns. Beside the excellent HER activity, the stability of the Fe_xS_y/WS_2 Ns electrocatalyst towards HER was also performance. The Fe_xS_y/WS_2 Ns also exhibited remarkable HER activity even after 1000 CV cycles (Figure 2.9c) and only 2% losses of the continuous current density after 10 hours chronopotentiometric measurement at 0.12 V (insert of 2.9c). Moreover, the stable current density for each potential increasing during the multistep-voltage measurement from 0.13 V to 0.17 V (Figure 2.9d), suggested the Fe_xS_y/WS_2 Ns owned remarkable transport property.

Table 2.2. HER performance comparison of recently reported electrocatalysts

Electrocatalyst	Overpotential (mV vs. RHE) at 10 mA cm^{-2}	Electrolyte	Reference
Fe_xS_y/WS_2 Ns	118	0.5 M H_2SO_4	This work
$W_xC@WS_2$	146	0.5 M H_2SO_4	*Adv. Funct. Mater.* **2017***, 27,* 1605802
WS_2-CoS_2	245	0.5 M H_2SO_4	Int. J. Hydrogen Energy **2019**, *44*, 809-818
WS_2/Graphite Foam	190	0.5 M H_2SO_4	*ACS Appl. Mater. Interfaces* **2017***, 9,* 30591-30598
Porous WS_2/WO_2 nanorods	147	0.5 M H_2SO_4	*ACS Catal.* **2016**, *6,* 6585-6590

WS_2/rGO nanosheets	246	0.5 M H_2SO_4	*Angew. Chem.* **2013**, *52,* 13751-13754.
$W(Se_xS_{1-x})_2$ nanoporous films	110	0.5 M H_2SO_4	*ACS Energy Lett.* **2017** *2,* 1315-1320
$WS_{2(1-x)}P_{2x}$ nanoribbons	98	0.5 M H_2SO_4	*Small* **2017**, *13,* 1603706

2.5.2 Electrochemical characterizations and mechanism study

To further understand the reason of the enhanced HER activity of Fe_xS_y/WS_2 Ns, the electrochemical active surface area (ECSA) and electrochemical impedance spectroscopy (EIS) were carried out.

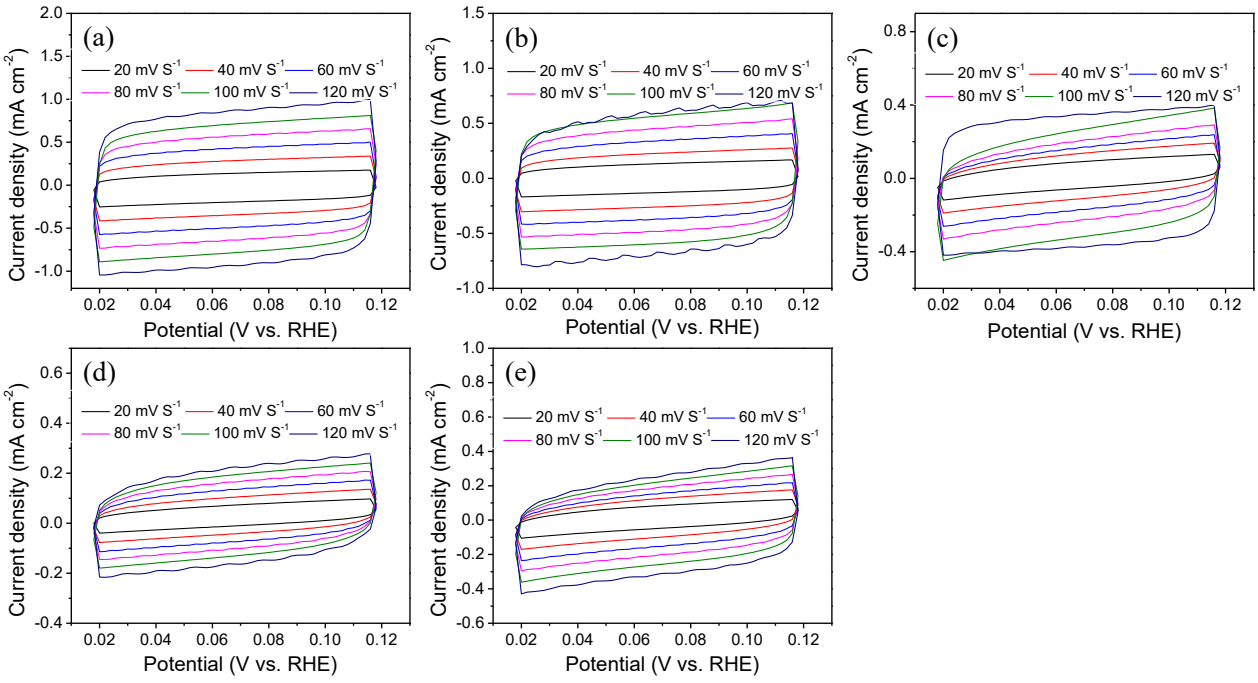

Figure 2.10. CV measurements of (a) Fe_xS_y/WS_2 Ns, (b) Fe_xS_y/WS_2-2, (c) Fe_xS_y/WS_2-1, Fe_xS_y and WS_2 (d, e) for ECSA.

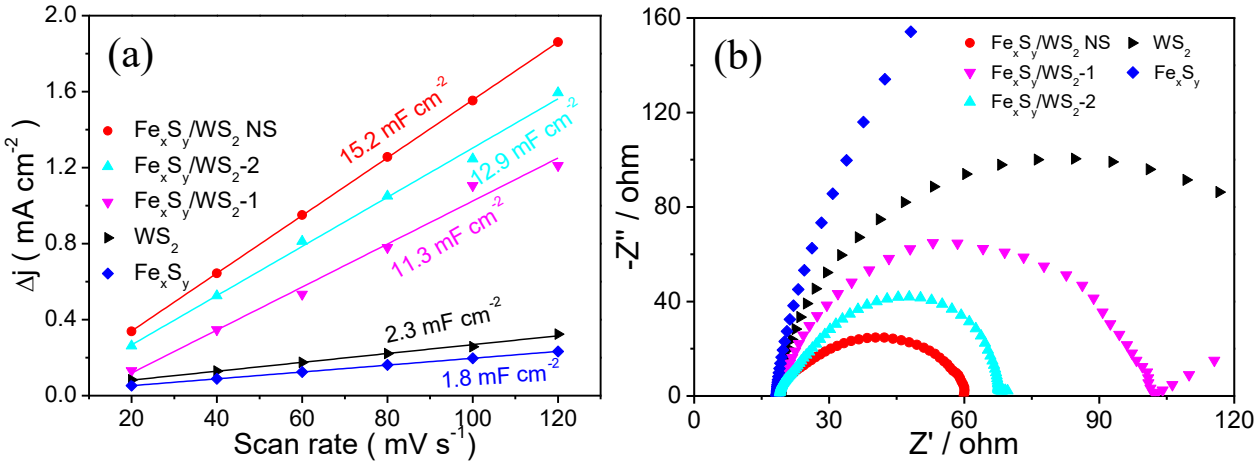

Figure 2.11. (a) ECSA and (b) EIS measurements of Fe_xS_y/WS_2 Ns, Fe_xS_y/WS_2-1, Fe_xS_y/WS_2-2, Fe_xS_y and WS_2.

The ECSA could be calculated from the value of double-layer capacitance (C_{dl}) between electrocatalysts and electrolyte by cyclic voltammetry method (Figure 2.10). As shown in Figure 2.11a, the Fe_xS_y/WS_2 Ns owned C_{dl} of 15.2 mF cm^{-2}, which was extremely greater than that of Fe_xS_y and WS_2 (1.8 and 2.3 mF cm^{-2} respectively). Likewise, the C_{dl} values of Fe_xS_y/WS_2-2 and Fe_xS_y/WS_2-1 were determined to 12.9 and 11.3 mF cm^{-2}. Which were smaller than that of Fe_xS_y/WS_2 Ns but significantly improved compared with that of Fe_xS_y and WS_2. In fact, the ECSA was corresponding to the catalytic active sites. The defects at the interface of Fe_xS_y/WS_2 in Fe_xS_y/WS_2 Ns (Figure 2.2) and thin layered structure provided numerous exposed active sites, which resulted in high C_{dl} and remarkable HER activity. Furthermore, electrochemical impedance spectroscopy (EIS) indicated the highest conductivity of Fe_xS_y/WS_2 Ns among Fe_xS_y/WS_2-2, Fe_xS_y/WS_2-1 as well as Fe_xS_y and WS_2 (Figure 2.11b). The EIS result suggested that the high electron transfer rate existed between interface of Fe_xS_y/WS_2 in Fe_xS_y/WS_2 Ns.

Therefore, the promoted HER activity of Fe_xS_y/WS_2 Ns could be recognized as the followed reasons: (a) the defects in Fe_xS_y/WS_2 Ns provided active sites and high charge transfer rate between

Fe_xS_y/WS_2 heterojunction resulted in rapid catalytic kinetic for Fe_xS_y/WS_2 Ns, both of which further improved the HER activity with low overpotential and accelerated the HER kinetic with small Tafel slop. (b) The thin petal-like structure of Fe_xS_y/WS_2 Ns could expose more active sites with a high ECSA and decreased the charge transfer distance, which improved the accessibility of catalytic active sites to reactants.

2.5.3 Energy-saving HER and water-splitting

Hydrogen evolution from water-splitting usually required the oxygen evolution reaction (OER) on the anodic side, which was a crucial speed-limiting process. Therefore, the OER activity in 1.0 M KOH of Fe_xS_y Ns was also explored. However, with the efficient HER activity, the Fe_xS_y/WS_2 Ns displayed poor OER performance with overpotential of 414 mV at 10 mA cm^{-2} in 1.0 M KOH (Figure 2.12a), which limited the usage of Fe_xS_y/WS_2 Ns as bifunctional electrocatalyst for water-splitting. With this problem, the oxidation reaction of more favorable species such as urea (CH_4N_2O) replaced the OER to promote the anodic reaction and decreased the anode overpotential at 10 mA cm^{-2} from 414 mV to 340 mV (Figure 2.12a), suggesting the Fe_xS_y/WS_2 Ns could act as an efficient electrocatalyst for urea oxidation reaction (UOR).[4] In addition, The almost overlapped LSV curves (Figure 2.12b) indicated the negligible influence of urea on the HER activity. The UOR rate capability of Fe_xS_y/WS_2 Ns was further studied by tuning the scan rate of 5, 20, 40, 60 and 100 mV s^{-1} (Figure 2.12c). The current density and the scan rate maintain a good linear relationship at 1.70 V vs. RHE (Figure 2.12d), which indicated that UOR is a surface-controlled process with highly efficient charge and mass transfer.

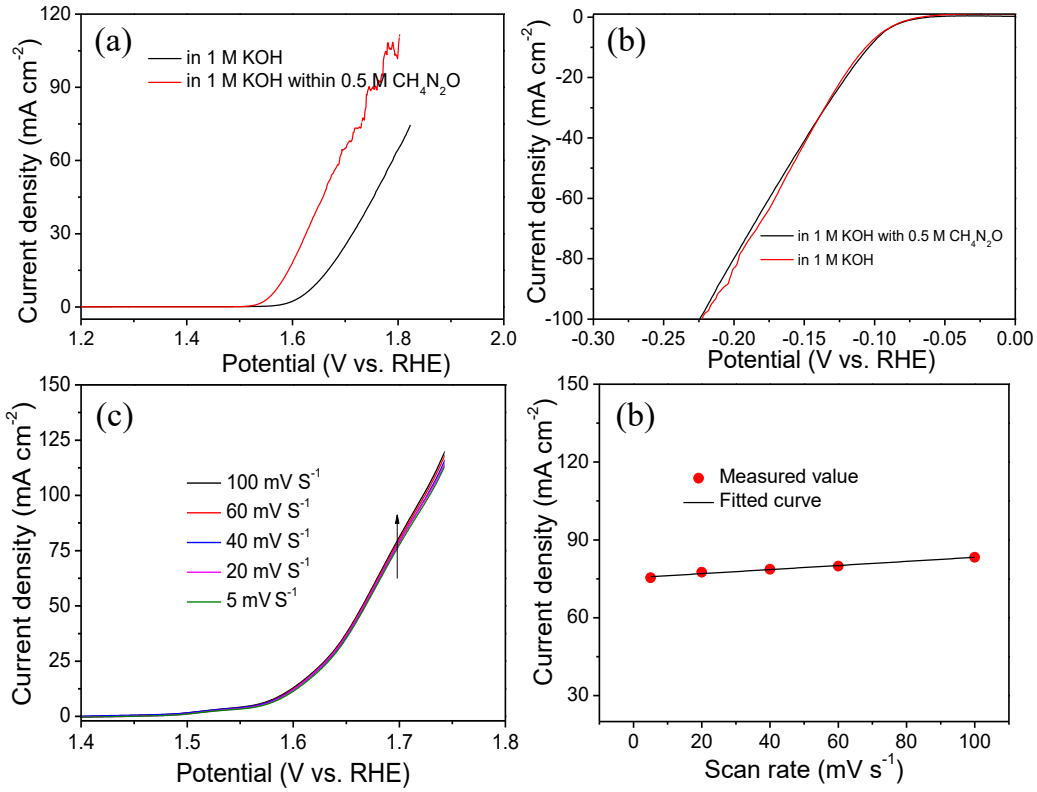

Figure 2.12. (a) Polarization curves of Fe_xS_y/WS_2 Ns for OER and UOR. (b) HER LSV of Fe_xS_y/WS_2 Ns in 1.0 M KOH with and without urea. (c) UOR polarization curves of Fe_xS_y/WS_2 Ns recorded at different scan rates. (d) The linear dependence of the current density measured at 1.7 V vs. RHE on the scan rate.

According to the above results, an energy-saving HER water-splitting device was designed with Fe_xS_y/WS_2 Ns as bifunctional electrocatalyst for HER at cathode and UOR at anode (Figure 2.13a). As shown in the device of energy-saving water-splitting device, a two-electrode system was applied for the HER at cathode and UOR at anode. The electrolysis at the cathode section is the 1.0 M KOH, while the electrolysis at the anode section is the 1.0 M KOH with 0.5 M urea. A Nafion membrane was used to separate these two different kinds of electrolysis. As shown in Figure 2.13b, an energy-saving HER process could be enable by Fe_xS_y/WS_2 Ns as bifunctional electrocatalyst for HER at cathode and UOR at anode using a two-electrode system. Notably, by

replacing OER with UOR, the potential decreased 147 mV at the prescience of CH_4N_2O. Besides, a continuous 10 hours chronopotentiometric measurement also demonstrated the energy-saving HER process owned good stability at 1.8 V (Figure 2.13c).

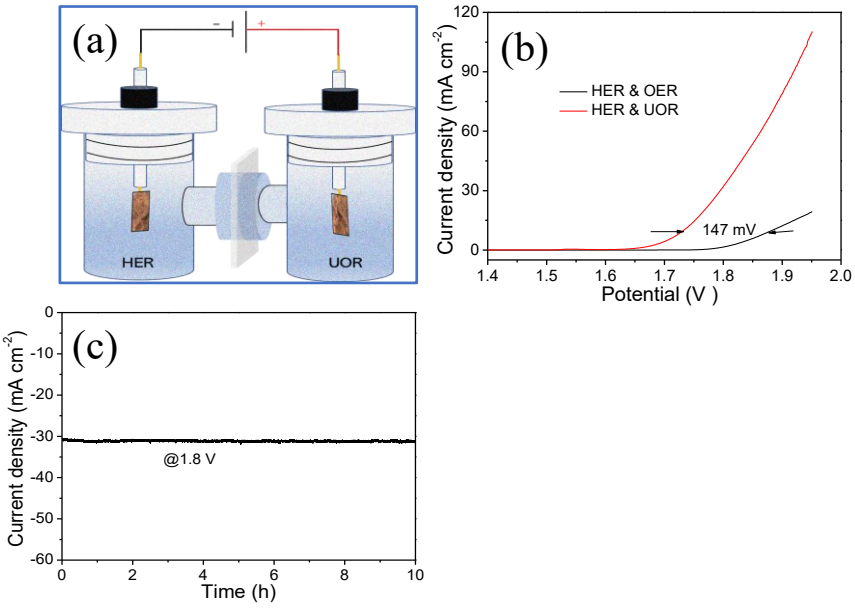

Figure 2.13. (a) The schematic diagram of device, in which the Fe_xS_y/WS_2 Ns as bifunctional electrocatalyst for HER at cathode and UOR at anode. (b) Polarization curves of bifunctional Fe_xS_y/WS_2 Ns for energy-saving HER process with urea and without urea through a two-electrode system. (c) Chronopotentiometric curve of bifunctional Fe_xS_y/WS_2 Ns for energy-saving HER process at 1.8 V.

2.6 Conclusions

In summary, a novel petal-like Fe_xS_y/WS_2 heterojunction nanosheets with diameter of ~1 μm and thickness of 8 nm was developed through a facial hydrothermal method. The defects in Fe_xS_y/WS_2 Ns provided numerous active sites, resulting in an enhanced HER activity with overpotential of 118 mV. Benefiting from the fast charge rate between Fe_xS_y/WS_2 heterojunction

and thin layered structure, the Fe_xS_y/WS_2 Ns exposed more active sites and exhibited excellent HER catalytic kinetic with Tafel slop of 87 mV dec^{-1} and high conductivity. Moreover, the Fe_xS_y/WS_2 Ns as bifunctional electrocatalyst could realize a 147-mV energy-saving HER process at cathode by replacing OER with UOR at anode. This work could provide a way to further improve the catalytic activity of TMDs electrocatalysts.

Outcomes of our work and interest to others in the field:

1. The petal-like Fe_xS_y/WS_2 Ns with a lateral size of ~1 μm and thickness of 8 nm exhibited an excellent HER activity in 0.5 M H_2SO_4, featured by a low overpotential of 118 mV at current density of 10 mA cm^{-2} and a low Tafel slope of 87 mV dec^{-1}, which is the almost best performance among all previously reported WS_2-based HER electrocatalysts. Furthermore, the Fe_xS_y/WS_2 Ns bifunctional electrocatalyst act as both anode and cathode, enabling urea oxidation reaction (UOR) instead of oxygen evolution reaction (OER) to energy-efficient HER.
2. XRD patterns indicated that the Fe_xS_y/WS_2 was compound by WS_2 and Fe_xS_y, while the Fe_xS_y was FeS_2 and Fe_3S_4. The HRTEM images displayed numerous defects and clear crystal plane boundary of WS_2 and Fe_xS_y in Fe_xS_y/WS_2 Ns. Raman spectrum and XPS results further demonstrated the presence of Fe_xS_y/WS_2 heterojunction. Electrochemical results revealed that the highly exposed active sites and fast electron transfer rates of Fe_xS_y/WS_2 Ns contributed to the high HER activity.
3. This Fe_xS_y/WS_2 Ns presented in this work provides ideas for promating catalytic activity of other TMDs materials and promising potentials in many important applications, such as CO_2 reduction reaction, nitrogen reduction reaction, and oxygen reduction reaction.

We believe that this interface engineering method will be of broad interest to scientists and engineers working in transition metal dichalcogenides and have significant impact in the fundamental research of bifunctional catalysts in electrochemical water splitting.

References

1. Aslan, E.; Sarilmaz, A.; Yanalak, G.; Ozel, S. S.; Ozel, F.; Patir, I. H., Transition Metal–incorporated Tungsten-based Ternary Refractory Metal Selenides ($MWSe_x$; M = Fe, Co, Ni, and Mn) as Hydrogen Evolution Catalysts at Soft Interfaces. *Materials Today Energy* **2020,** *18*, 100510.
2. Han, A.; Zhou, X.; Wang, X.; Liu, S.; Xiong, Q.; Zhang, Q.; Gu, L.; Zhuang, Z.; Zhang, W.; Li, F.; Wang, D.; Li, L.-J.; Li, Y., One-step Synthesis of Single-site Vanadium Substitution in 1T-WS_2 Monolayers for Enhanced Hydrogen Evolution Catalysis. *Nat. Commun.* **2021,** *12* (1), 709.
3. Li, Z.; Li, B.; Liu, Z.; Liu, Z.; Li, D., A Tungsten Carbide/iron Sulfide/FePt Nanocomposite Supported on Nitrogen-doped Carbon as An Efficient Electrocatalyst for Oxygen Reduction Reaction. *RSC Adv.* **2015,** *5* (128), 106245-106251.
4. Zhou, L.; Yan, S.; Song, H.; Wu, H.; Shi, Y., Multivariate Control of Effective Cobalt Doping in Tungsten Disulfide for Highly Efficient Hydrogen Evolution Reaction. *Sci Rep* **2019,** *9* (1), 1357.
5. Yan, S.; Wang, K.; Zhou, F.; Lin, S.; Song, H.; Shi, Y.; Yao, J., Ultrafine Co:FeS_2/CoS_2 Heterostructure Nanowires for Highly Efficient Hydrogen Evolution Reaction. *ACS Applied Energy Materials* **2019,** *3* (1), 514-520.
6. Fu, L.; Xiong, W.; Liu, Q.; Wan, S.; Kang, C.; Li, G.; Chu, J.; Chen, Y.; Yuan, S., Metal-organic Framework Derived FeS/MoS_2 Composite as A High Performance Anode for Sodium-ion Batteries. *Journal of Alloys and Compounds* **2021,** *869*, 159348.
7. Fan, K.; Zou, H.; Dharanipragada, N. V. R. A.; Fan, L.; Inge, A. K.; Duan, L.; Zhang, B.; Sun, L., Surface and Bulk Reconstruction of CoW Sulfides During pH-universal Electrocatalytic Hydrogen Evolution. *Journal of Materials Chemistry A* **2021,** *9* (18), 11359-11369.
8. Jing, Z.; Zhao, Q.; Zheng, D.; Sun, L.; Geng, J.; Zhou, Q.; Lin, J., Nickel-doped Pyrrhotite Iron Sulfide Nanosheets as A Highly Efficient Electrocatalyst for Water Splitting. *Journal of Materials Chemistry A* **2020,** *8* (39), 20323-20330.

9. Shang, X.; Chi, J.-Q.; Lu, S.-S.; Dong, B.; Li, X.; Liu, Y.-R.; Yan, K.-L.; Gao, W.-K.; Chai, Y.-M.; Liu, C.-G., Novel Co_xS_y/WS_2 Nanosheets Supported on Carbon Cloth as Efficient Electrocatalyst for Hydrogen Evolution Reaction. *International Journal of Hydrogen Energy* **2017,** *42* (7), 4165-4173.

10. Fonseca, H. A. B.; Verga, L. G.; Da Silva, J. L. F., Ab Initio Study of CO_2 Activation on Pristine and Fe-Decorated WS_2 Nanoflakes. *J Phys Chem A* **2021,** *125* (36), 7769-7777.

11. Yang, Y.; Liu, J.; Liu, F.; Wang, Z.; Wu, D., FeS_2-anchored Transition Metal Single Atoms for Highly Efficient overall Water splitting: A DFT Computational Screening Study. *J. Mater. Chem. A* **2021,** *9* (4), 2438-2447.

12. Cai, M.; Han, J.; Lin, Y.; Liu, W.; Luo, X.; Zhang, H.; Zhong, M., CoS_2-incorporated WS_2 Nanosheets for Efficient Hydrogen Production. *Electrochimica Acta* **2018,** *287*, 1-9.

13. Tran, P. D.; Chiam, S. Y.; Boix, P. P.; Ren, Y.; Pramana, S. S.; Fize, J.; Artero, V.; Barber, J., Novel Cobalt/nickel–tungsten-sulfide Catalysts for Electrocatalytic Hydrogen Generation from Water. *Energy & Environmental Science* **2013,** *6* (8), 2452.

14. Lukowski, M. A.; Daniel, A. S.; English, C. R.; Meng, F.; Forticaux, A.; Hamers, R. J.; Jin, S., Highly Active Hydrogen Evolution Catalysis from Metallic WS_2 Nanosheets. *Energy Environ. Sci.* **2014,** *7* (8), 2608-2613.

15. Ding, R.; Chen, Q.; Luo, Q.; Zhou, L.; Wang, Y.; Zhang, Y.; Fan, G., Salt template-assisted in situ Construction of Ru Nanoclusters and Porous carbon: Excellent Catalysts toward Hydrogen Evolution, Ammonia-borane Hydrolysis, and 4-nitrophenol reduction. *Green Chemistry* **2020,** *22* (3), 835-842.

16. Sun, L.; Gao, M.; Jing, Z.; Cheng, Z.; Zheng, D.; Xu, H.; Zhou, Q.; Lin, J., 1 T-Phase Enriched P Doped WS_2 Nanosphere for Highly Efficient Electrochemical Hydrogen Evolution Reaction. *Chemical Engineering Journal* **2022,** *429*, 132187.

17. Sun, L.; Geng, J.; Gao, M.; Zheng, D.; Jing, Z.; Zhao, Q.; Lin, J., Novel $WS_2/Fe_{0.95}S_{1.05}$ Hierarchical Nanosphere as a Highly Efficient Electrocatalyst for Hydrogen Evolution Reaction. *Chemistry* **2021**.

18. Jin, J.; Yin, J.; Liu, H.; Xi, P., Synthesis of Silk-like FeS_2/NiS_2 Hybrid Nanocrystals with Improved Reversible Oxygen Catalytic Performance in A Zn-air battery. *Chinese Journal of Catalysis* **2019,** *40* (1), 43-51.

19. Zhang, G.; Hao, Z.; Yin, J.; Wang, C.; Zhang, J.; Zhao, Z.; Wei, D.; Zhou, H.; Li, Z., FeS_2 Crystal Lattice Promotes the Nanostructure and Enhances the Electrocatalytic Performance of WS_2 Nanosheets for the Oxygen Evolution Reaction. *Dalton Trans* **2020,** *49* (28), 9804-9810.

20. Zhao, X.; Ma, X.; Lu, Q.; Li, Q.; Han, C.; Xing, Z.; Yang, X., FeS_2-doped MoS_2 Nanoflower with the Dominant 1T-MoS_2 Phase as An Excellent Electrocatalyst for High-performance Hydrogen Evolution. *Electrochim. Acta* **2017,** *249*, 72-78.

21. Chen, H.; Chen, J.; Si, J.; Hou, Y.; Zheng, Q.; Yang, B.; Li, Z.; Gao, L.; Lei, L.; Wen, Z.; Feng, X., Ultrathin Tin Monosulfide Nanosheets with the Exposed (001) Plane for Efficient Electrocatalytic Conversion of CO_2 into Formate. *Chem Sci* **2020,** *11* (15), 3952-3958.

22. Li, S.; Zang, W.; Liu, X.; Pennycook, S. J.; Kou, Z.; Yang, C.; Guan, C.; Wang, J., Heterojunction Engineering of $MoSe_2$/MoS_2 with Electronic Modulation toward Synergetic Hydrogen Evolution Reaction and Supercapacitance Performance. *Chemical Engineering Journal* **2019,** *359*, 1419-1426.

23. Zhang, Y.; Wang, D.; Wang, S., High-Entropy Alloys for Electrocatalysis: Design, Characterization, and Applications. *Small* **2021**, e2104339.

24. Nourmohammadi Khiarak, B.; Shariati, K.; Mojaddami, M.; Zamani, Z.; Zekiy, A. O.; Simchi, A., Efficient Electrocatalytic Overall Water Splitting on a Cu-Based High Entropy Alloy: An Electrochemical Study. *SSRN Electronic Journal* **2021**.

25. Liu, H.; Syama, L.; Zhang, L.; Lee, C.; Liu, C.; Dai, Z.; Yan, Q., High-entropy Alloys and Compounds for Electrocatalytic Energy Conversion Applications. *SusMat* **2021,** *1* (4), 482-505.

26. Huo, W.-Y.; Wang, S.-Q.; Zhu, W.-H.; Zhang, Z.-L.; Fang, F.; Xie, Z.-H.; Jiang, J.-Q., Recent Progress on High-entropy Materials for Electrocatalytic Water Splitting Applications. *Tungsten* **2021,** *3* (2), 161-180.

27. Sahlberg, M.; Karlsson, D.; Zlotea, C.; Jansson, U., Superior Hydrogen Storage in High Entropy Alloys. *Sci Rep* **2016,** *6*, 36770.

28. Yao, Y.; Huang, Z.; Xie, P.; Lacey, S. D.; Jacob, R. J.; Xie, H.; Chen, F.; Nie, A.; Pu, T.; Rehwoldt, M.; Yu, D.; Zachariah, M. R.; Wang, C.; Shahbazian-Yassar, R.; Li, J.; Hu, L., Carbothermal Shock Synthesis of High-entropy-alloy Nanoparticles. *Science* **2018,** *359* (6383), 1489-1494.

29. Jin, Z.; Lv, J.; Jia, H.; Liu, W.; Li, H.; Chen, Z.; Lin, X.; Xie, G.; Liu, X.; Sun, S.; Qiu, H. J., Nanoporous Al-Ni-Co-Ir-Mo High-Entropy Alloy for Record-High Water Splitting Activity in Acidic Environments. *Small* **2019,** *15* (47), e1904180.

30. He, Q. F.; Wang, J. G.; Chen, H. A.; Ding, Z. Y.; Zhou, Z. Q.; Xiong, L. H.; Luan, J. H.; Pelletier, J. M.; Qiao, J. C.; Wang, Q.; Fan, L. L.; Ren, Y.; Zeng, Q. S.; Liu, C. T.; Pao, C. W.; Srolovitz, D. J.; Yang, Y., A Highly Distorted Ultraelastic Chemically Complex Elinvar alloy. *Nature* **2022,** *602* (7896), 251-257.

31. Glasscott, M. W.; Pendergast, A. D.; Goines, S.; Bishop, A. R.; Hoang, A. T.; Renault, C.; Dick, J. E., Electrosynthesis of High-entropy Metallic Glass Nanoparticles for Designer, Multi-Functional Electrocatalysis. *Nat Commun* **2019,** *10* (1), 2650.

32. Li, H.; Han, Y.; Zhao, H.; Qi, W.; Zhang, D.; Yu, Y.; Cai, W.; Li, S.; Lai, J.; Huang, B.; Wang, L., Fast Site-to-site Electron Transfer of High-entropy Alloy Nanocatalyst Driving Redox Electrocatalysis. *Nat Commun* **2020,** *11* (1), 5437.

Chapter 3. Development bifunctional quinary NiFeCoMnCu high entropy alloy electrocatalyst for alkalic OER and HER

3.1 Introduction

Hydrogen with properties of high energy density and zero CO_2 emission is promised to be a desirable energy source, which could overcome challenges of global energy and environmental crises. In recent years, hydrogen evolution from electrochemical water-splitting is a green and sustainable pathway to generate hydrogen. The electrochemical water-splitting reaction is heavily dependent on high effective electrocatalysts because both of hydrogen evolution reaction (HER) and oxygen evolution reaction (OER) occurred on cathode and anode require high-efficiency electrocatalysts to decrease the overpotential. Though Pt-based materials exhibit excellent HER activity, but the expensive cost limits their usage on electrochemical water-splitting reaction.[6] Ru-based and Ir-based materials process very outstanding OER activity. However, rare reserves on earth and intolerable price also preclude their wide application for electrochemical water-splitting reaction.[7] Therefore, developing high efficiency and low-cost electrocatalysts for electrochemical water-splitting is promising and urgent.

Transition metal-based electrochemical water-splitting catalysts experienced the process from the monometallic-based materials (such as Fe, Co, Ni, etc.) to bimetallic-based materials (such as NiFe, CoFe, MnFe, etc.) and sequentially to the trimetallic-based materials (such as CoFeW, NiFeCo, etc.).[1-4] Although these non-precious metals based electrocatalysts were reported with high efficiency and promised to replace noble metal-based electrocatalysts, the specific effect of each metal element for promoting the activity in multimetallic electrocatalysts has still not been fully clarified. Moreover, most studies about transition metal electrochemical catalysts reported

compositions not exceeding three elements because of the difficulties of combining immiscible elements. High entropy alloys (HEAs) are referred to as those alloys that contained at least five specific elements, in which each element has an atomic concentration ratio between 5% to 35%. Different from transition metal-based electrocatalysts,[5-6] HEAs as electrocatalysts with unique chemical and physical properties have received significant attention, which includes a various selection of elements, high chemical and thermal stability, multi-active sites, and large configuration entropy.[7] Notably, due to the combination of various catalytically effective elements with different atomic sizes, the strong lattice inside HEAs provides high potential energy, which results in relatively low barrier energy for the catalytic reaction. In addition, various elements were alloyed together with desired distance and position between the center active atoms and neighboring atoms, thus, the intermediates or the adsorption energies of species could be tuned in HEAs. As a result, this synergy effect in HEAs could play an important role in OER and HER performances. However, strategies for the synthesis of HEAs remain a challenge, because of difficulties in mixing different elements and avoiding the aggregation and migration phenomena. Over the past years, high-energy ball milling and solid-phase alloying are simple methods for large-scale production, but the size and morphology of HEAs are out of control.[7-11] Carbothermal shock, laser melting, and arc melting methods could prepare desired HEAs rapidly. However, the generation of HEAs with extremely high temperature limits the large-scale production. Recently, the wet impregnation method with its advantages of low ease for operation and high controllability has been recognized as the most popular strange to produce HEAs, which could be recognized as a promised operative method for large-scale production. Nevertheless, materials with multi-ligands such as 1,10-Phenanthroline and Poly(N-vinyl-2-pyrrolidone) used for aggregating metal precursors widely are noxious and harmful to the environment. Critic acid (CA) as a natural

material has a unique combination of halide salts to form hydrogen-bond networks. Up to now, using critic acid to polymerize metal precursor is significant and rare reported.[12-13]

Herein, we developed a novel and facile critic acid polymerization strategy that followed the pyrolysis process to direct synthesis of Fe, Co, Ni, Cu, and Mn high entropy alloys (NiFeCoMnCu HEAs). Benefiting from the more effective reducing and chelating agents of critic acid (-OH and -COOH groups), the Fe, Co, Ni, Cu, and Mn halide salts are chelated with critic acid through a hydrogen bond to form a homogeneous aqueous solution, which overcomes the immiscibility of different metals and polymerizes them uniformly inside chemical gelation spontaneously, thus results in a single-phase high entropy alloy after pyrolysis process. Benefiting from the more exposed active sites, high conductivity, and unique synergistic effect between different metal species, the prepared NiFeCoMnCu HEAs exhibited excellent OER and HER activity with low overpotential at 10 mA cm^{-2} of 240 mV and 165 mV in 1.0 M KOH respectively. As the bifunctional electrocatalyst, an effective electrochemical water-splitting reaction could be realized by NiFeCoMnCu HEAs, which only required 1.5 V to reach a current density of 10 mA cm^{-2}. In addition, a favorable sea water-splitting reaction also could be enabled by the bifunctional NiFeCoMnCu HEAs electrocatalyst.

3.2 Materials and characterization information

3.2.1 Materials

Table 3.1 Experiment materials

Materials	Purity	Company

$FeCl_3 \cdot 6H_2O$	99.9%	Wako
$NiCl_2 \cdot 6H_2O$	99.9%	Wako
$MnCl_2 \cdot 4H_2O$	99.9%	Wako
$CuCl_2 \cdot 2H_2O$	99.9%	Wako
Deionized water	18.6 MΩ	Homemade
$CoCl_2 \cdot 6H_2O$	99.9%	Wako
KOH	99.9%	Wako
H_2SO_4	95 w%	Wako
Nafion	5 w% solution	Wako
$NH_3 \cdot H_2O$	25 w%	Wako
RuO_2	20 w%	Wako
Pt/C	20 w%	Wako
Citric acid	99.9 %	Wako
CH_3CH_2OH	99.9%	Wako
$CH_3CHOHCH_3$	99.9%	Wako

All the above-mentioned materials in Table S1 were purchased from the Wako. The regents and the relative solvent were directly used for the experiment without any change.

3.2.2 Materials characterization information

The transmission electron microscopy (TEM, JEOL JEM-F200) was used to take TEM images. X-ray diffraction (XRD) patterns were required from the Axis Petro analytical powder diffractometer by a Co Kα radiation. X-ray photoelectron spectroscopy (XPS) measurements were carried out by a Shimadzu AXIS-His instrument to determine the valance state of the materials. ICP-OES was carried out on SHIMADZU.

3.2.3 Electrochemical characterization information

All the OER measurements of the electrocatalysts were explored by dropping the electrocatalysts ink on the surface of carbon paper. Specifically, 5 mg of electrocatalyst was added into 500 μL ethanol and IPA aqueous solution, in which the volume ratio of ethanol, IPA, water and Nafion was 60: 15: 15: 10. The total concentration of the electrocatalyst is 10 mg mL^{-1}. After sonicating at room temperature for 2 h, the well dispersed electrocatalyst ink with high stability was prepared. For preparing the electrode for OER activity, 30 μL of the electrocatalyst ink was dropped slowly on the surface of carbon paper electrode and then the electrocatalyst ink dried under the infrared lamp. The area of the carbon paper electrode is 0.5 cm^{-2}, thus, the loading amount of the electrocatalyst is about 0.6 mg cm^{-2}. Before dropping electrocatalysts ink on the surface of carbon paper, the carbon paper was washed with ethanol and water several times under sonication. Then the cleaned carbon paper was dry at 60 ^{o}C under vacuum.

For the OER activity measurement, a typical three-electrode system was allied to explore linear sweep voltammetry curve (LSV) and cyclic voltammetry (CV) curves, where a carbon rode was used for the counter electrode and Ag/Cl were used as the reference electrode. The LSV was carried out in the 1.0 M KOH electrolysis with scan rate of 5 mV s^{-1}. Before the LSV measurement,

50 circles of CV process were carried out firstly to active the work electrode with scan rate of 5 mV s^{-1}. Electrochemical impedance spectroscopies (EIS) were investigated beginning 0.01 Hz toward 100 kHz. Electrochemical surface area (ECSA) measurements were carried out with different scan rates of 120, 100, 80, 60, 40, 20 mV s^{-1} with specific potential scale (1.11 V to 1.21 V).

In addition, all the process of preparing electrode for HER was the same as that of OER. All the electrochemical measurements were recorded by the electrochemical workstation CHI 760E.

3.3 Materials synthesis process

As shown in Figure 3.1, the 7.5 mmol of citric acid was firstly dissolved into a 50 mL nitrogen saturated ethanol aqueous solution (20 v%) and stirred for 30 min. Then Equal amounts of metal precursors ($NiCl_2 \cdot 6H_2O$, $FeCl_3 \cdot 6H_2O$, $MnCl_2 \cdot 4H_2O$, $CuCl_2 \cdot 2H_2O$, and $CoCl_2 \cdot 6H_2O$, total amount of 0.5 mmol) were slowly added into the above solution at the sequence of Mn, Fe, Co, Ni, and Cu. After 1 h stirring process, the obtained solution was refluxed at 80 ºC for 2 h. When the solution cooled down to room temperature, the mixed solution was evaporated at 70 ºC for 3 h. Finally, the NiFeCoMnCu HEAs was prepared after a pyrolysis process under a nitrogen atmosphere, in which the temperature was firstly increased to 150 ºC for 2 h with 3 ºC min^{-1} and then increased to 800 ºC for 1 h with 10 ºC min^{-1}. The unary Ni, binary NiFe, ternary NiFeCo, and quaternary NiFeCoMn were also prepared by the same method for comparison.

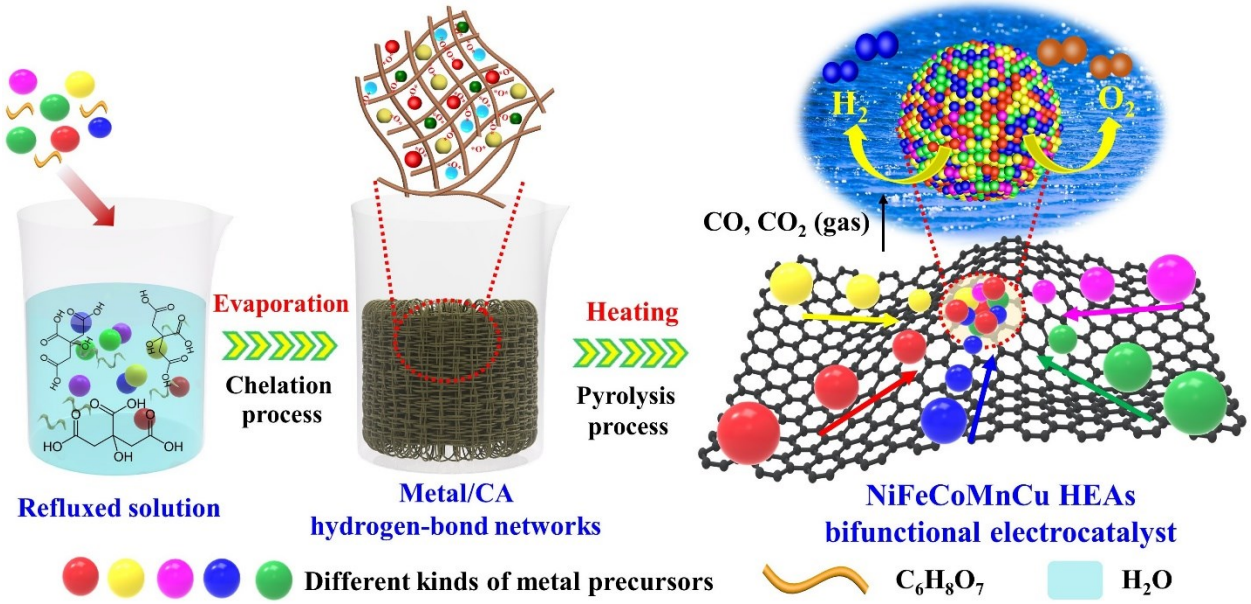

Figure 3.1. The process of preparing NiFeCoMnCu HEAs.

The citric acid ($C_6H_8O_7$, CA) as one of the complexants possesses many -COOH and -OH groups, which could chelate halide salts to form homogeneous polymetallic networks. After the reflux and evaporation process, CA polymerized with metal chlorides and formed a homogeneous network through hydrogen-bond, which efficiently avoided the aggregation of metal chlorides. The synthetic mechanism is driven by the metal salts decomposing and the release of CO gas:[14-18]

$$MCl_xH_y \rightarrow M + \text{gases} \uparrow$$

$$C + O^* \rightarrow CO \uparrow$$

Where the O^* indicated the surface-bound residual oxygen. During the pyrolysis process, a carbon metabolism reaction could be formed, including carbon (fuel), metal (catalyst), and O^* (oxidizer). Mechanistically, the metals with catalytic sites could accelerate vigorous carbon metabolism reaction, resulting in a high frequency of metal motion. This process enabled a

uniformly dispersed high entropy alloy. In addition, this method has the advantages of low-cost, simple preparation, green and high productivity.

3.4 Morphonology and composition analysis results

3.4.1 Morphonology characterization results

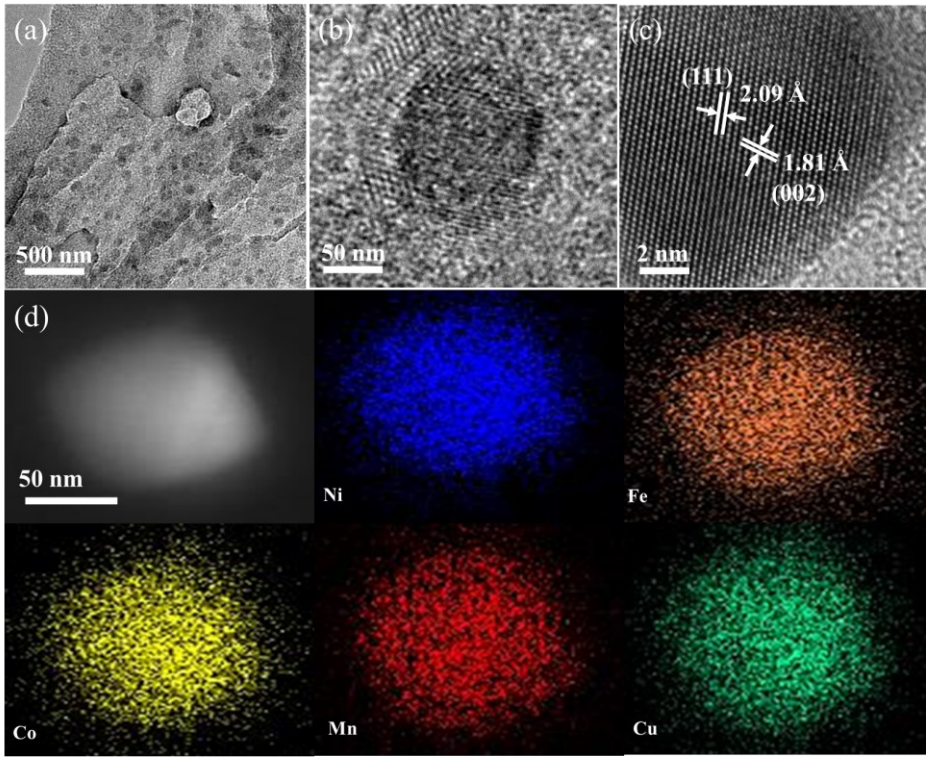

Figure 3.2. (b and c) TEM images of NiFeCoMnCu HEAs. (d) HRTEM image of NiFeCoMnCu HEAs. (e) Element mapping of Ni, Fe, Co, Mn, and Cu image of NiFeCoMnCu HEAs.

Transmission electron microscopy (TEM) image shown in (Figure 3.2a) indicated the prepared NiFeCoMnCu HEAs (dark particles) uniformly dispersed on the surface of carbon substrate without aggregation, suggesting that the effective chelating effect of CA played an important role to avoid aggregation. The TEM image with higher magnification (Figure 3.2b) revealed that the prepared NiFeCoMnCu HEAs possessed a diameter of about 80 nm. In addition,

a high-resolution transmission electron microscope (HRTEM) image (Figure 3.2c) showed a clear and ordered crystal interface, suggesting a high crystallinity of prepared NiFeCoMnCu HEAs. Moreover, the distinct lattice fringes with specific distances of 2.09 Å and 1.81 Å were corresponding to the (111) and (002) interfaces respectively.[19-24] To further confirm the metals were assembled to form a single phase, the element mapping measurement was carried out to explore the element distribution. As shown in Figure 3.2d, five metal elements of Ni, Fe, Co, Mn, and Cu were simultaneously dispersed over the whole particle, suggesting the formation of high entropy alloys without apparent elemental segregation.

3.4.2 Composition analysis results

The element mapping test confirmed that the five metal elements of Ni, Fe, Co, Mn and Cu were successfully chelated together and formed a particle with diameter of 80 nm. To further confirm the specific ration of these five metal species, the inductively coupled plasma-optical emission (ICP-OES) measurement was carried out to find the ratio of Ni, Fe, Co, Mn and Cu. As shown in the Figure 3.3, ICP-OES result exhibited the ratio of five metal elements with Ni : Fe : Co : Mn : Cu = 1 : 0.97 : 0.99 : 1.028 : 0.98.

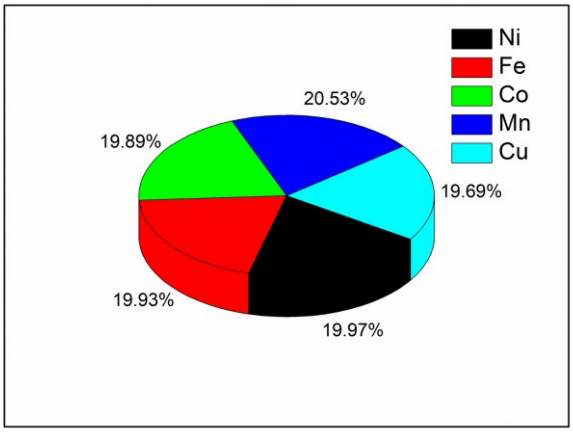

Figure 3.3. ICP-OES result of the prepared NiCoFeMnCu HEAs.

X-ray diffraction (XRD) pattern of the prepared NiFeCoMnCu HEAs (Figure 3.4a) exhibited a single-phase face-centered-cubic (fcc) structure without any metal phase separation, in which the XRD peaks located at 42.9°, 50.2° and 74.6° were attributed to the (111), (002) and (022) lattice planes respectively[25-26]. This single-phase structure could be formed by lowering the relevant free energy under high temperature when the mixed configuration entropy increased according to the increased number of elements accordingly. Moreover, the XRD patterns of unary Ni, binary NiFe, ternary NiFeCo, and quaternary NiFeCoMn were also explored. As shown in Figure 3.4b, all the samples exhibited a pure single-phase, which indicated the Fe, Co, Mn, and Cu were replacing the Ni atoms gradually and formed a single-phase without any impurity. This result demonstrated that the NiFeCoMnCu HEAs were prepared successfully.

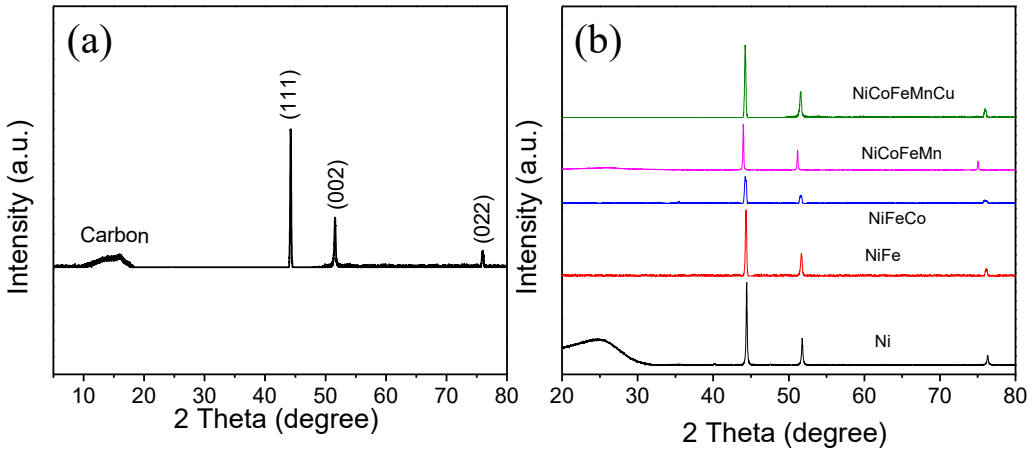

Figure 3.4. (a) XRD pattern of NiFeCoMnCu HEAs. (b) XRD patterns of unary Ni, binary NiFe, ternary NiFeCo, and quaternary NiFeCoMn as well as NiFeCoMnCu HEAs.

The high-entropy effect is a unique and qualitative concept of high entropy alloys raised from the increasing near-equimolar elemental components number. Therefore, the synergy effect of mixed elements in HEAs resulted in a unique charge distribution, which could accelerate the catalytic process. Accordingly, the X-ray photoelectron spectroscopy (XPS) was performed to

compare NiFeCoMnCu HEAs with unary Ni, binary NiFe, ternary NiFeCo, and quaternary NiFeCoMn. As shown in Figure 3.5a, the Ni $2p_{3/2}$ peaks of NiFeCoMnCu HEAs shifted to lower binding energy compared with that of unary Ni. The same phenomenon could also be found in the Ni 2p XPS spectrums of binary NiFe, ternary NiFeCo, and quaternary NiFeCoMn, which indicated an electron-rich state of Ni in the alloy. On the contrary, the Fe $2p_{3/2}$ peaks NiFeCoMnCu HEAs shifted to higher binding energy compared with that of binary NiFe, which suggested the electron-deficient state of Fe in NiFeCoMnCu HEAs (Figure 3.5b). Compared with the Fe $2p_{3/2}$ XPS spectrum of binary NiFe, the binding energy of Fe $2p_{3/2}$ remained unchanged when further increased the element number to ternary NiFeCo.[27-28] However, a large decreased binding energy of Fe $2p_{3/2}$ could be found in the Fe 2p XPS spectrum of quaternary NiFeCoMn, which indicated the Mn could be recognized as an electron donor. Moreover, comparing the lower Fe $2p_{3/2}$ binding energy in NiFeCoMnCu HEAs with the higher Fe $2p_{3/2}$ binding energy in quaternary NiFeCoMn, the element Cu could be recognized as an electron accepter. The effects of electron donor Mn and electron accepter Cu were also observed in Co 2p XPS spectrums of quaternary NiFeCoMn and NiFeCoMnCu HEAs, in which the Co $2p_{3/2}$ peaks shifted to low binding energy and high binding energy compared with that of ternary NiFeCo (Figure 3.5c). This result also indicated the electron-deficient state of Co in NiFeCoMnCu HEAs. The Mn $2p_{3/2}$ XPS peak in NiFeCoMnCu HEAs shifted to higher binding energy compared to that of quaternary NiFeCoMn, also indicating the electron-deficient state of Mn in HEAs (Figure 3d). The Cu 2p XPS spectrum of NiFeCoMnCu HEAs were also shown in Figure 3e. The Cu $2p_{3/2}$ peak was located at 932.3 eV with a satellite peak located at 940.4 eV, while the Cu $2p_{1/2}$ peak was located at 952.3 eV with a satellite peak located at 960.1 eV (Figure 3.5e). The XPS results demonstrated the existence of a strong multi-

metallic effect in NiFeCoMnCu HEAs, in which the Ni suffered a more negative charge while Fe, Co suffered a more negative charge.

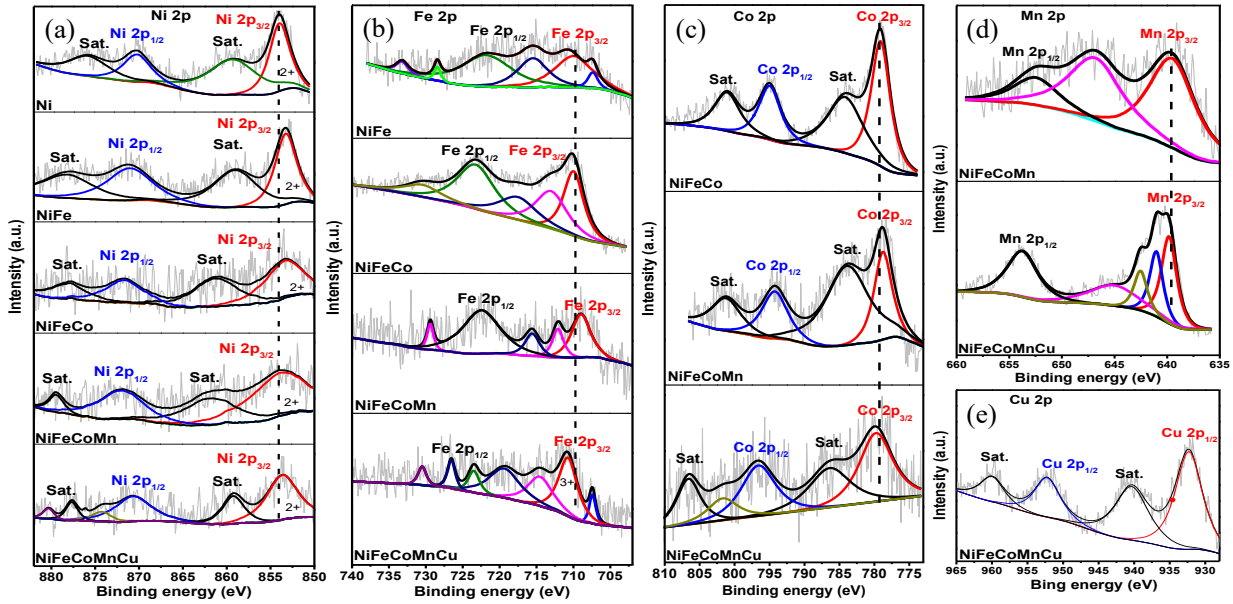

Figure 3.5 (a) Ni2p XPS spectrums of unary Ni, binary NiFe, ternary NiFeCo, quaternary NiFeCoMn, and quinary NiFeCoMnCu HEAs. (b) Fe 2p XPS spectrums of binary NiFe, ternary NiFeCo, quaternary NiFeCoMn, and quinary NiFeCoMnCu HEAs. (c) Co2p XPS spectrums of ternary NiFeCo, quaternary NiFeCoMn, and quinary NiFeCoMnCu HEAs. (d) Mn2p XPS spectrums of quaternary NiFeCoMn and quinary NiFeCoMnCu HEAs. (e) Cu2p XPS spectrums of NiFeCoMnCu HEAs.

3.5 Electrochemical measurements results

3.5.1 OER performance

The linear sweep voltammetry curves (LSV) were performed to evaluate the OER activity of prepared unary Ni, binary NiFe, ternary NiFeCo, quaternary NiFeCoMn, and quinary NiFeCoMnCu HEAs in 1.0 M KOH by a typical three-electrode system with carbon as counter

electrode and Ag/AgCl as a reference electrode. The OER activity of commercial RuO_2 electrocatalyst was also invested as the compassion by the same method. All the mentioned potentials had been converted to the values versus reversible hydrogen electrode (RHE).

As shown in Figure 3.6a, the NiFeCoMnCu HEAs exhibited the best OER activity with an overpotential of 240 mV at 10 mA cm^{-2}, which was even superior to that of a commercial RuO_2 electrocatalyst (322 mV). Moreover, the overpotentials at 10 mA cm^{-2} decreased consecutively from 394 mV to 385 mV, 376 mV, and 288 mV with the succession of increasing metal species of unary Ni, binary NiFe, ternary NiFeCo, and quaternary NiFeCoMn, respectively. This phenomenon of the enhanced OER activity arising from the number increase of metal species indicated that the mixing entropy and electronic structure tailored by various metal kinds played an important role to improve the electrocatalytic activity. Tafel slope could be recognized as a vital intrinsic factor to evaluate the OER performance. The NiFeCoMnCu HEAs exhibited the best electrocatalytic activity and favorable OER kinetics with a low Tafel slope of 71.2 mV dec^{-1}, while a relatively high Tafel slope of 252.8 mV dec^{-1}, 137.3 mV dec^{-1}, 134.4 mV $dec^{-1,}$ and 104.4 mV dec^{-1} for unary Ni, binary NiFe, ternary NiFeCo and quaternary NiFeCoMn, respectively shown in Figure 3.6b. This result also confirmed that the mixing of high entropy in NiFeCoMnCu HEAs enabled fast and favorable reaction kinetics, thus resulting in an outstanding OER activity. Moreover, this excellent OER activity of NiFeCoMnCu was much superior to that of the reported electrocatalysts (Figure 3.6c and Table S3.2).

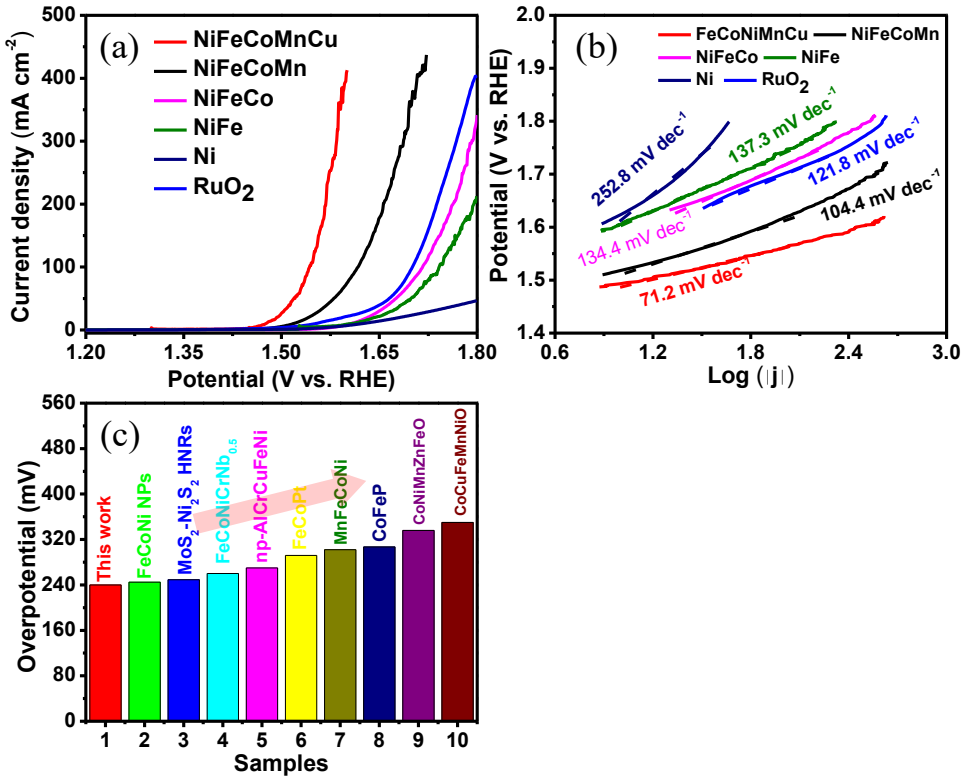

Figure 3.6. (a) OER LSV curves of unary Ni, binary NiFe, ternary NiFeCo, quaternary NiFeCoMn, quinary NiFeCoMnCu HEAs and compared RuO_2. (b) Tafel slope of unary Ni, binary NiFe, ternary NiFeCo, quaternary NiFeCoMn, quinary NiFeCoMnCu HEAs and compared RuO_2. (c) The OER overpotential at 10 mA cm^{-2} for reported electrocatalysts.

Table S3.2. OER performance of compared reported electrocatalysts

Catalysts	Overpotential (mA cm^{-2})	Electrolyte	Reference
This work	240	1.0 M KOH	
MoS_2-Ni_3S_2 HNRs	249	1.0 M KOH	*ACS Catalysis., 2017, 7, 2357–2366*

MnFeCoNi	302	1.0 M KOH	*J. Power Sources., 2019, 430,104–111*
AlNiCoRuMo	245	1.0 M KOH	*ACS Mater. Lett., 2020, 2, 1698-1706.*
Ni-Mo-S/Ni-foam	306	1.0 M KOH	*ECS Transactions., 2020, 97 ,575*
CoFeP	307	1.0 M KOH	*J. Electro. 491 Soc., 2018, 165, H271.*
np-AlCrCuFeNi	270	1.0 M KOH	*Rare Metals, 2022, 41, 125-131.*
CoNiMnZnFeO	335	1.0 M KOH	*J Alloys Compd., 2021, 868, 159064.*
CoCuFeMnNiO	350	1.0 M KOH	*J Mater Chem. A, 2019, 7, 24211-24216.*
FeCoPt	292	1.0 M KOH	*Materials Science and Engineering. IOP Publishing, 2019, 592,1,012043.*

3.5.2 Electrochemical characterizations and mechanism study

To fully understand the reason why the OER performance was promoted, the electrochemical active surface area (ECSA) and electrochemical impedance spectroscopy (EIS) were also measured. The double-layer capacitance (C_{dl}) between electrolyte and electrocatalyst could be measured through cyclic voltammetry (Figure 3.7), which could be used for calculating the value of ECSA. As shown in Figure 3.8a, the NiFeCoMnCu HEAs possessed the highest C_{dl} value of 18.12 mF cm^{-2}, while 4.73 mF cm^{-2}, 5.45 mF cm^{-2}, 8.03 mF $cm^{-2,}$ and 16.45 mF cm^{-2} for unary Ni, binary NiFe, ternary NiFeCo and quaternary NiFeCoMn respectively. Compared with the C_{dl} value of unary Ni, almost four times improvement of C_{dl} value for NiFeCoMnCu HEAs indicated that the more favorable reaction intermediates adsorption could be realized by the tuned multiple elements species according to the Sabatier principle, thus resulting in more exposed active sites and superior OER activity (Figure 3.6a). Likewise, the NiFeCoMnCu HEAs exhibited the lowest electron transfer resistance among the compared unary Ni, binary NiFe, ternary NiFeCo, and quaternary NiFeCoMn (Figure 3.8b), suggesting the high conductivity and rapid catalytic kinetics of NiFeCoMnCu HEAs, which also revealed the reason of the lowest Tafel slope for NiFeCoMnCu HEAs (Figure 3.6b).

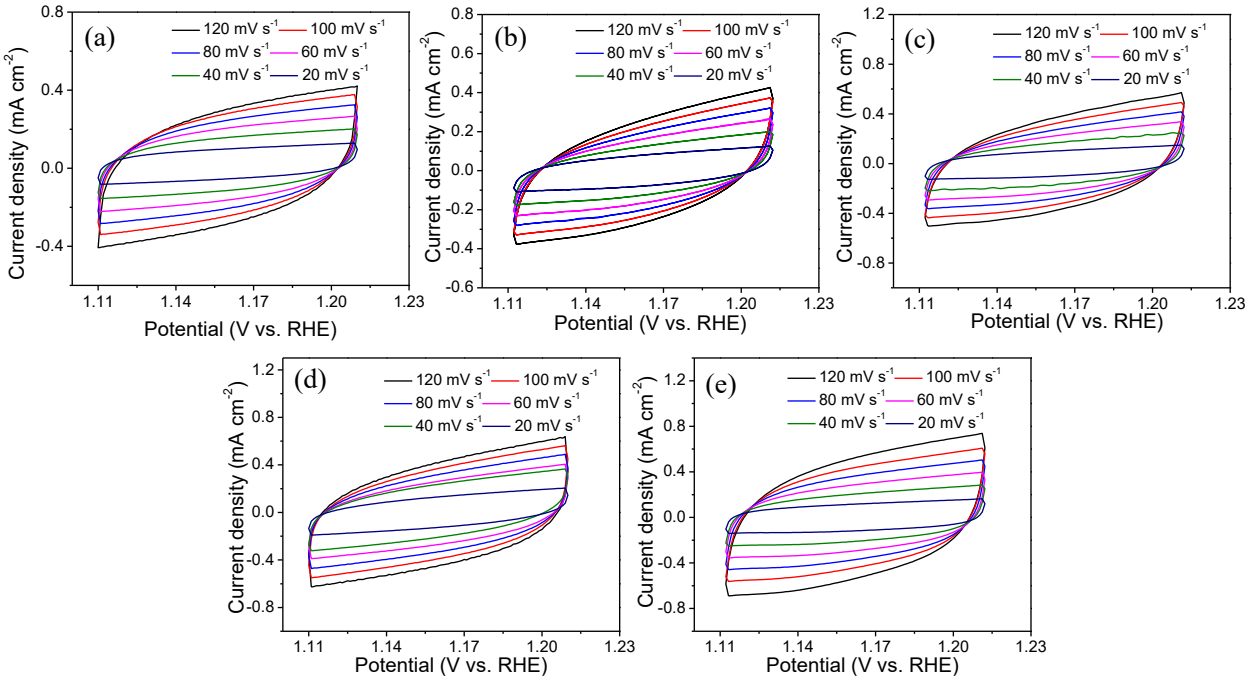

Figure 3.7. CV measurements for ECSA. (a) unary Ni, (b) binary NiFe, (c) ternary NiFeCo (d) quaternary NiFeCoMn and (e) quinary NiFeCoMnCu HEAs.

Therefore, this excellent OER activity could be attributed to the unique high entropy property raised from the synergy effect of mixed elements in NiFeCoMnCu HEAs, which specifically could be due to the following two reasons: a) the multimetallic species are amenable to forming an optimized structure, which could accelerate the adsorption/desorption of intermediates during the reaction process, thus resulted in more exposed active sites and superior electrocatalytic activity; b) the unfilled d-orbitals of various metals could lead to taking/lending charges from the surface to the adsorbed intermediates, which provided a low energy barrier to the process of electron distribution, thus resulted in favorable electrocatalytic kinetics.

Moreover, the OER process enabled by NiFeCoMnCu HEAs exhibited extreme stability, which both current density and potential remained unchanged during 10 hours of continuous current density at 1.5 V and potential at 10 mA cm^{-2} measurements (Figure 3.8c). In addition, the

current density displayed a steady change for every potential change from 1.5 V to 1.54 V (insert of Figure 3.8c), which also indicated an outstanding conductivity and transport property of the NiFeCoMnCu HEAs electrocatalyst.

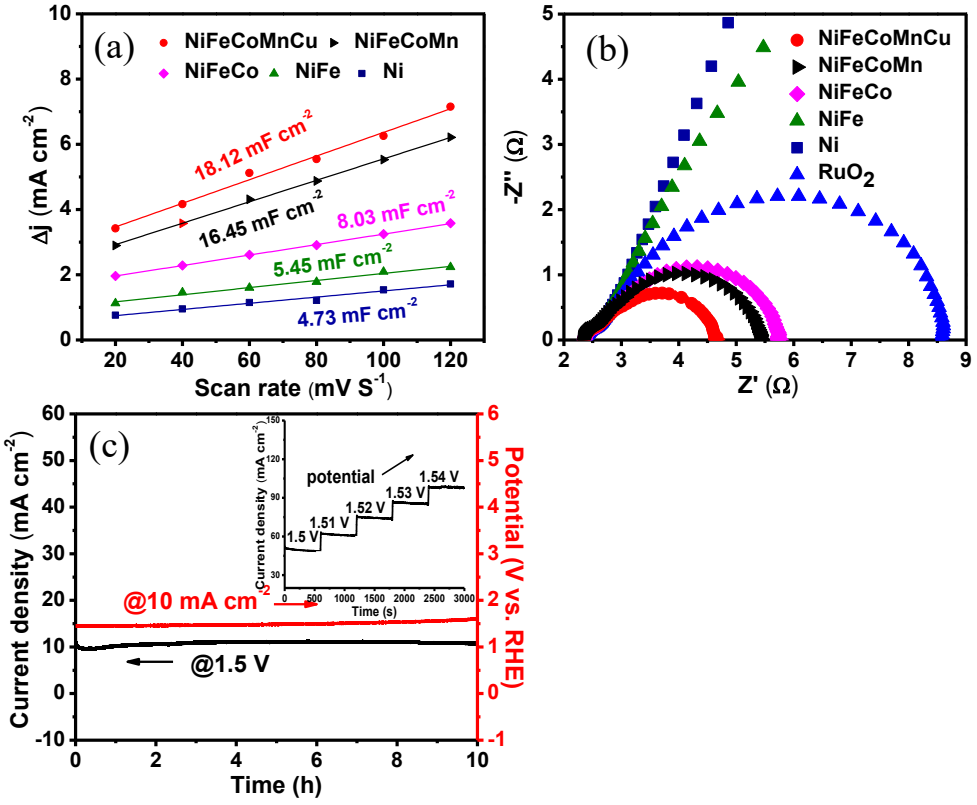

Figure 3.8. (a) ECSA for unary Ni, binary NiFe, ternary NiFeCo, quaternary NiFeCoMn, and quinary NiFeCoMnCu HEAs. (b) EIS of unary Ni, binary NiFe, ternary NiFeCo, quaternary NiFeCoMn, and quinary NiFeCoMnCu HEAs. (c) Current density (black line) and potential (red line) stability measurement for 10 h of NiFeCoMnCu HEAs. Insert: multistep-voltage cure of NiFeCoMnCu HEAs.

3.6 Alkalic HER performance

The electrocatalytic HER activities of unary Ni, binary NiFe, ternary NiFeCo, quaternary NiFeCoMn, and quinary NiFeCoMnCu HEAs were also evaluated in 1.0 M KOH. Similar to the result of OER performance, the HER activity was improved with the sequence of increasing metal species number, in which specifically the overpotential at 10 mA cm^{-2} decreased from 395 mV for unary Ni to 330 mV, 293 mV, 221 mV, and 165 mV for binary NiFe, ternary NiFeCo, quaternary NiFeCoMn and quinary NiFeCoMnCu HEAs, respectively (Figure 3.9a). Moreover, as the commercial electrocatalyst, the overpotential at 10 mA cm^{-2} for Pt/C was only 83 mV lower than that of NiFeCoMnCu HEAs, indicating a promised prospect for large-scale usage of NiFeCoMnCu HEAs electrocatalyst. The above-listed results directly demonstrated that the incorporation of quinary metal species effectively promoted the HER activity. Furthermore, the Tafel slope of NiFeCoMnCu HEAs was 61.6 mV dec^{-1} (Figure 3.9b), which was much lower than that of unary Ni (167.4 mV dec^{-1}), binary NiFe (137.4 mV dec^{-1}), ternary NiFeCo (135 mV dec^{-1}) and quaternary NiFeCoMn (71.4 mV dec^{-1}). Although the mechanism of HER process in alkaline solution remains unclear, the following reactions with multisite step process could be concerned:[29-30]

$M + H_2O + e^- \rightarrow MH_{ads} + Oe^-$ (discharge reaction; Volmer step) (1)

$MH_{ads} + MH_{ads} \rightarrow 2M + H_2$ (recombination reaction; Tafel step) (2)

$MH_{ads} + H_2O + e^- \rightarrow M + OH^- + H_2$ (Heyrovsky step) (3)

The “M” indicated the H adsorption active sites. Based on the result of the Tafel slope decreasing at the sequence of increasing the number of metal species, the NiFeCoMnCu HEAs confirmed that the internal synergy effect of mixed metal elements promoted the HER kinetics according to the Volmer-Heyrovsky mechanism, thus resulting in the promoted HER activity.

Moreover, this excellent HER activity of NiFeCoMnCu HEAs was superior to that of reported similar electrocatalysts (Figure 3.9c and Table 3.3).

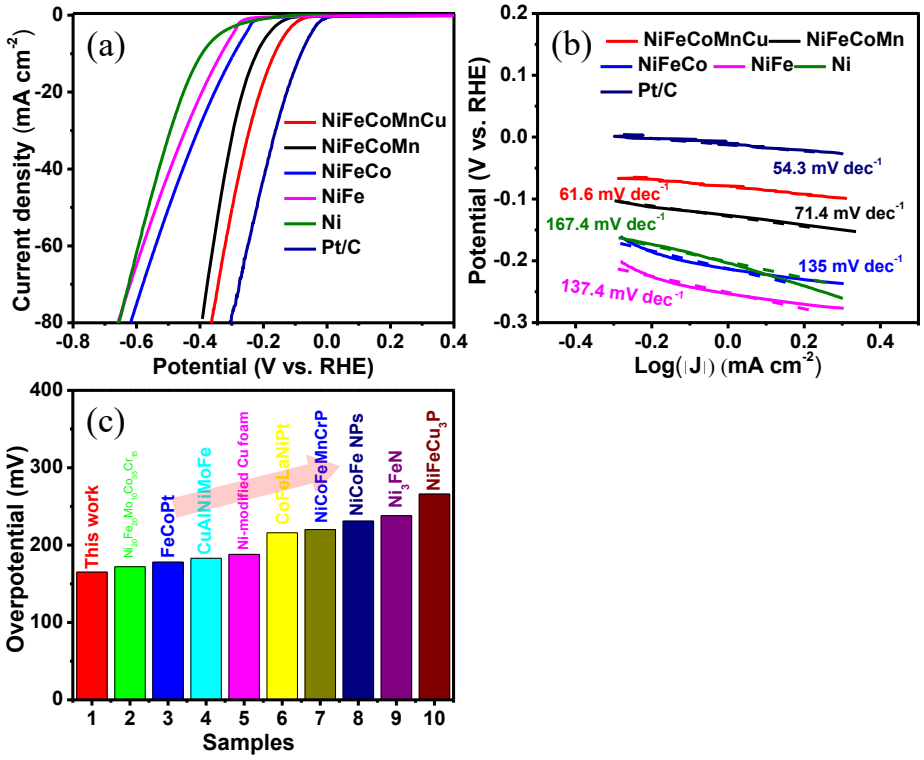

Figure 3.9. (a) HER LSV curves of unary Ni, binary NiFe, ternary NiFeCo, quaternary NiFeCoMn, quinary NiFeCoMnCu HEAs and compared Pt/C. (b) Tafel slope of unary Ni, binary NiFe, ternary NiFeCo, quaternary NiFeCoMn, quinary NiFeCoMnCu HEAs and compared Pt/C. (c) The HER overpotential at 10 mA cm^{-2} for reported electrocatalysts.

Table 3.3. HER performance of compared reported electrocatalysts

Catalysts	Overpotential (mA cm^{-2})	Electrolyte	Reference
This work	165	1.0 M KOH	

N-modified Cu foam	188	1.0 M KOH	*Inter. J. Hydro. Ener. 2020, 45, 2808–2817*
NiFe-LDH /Cu_3P	266	1.0 M KOH	*Adv. Funct. Mater. 2015, 25, 7337–7347*
Ni_3FeN	238	1.0 M KOH	*Inorg. Chem. Fron.,. 2016, 3, 630–634*
MoS_2-VN	179	1.0 M KOH	*ACS Appl. Ener. Mater., 2019,2, 2854–2861.*
NiCoFeMnCrP	220	1.0 M KOH	*J Mater Chem. A, 2021, 9, 17913-17922*
NiCoFe NPs	231	1.0 M KOH	*Nanoscale., 2018, 10, 12975–12980.*
CuAlNiMoFe	183	1.0 M KOH	*Adv. Funct. Mater., 2021, 31, 2009613*
$Ni_{20}Fe_{20}Mo_{10}Co_{35}Cr_{15}$	172	1.0 M KOH	*Electrochimica Acta 2018, 279, 19e2320*
FeCoPt	178	1.0 M KOH	*Materials Science and Engineering. IOP Publishing, 2019, 592,1,012043.*

3.7 Conclusions

In summary, an fcc single-phase NiFeCoMnCu HEAs with a diameter of ~ 80 nm was prepared by combining a facile citric acid chelating method with pyrolysis process. Owing to the efficient chelation effect of citric acid, the NiFeCoMnCu HEAs uniformly dispersed on the surface of the carbon substrate without aggregation. The binding energy shift of metal elements in NiFeCoMnCu HEAs and increased ECSA and conductivity from unary Ni to quinary NiFeCoMnCu HEAs demonstrated the strong synergy effect between metal species and fast charge transfer in high entropy alloys. This high-entropy effect in NiFeCoMnCu HEAs resulted in promoted OER and HER activity of 240 mV and 165 mV at 10 mA cm^{-2} in 1.0 M KOH.

Our innovative solution: Herein, citric acid (CA) was selected to chelated halide salts to form homogeneous polymetallic networks through hydrogen-bond, which efficiently avoided the aggregation of metal species. A fcc single-phase NiFeCoMnCu HEAs was prepared successfully prepared. Benefiting from the unique synergy effect in NiFeCoMnCu HEAs, the NiFeCoMnCu HEAs exhibited excellent OER and HER activity in 1.0 M KOH.

Outcomes of our work and interest to others in the field:

1. The prepared NiFeCoMnCu HEAs dipsersed uniformly without any aggregation on the surafce of carbon substrate with diameter of 80 nm. The NiFeCoMnCu HEAs exhibited outstanding oxygen evolution reaction (OER) and hydrogen evolution reaction (HER) activity with overpotential of 240 mV and 165 mV at 10 mA cm^{-2} in 1.0 M KOH respectively, which were much lower than that of reported similar electrocatalysts.
2. The shift of binding energy for metal elements in NiFeCoMnCu HEAs demonstrated the existence of a strong multi-metallic effect in NiFeCoMnCu HEAs, in which the Ni suffered

more positive charge while Fe, Co suffered more negative charge. The increased ECSA and conductivity from unary Ni to quinary NiFeCoMnCu HEAs further confirmed the strong synergy effect between metal species and fast charge transfer in high entropy alloy, which was also the reason of the promoted electrocatalytic activity.

This CA chelating method presented in this work provides ideas for preparing other various HEAs electrocatalysts and promising potentials in many important applications, such as CO_2 reduction reaction, nitrogen reduction reaction, and oxygen reduction reaction.

References

1. Yu, L.; Zhu, Q.; Song, S.; McElhenny, B.; Wang, D.; Wu, C.; Qin, Z.; Bao, J.; Yu, Y.; Chen, S.; Ren, Z., Non-noble Metal-nitride based Electrocatalysts for High-performance Alkaline Seawater Electrolysis. *Nat Commun* **2019,** *10* (1), 5106.

2. Niu, B.; Zhang, F.; Ping, H.; Li, N.; Zhou, J.; Lei, L.; Xie, J.; Zhang, J.; Wang, W.; Fu, Z., Sol-gel Autocombustion Synthesis of Nanocrystalline High-entropy Alloys. *Sci Rep* **2017,** *7* (1), 3421.

3. Alobaid, A.; Wang, C.; Adomaitis, R. A., Mechanism and Kinetics of HER and OER on NiFe LDH Films in an Alkaline Electrolyte. *Journal of The Electrochemical Society* **2018,** *165* (15), J3395-J3404.

4. Ye, Y. F.; Wang, Q.; Lu, J.; Liu, C. T.; Yang, Y., High-entropy Alloy: Challenges and Prospects. *Materials Today* **2016,** *19* (6), 349-362.

5. Gao, S.; Hao, S.; Huang, Z.; Yuan, Y.; Han, S.; Lei, L.; Zhang, X.; Shahbazian-Yassar, R.; Lu, J., Synthesis of High-entropy Alloy Nanoparticles on Supports by the Fast Moving Bed Pyrolysis. *Nat Commun* **2020,** *11* (1), 2016.

6. Hou, J.; Wang, Z.; Shi, X.; Wang, Z.; Qiao, J.; Wu, Y., Strengthening of an $Al_{0.45}CoCrFeNi$ high-entropy Alloy via in situ Fabricated Duplex-structured Composites. *Journal of Materials Science* **2020,** *55* (18), 7894-7909.

7. Tang, J.; Xu, J. L.; Ye, Z. G.; Li, X. B.; Luo, J. M., Microwave Sintered Porous CoCrFeNiMo High Entropy Alloy as an Efficient Electrocatalyst for Alkaline Oxygen Evolution Reaction. *Journal of Materials Science & Technology* **2021,** *79*, 171-177.

8. Zhou, P.; Liu, D.; Chen, Y.; Chen, M.; Liu, Y.; Chen, S.; Kwok, C. T.; Tang, Y.; Wang, S.; Pan, H., Corrosion Engineering Boosting Bulk $Fe_{50}Mn_{30}Co_{10}Cr_{10}$ High-entropy Alloy as High-efficient Alkaline Oxygen Evolution Reaction Electrocatalyst. *Journal of Materials Science & Technology* **2022,** *109*, 267-275.

9. Dai, W.; Lu, T.; Pan, Y., Novel and Promising Electrocatalyst for Oxygen Evolution Reaction based on MnFeCoNi High Entropy Alloy. *Journal of Power Sources* **2019,** *430*, 104-111.

10. Bondesgaard, M.; Becker, J.; Xavier, J.; Hellstern, H.; Mamakhel, A.; Iversen, B. B., Guide to By-products Gormed in Organic Solvents under Solvothermal Conditions. *The Journal of Supercritical Fluids* **2016,** *113*, 166-197.

11. He, F.; Wang, Z.; Cheng, P.; Wang, Q.; Li, J.; Dang, Y.; Wang, J.; Liu, C. T., Designing Eutectic High Entropy Alloys of $CoCrFeNiNb_x$. *Journal of Alloys and Compounds* **2016,** *656*, 284-289.

12. Zlotea, C.; Sow, M. A.; Ek, G.; Couzinié, J. P.; Perrière, L.; Guillot, I.; Bourgon, J.; Møller, K. T.; Jensen, T. R.; Akiba, E.; Sahlberg, M., Hydrogen Sorption in TiZrNbHfTa High Entropy alloy. *Journal of Alloys and Compounds* **2019,** *775*, 667-674.

13. El Sawy, E. N.; Handal, H. T.; Thangadurai, V.; Birss, V. I., Pt_xIr_y Alloy Nanoparticles with fully Tunable Bulk and Surface Compositions. *Journal of Materials Chemistry A* **2016,** *4* (40), 15400-15410.

14. Sivanantham, A.; Lee, H.; Hwang, S. W.; Ahn, B.; Cho, I. S., Preparation, Electrical and Electrochemical Characterizations of CuCoNiFeMn high-entropy-alloy for overall Water splitting at Neutral-pH. *Journal of Materials Chemistry A* **2021,** *9* (31), 16841-16851.

15. Tomboc, G. M.; Kwon, T.; Joo, J.; Lee, K., High Entropy Alloy Electrocatalysts: A Critical Assessment of Fabrication and Performance. *Journal of Materials Chemistry A* **2020,** *8* (30), 14844-14862.

16. Zhao, X.; Xue, Z.; Chen, W.; Bai, X.; Shi, R.; Mu, T., Ambient Fast, Large-scale Synthesis of Entropy-stabilized Metal–organic Framework Nanosheets for Electrocatalytic Oxygen Evolution. *Journal of Materials Chemistry A* **2019,** *7* (46), 26238-26242.

17. Fu, M.; Ma, X.; Zhao, K.; Li, X.; Su, D., High-entropy Materials for Energy-related Applications. *iScience* **2021,** *24* (3), 102177.

18. Wu, D.; Kusada, K.; Yamamoto, T.; Toriyama, T.; Matsumura, S.; Kawaguchi, S.; Kubota, Y.; Kitagawa, H., Platinum-Group-Metal High-Entropy-Alloy Nanoparticles. *J Am Chem Soc* **2020,** *142* (32), 13833-13838.

19. Ma, Y.; Ma, Y.; Wang, Q.; Schweidler, S.; Botros, M.; Fu, T.; Hahn, H.; Brezesinski, T.; Breitung, B., High-entropy Energy Materials: Challenges and New Opportunities. *Energy & Environmental Science* **2021,** *14* (5), 2883-2905.

20. Wang, J.; Li, J.; Wang, J.; Bu, F.; Kou, H.; Li, C.; Zhang, P.; Beaugnon, E., Effect of Solidification on Microstructure and Properties of $FeCoNi(AlSi)_{0.2}$ High-Entropy Alloy Under Strong Static Magnetic Field. *Entropy (Basel)* **2018,** *20* (4).

21. Ipadeola, A. K.; Lebechi, A. K.; Gaolatlhe, L.; Haruna, A. B.; Chitt, M.; Eid, K.; Abdullah, A. M.; Ozoemena, K. I., Porous High-entropy Alloys as Efficient Electrocatalysts for Water-splitting Reactions. *Electrochemistry Communications* **2022,** *136*, 107207.

22. Zhang, G.; Ming, K.; Kang, J.; Huang, Q.; Zhang, Z.; Zheng, X.; Bi, X., High Entropy Alloy as a Highly Active and Stable Electrocatalyst for Hydrogen Evolution Reaction. *Electrochimica Acta* **2018,** *279*, 19-23.

23. Zhu, Q.; Qu, Y.; Liu, D.; Ng, K. W.; Pan, H., Two-Dimensional Layered Materials: High-Efficient Electrocatalysts for Hydrogen Evolution Reaction. *ACS Applied Nano Materials* **2020,** *3* (7), 6270-6296.

24. Yan, Y.; Xia, B.; Xu, Z.; Wang, X., Recent Development of Molybdenum Sulfides as Advanced Electrocatalysts for Hydrogen Evolution Reaction. *ACS Catalysis* **2014,** *4* (6), 1693-1705.

25. Liu, J.; Liu, X.; Shi, H.; Luo, J.; Wang, L.; Liang, J.; Li, S.; Yang, L.-M.; Wang, T.; Huang, Y.; Li, Q., Breaking The Scaling Relations of Oxygen Evolution Reaction on Amorphous NiFeP Nanostructures with Enhanced Activity for overall Seawater splitting. *Applied Catalysis B: Environmental* **2022,** *302*, 120862.

26. Zheng, J., Seawater splitting for High-efficiency Hydrogen Evolution by Alloyed $PtNi_x$ Electrocatalysts. *Applied Surface Science* **2017,** *413*, 360-365.

27. Zhang, Y.; Li, P.; Yang, X.; Fa, W.; Ge, S., High-efficiency and Stable Alloyed Nickel based Electrodes for Hydrogen Evolution by Seawater splitting. *Journal of Alloys and Compounds* **2018,** *732*, 248-256.

28. Gayen, P.; Saha, S.; Ramani, V., Selective Seawater Splitting Using Pyrochlore Electrocatalyst. *ACS Applied Energy Materials* **2020,** *3* (4), 3978-3983.

29. Lv, Q.; Han, J.; Tan, X.; Wang, W.; Cao, L.; Dong, B., Featherlike NiCoP Holey Nanoarrys for Efficient and Stable Seawater Splitting. *ACS Applied Energy Materials* **2019,** *2* (5), 3910-3917.

30. Jin, H.; Liu, X.; Vasileff, A.; Jiao, Y.; Zhao, Y.; Zheng, Y.; Qiao, S. Z., Single-Crystal Nitrogen-Rich Two-Dimensional Mo_5N_6 Nanosheets for Efficient and Stable Seawater Splitting. *ACS Nano* **2018,** *12* (12), 12761-12769.

Chapter 4. Bifunctional NiFeCoMnCu HEAs for electrochemical alkaline seawater splitting

4.1 Introduction

Hydrogen evolution from the electrochemical water-splitting reaction recently has been widely recognized as promised future approach to retard the change of climate and pressed energy source on the earth, which could generate enough amount of hydrogen or hydrogen chemical bond for energy consume by converting electric energy into chemical energy.[1-3] In addition, besides the application of energy source, hydrogen could also be recognized as the sustainable intermediate or primary energy vector, which could be electrochemically converted into other materials with chemical hydrogen bond or ingredient for fuels, like methanol, ethanol, and some hydrocarbons with higher molecular weight.[4-6] Many previous studies and research have been focused on developing different technologies to further increase the activity of electrocatalysts and decrease their costs, which aimed to promote the electrochemical production of hydrogen.[8-11] Among the previous studies, various electrolysis for electrochemical water-splitting were developed, such as the exchange membrane electrolysis, proton exchange membrane electrolysis, and anion exchange membrane electrolysis.[8-9, 12-13] However, though different electrolysis owned different properties, the same reaction occurred in this electrolysis, which was the hydrogen evolution reaction (HER) at the cathode and oxygen evolution reaction (OER) at the anode.[7, 14-16]

Besides the electrolysis, the water feeds with high purity also plays important role for the electrochemical water-splitting reaction, which is received less attention.[17-19] Different with the prefect water feeds in the laboratory, the arid region lacks the highly pure water feeds, which makes it difficult to deploy electrochemical water-splitting device. The high temperature and arid climate limit the access to the highly pure water feeds, while the ocean seawater is easily available.

In fact, almost 96.5 % of water storage on the earth is stored in the oceans, thus the seawater could be recognized as unlimited water feeds source. The pH and salt concentration of seawater are different in different areas, but the average of pH and salt concentration were about 8 and 3.5 wt%.[199] The ions in seawater usually have enough concentration to react under the applied voltage. Specifically, the chloride and bromide with responding oxidation-reduction potential could compete with the electrochemical water-splitting reaction, such as the oxidation reaction of the chloride and bromide. More importantly, the ions of Cl^- and Na^+ are the most ions in seawater, in which the concentration is about 0.5 M.[20]

The chlorine evolution reaction (CER), which occurs at the anode during electrochemical seawater-splitting reaction because of the about 0.5 M Cl^- in seawater, could be recognized as the main challenge for the electrochemical seawater-splitting technology. The hypochlorite formation will be formed from the reaction of OH^- and Cl^-, which occurs at the anode for the CER in alkaline solution. However, the onset potential of the above reaction is 490 mV, which is much higher than the onset potential of OER.[16, 19, 21] Therefore, the effective OER electrocatalysts should possess a low onset potential, which is must lower than 490 mV. In addition, some indissoluble materials will be formed such as magnesium hydroxide at the cathode, which will deposit on the surface of electrode and corrode the electrode. These indissoluble materials could destroy the electrocatalysts and block the HER and OER for electrochemical seawater-splitting. According to the above problem, the highly effective electrocatalysts towards electrochemical seawater-splitting must possess the multifunctional active sites and large surface area. Up to now, few studies reported high effective electrocatalysts for the seawater-splitting reaction, because of these above intractable problems. Recent years, bimetal NiFe hydroxide layer electrocatalyst was reported for the seawater-splitting reaction in alkaline solution by Kuang et al. The NiFe hydroxide layer

electrocatalyst was covered by a layer of nickel sulfide, which could be recognized as the active sites. The nickel sulfide covered NiFe hydroxide layer electrocatalyst exhibited excellent electrocatalytic activity with high stability in 1.5 M NaCl + 6 M KOH electrolyte at 80 ºC.[22-23] Some non-noble cobalt based electrocatalysts such as cobalt selenides, cobalt phosphate, and transition metal hexacyanometallate were fully studied their OER activity in NaCl electrolytes. However, the above materials require large overpotential to reach high current density (500 mV for 1000 mA cm^{-2}), which is much higher than 490 mV and not possible for the electrochemical seawater-splitting reaction.[24-25] Therefore, it is highly demand to develop highly effective non-noble electrocatalyst for seawater-splitting reaction.[27]

Herein, the prepared NiFeCoMnCu high entropy alloys (NiFeCoMnCu HEAs) were used for the bifunctional water-splitting electrocatalyst. The OER and HER activity of NiFeCoMnCu HEAs in alkalic solution were fully studied in chapter 3. With the excellent OER and HER activity, NiFeCoMnCu HEAs enabled an effective electrochemical water-splitting process with a low 1.53 V to reach 10 mA cm^{-2}, which was much lower than that of Pt/C-RuO_2 electrocatalyst (1.65 V). In addition, by adding 0.5 M NaCl into 1.0 M KOH solution, we prepared the simulated seawater electrolyte and explored the water-splitting activity of NiFeCoMnCu HEAs in the simulated seawater electrolyte. Moreover, the natural seawater also was used for the electrolyte.[28-31] The bifunctional NiFeCoMnCu HEAs electrocatalyst also enabled a highly effective and stable seawater-splitting process with 10.5 mA cm^{-2} at 1.8 V for 10 h.

4.2 Material and characterization information

Table 4.1. Experiment materials

Materials	Purity	Company
$FeCl_3 \cdot 6H_2O$	99.9%	Wako
$NiCl_2 \cdot 6H_2O$	99.9%	Wako
$MnCl_2 \cdot 4H_2O$	99.9%	Wako
$CuCl_2 \cdot 2H_2O$	99.9%	Wako
Deionized water	18.6 MΩ	Homemade
$CoCl_2 \cdot 6H_2O$	99.9%	Wako
KOH	99.9%	Wako
NaCl	99.9 w%	Wako
Nafion	5 w% solution	Wako
$NH_3 \cdot H_2O$	25 w%	Wako
RuO_2	20 w%	Wako
Pt/C	20 w%	Wako
Citric acid	99.9 %	Wako

CH_3CH_2OH	99.9%	Wako
$CH_3CHOHCH_3$	99.9%	Wako
Seawater	Obtained at Wakita beach	

All the above-mentioned materials in Table S1 were purchased from the Wako. The regents and the relative solvent were directly used for the experiment without any change. The electrochemical measurements were carried out on the electrochemical workstation CHI760E.

4.3 Experiment process

4.3.1 Electrode Preparation information

The synthesis process of the bifunctional NiFeCoMnCu HEAs was displayed in the chapter 3 and all the NiFeCoMnCu HEAs electrocatalysts used in this chapter were the same materials with chapter 3.

Preparing the electrochemical seawater-splitting electrode. The carbon paper was washed in ethanol and water for several times under sonication and each wash process should sustain 30 min. After the last ethanol wash process, the cleaned carbon paper was dry at 60 ºC under vacuum overnight. 5 mg of NiFeCoMnCu HEAs was added into 500 μL ethanol and IPA aqueous solution, in which the volume ratio of ethanol, IPA, water and Nafion was 60 : 15 : 15 : 10. The total concentration of the electrocatalyst is 10 mg mL^{-1}. After sonicating at room temperature for 2 h, the well dispersed electrocatalyst ink with high stability was prepared. 30 μL of the NiFeCoMnCu HEAs ink was dropped slowly on the surface of carbon paper electrode and then the electrocatalyst ink dried under the infrared lamp. The area of the carbon paper electrode is 0.5 cm^{-2}, thus, the loading amount of the electrocatalyst is about 0.6 mg cm^{-2}.

4.3.2 Seawater-splitting electrolysis preparation information

Preparing alkaline simulated seawater electrolyte. The simulated seawater electrolyte was prepared by dissolving 0.5 M NaCl into 1.0 M KOH.

Preparing alkaline seawater electrolyte. The seawater was collected in the ocean. Before the electrochemical measurement, the seawater was stranded still for several hours. Then the supernatant seawater was filtered using filterable membrane for three times. Then the KOH was added into the clean seawater and the concentration is 1.0 M.

Electrochemical seawater-splitting process. The electrochemical seawater-splitting process was carried out by a two-electrode system. The carbon paper coating with the NiFeCoMnCu HEAs electrocatalyst was used as electrodes. The distance of these two electrodes was 2 cm. Under the applied voltage, the OER occurred at the anode, while the HER occurred at the cathode. The LSV scan rate was 50 mV s^{-1}.

4.4 Electrochemical seawater-splitting activity

With such outstanding OER and HER electrocatalytic activity (displayed in chapter 3), the NiFeCoMnCu HEAs as a bifunctional electrocatalyst could enable an overall electrochemical water-splitting reaction. As shown in Figure 4.1a, a two-electrode electrochemical water-splitting device was assembled, where the bifunctional NiFeCoMnCu HEAs electrocatalyst was used for anode and cathode. Under the eligible voltage, the bifunctional NiFeCoMnCu HEAs enabled favorable OER and HER process at anode and cathode respectively with numerous gas bubbles on the surface of the corresponding electrode, which was marked by red circles.

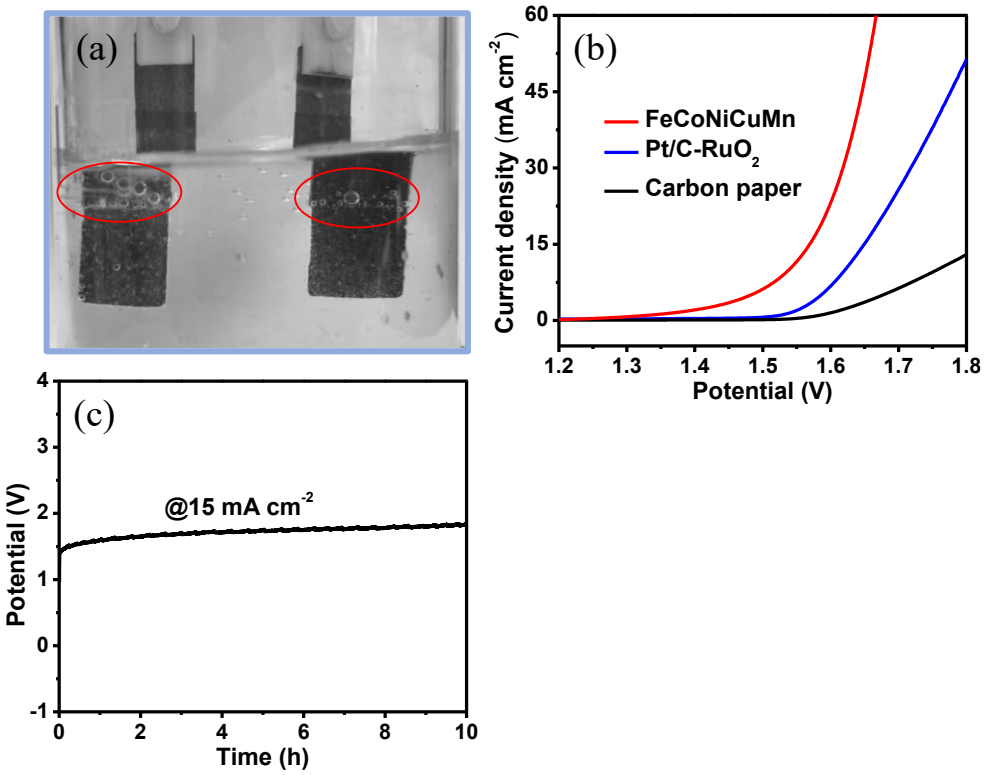

Figure 4.1. (a) Photo of the two-electrode electrochemical water-splitting process of bifunctional NiFeCoMnCu HEAs. (b) LSV of electrochemical water-splitting of NiFeCoMnCu HEAs, Pt/C-RuO_2, and black carbon paper. (c) Potential stability test of electrochemical water-splitting process at 15 mA cm^{-2}.

To evaluate the electrochemical water-splitting capability of NiFeCoMnCu HEAs, the electrochemical water-splitting LSV curve was explored by a two-electrode system in 1.0 M KOH. As shown in Figure 4.1b, the current density of electrochemical water-splitting enabled by bifunctional NiFeCoMnCu HEAs electrocatalyst could be achieved to 10 mA cm^{-2} under the 1.53 V. Furthermore, the activity of electrochemical water-splitting enabled by commercial Pt/C and RuO_2 electrocatalysts for cathode and anode, respectively was also explored as the comparison, which required a huge voltage of 1.62 V to reach 10 mA cm^{-2}. Although the HER overpotential of NiFeCoMnCu HEAs were slightly higher than that of commercial Pt/C electrocatalyst, the

NiFeCoMnCu HEAs with higher OER activity than RuO_2 could enable a more effective electrochemical water-splitting process than that of Pt/C-RuO_2 electrocatalysts, because that the OER with slow kinetics and the complex multistep process was recognized as an important speed-limit step towards electrochemical water-splitting. In addition, the voltage of electrochemical only increased 0.3 V after a 10 h continuous electrochemical water-splitting process at 15 mA cm^{-2}, suggesting the bifunctional NiFeCoMnCu HEAs possessed high activity and ability (Figure 4.1c).

As one of the most abundant natural resources on the earth, electrochemical seawater-splitting is a promised approach to producing hydrogen and oxygen, which is beneficial for creating sustainable development. Optimally, electrochemical seawater-splitting ought to be a process involving HER and OER, which occurs at cathode and anode respectively (Figure 4.2a). However, the existence of aggressive chloride anions (~ 0.5 M) in seawater could restrict the development of electrochemical seawater-splitting and corrode the electrodes. Considering this major problem of seawater, we studied the HER and overall water-splitting activity in an alkaline simulated seawater electrolyte (0.5 M NaCl + 1.0 M KOH). As shown in Figure 4.2b, the NiFeCoMnCu HEAs exhibited outstanding HER activity with an overpotential of 143 mV at 10 mA cm^{-2} in the simulated seawater electrolyte, which was very close to that in the 1.0 M KOH. Some insoluble precipitates such as magnesium hydroxide were formed on the surface of the electrode and poisoned the NiFeCoMnCu HEAs electrode, thus resulting in the decreased HER performance in simulated seawater electrolyte. However, as shown in Figure 4.2c, the overall seawater-splitting process enabled by bifunctional NiFeCoMnCu HEAs electrodes displayed a superior activity to that of Pt/C-RuO_2, which only required 1.79 V to achieve 10 mA cm^{-2}. In addition, the bifunctional NiFeCoMnCu HEAs showed excellent current density stability at 1.8 V with a continuous 10 h electrochemical seawater-splitting process (Figure 4.2d). The aggregations of hydrogen and

oxygen bubbles on the surface of electrodes also demonstrated the high activity of the NiFeCoMnCu HEAs (insert of Figure 4.2d).

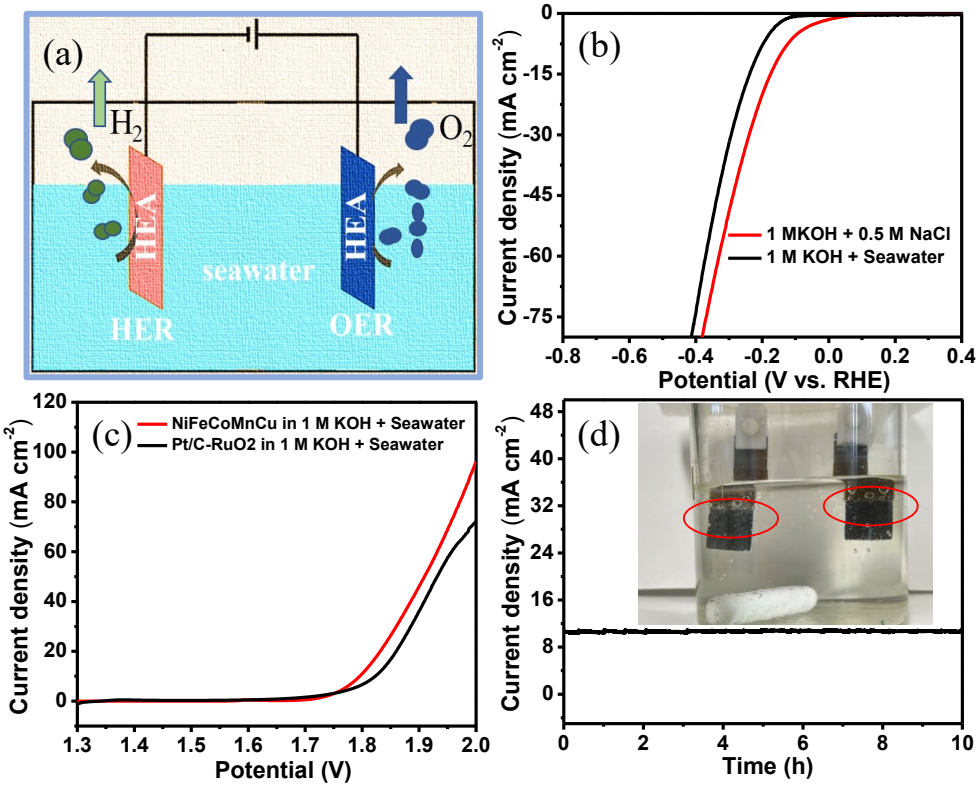

Figure 4.2. (a) The schematic of the electrochemical seawater-splitting process by a two-electrode system. (b) HER LSV of NiFeCoMnCu HEAs in simulated seawater electrolyte and seawater with 1 M KOH. (c) The LSV of electrochemical seawater-splitting by NiFeCoMnCu HEAs and Pt/C-RuO_2. (d) Long-term electrochemical seawater-splitting stability test for NiFeCoMnCu HEAs at an applied potential of 1.55 V; insert: photo of the electrochemical seawater-splitting process by two-electrode system.

4.5 Conclusions

The bifunctional NiFeCoMnCu HEAs electrocatalyst also exhibited more favorable water-splitting activity than that of the Pt/C-RuO_2 electrocatalyst. In addition, a high effective seawater-

splitting process could be also enabled by the bifunctional NiFeCoMnCu HEAs electrocatalyst with excellent stability with a 10 h continuous reaction process. This facile and efficient method could provide a new approach to preparing another high entropy alloy used in the energy conversion field.

References

1. Chen, H.; Zhao, Q.; Gao, L.; Ran, J.; Hou, Y., Water-Plasma Assisted Synthesis of Oxygen-Enriched NiFe Layered Double Hydroxide Nanosheets for Efficient Oxygen Evolution Reaction. *ACS Sustainable Chem. Eng.* **2019,** *7* (4), 4247-4254.

2. Chen, H.; Si, J.; Lyu, S.; Zhang, T.; Li, Z.; Lei, C.; Lei, L.; Yuan, C.; Yang, B.; Gao, L.; Hou, Y., Highly Effective Electrochemical Exfoliation of Ultrathin Tantalum Disulfide Nanosheets for Energy-Efficient Hydrogen Evolution Electrocatalysis. *ACS Appl. Mater. Inter.* **2020,** *12* (22), 24675-24682.

3. Lu, H.; Tournet, J.; Dastafkan, K.; Liu, Y.; Ng, Y. H.; Karuturi, S. K.; Zhao, C.; Yin, Z., Noble-Metal-Free Multicomponent Nanointegration for Sustainable Energy Conversion. *Chem. Rev.* **2021,** *121* (17), 10271-10366.

4. Yu, J.; He, Q.; Yang, G.; Zhou, W.; Shao, Z.; Ni, M., Recent Advances and Prospective in Ruthenium-Based Materials for Electrochemical Water Splitting. *ACS Catal.* **2019,** *9* (11), 9973-10011.

5. Xiong, B.; Chen, L.; Shi, J., Anion-Containing Noble-Metal-Free Bifunctional Electrocatalysts for Overall Water Splitting. *ACS Catal.* **2018,** *8* (4), 3688-3707.

6. Shang, X.; Chi, J.-Q.; Lu, S.-S.; Dong, B.; Li, X.; Liu, Y.-R.; Yan, K.-L.; Gao, W.-K.; Chai, Y.-M.; Liu, C.-G., Novel Co_xS_y/WS_2 Nanosheets Supported on Carbon Cloth as Efficient Electrocatalyst for Hydrogen Evolution Reaction. *Inter. J. Hydrog. Energy* **2017,** *42* (7), 4165-4173.

7. Yu, J.; He, Q.; Yang, G.; Zhou, W.; Shao, Z.; Ni, M., Recent Advances and Prospective in Ruthenium-Based Materials for Electrochemical Water Splitting. *ACS Catal.* **2019,** *9* (11), 9973-10011.

8. Gao, T.; Zhang, Q.; Li, L.; Zhou, X.; Li, L.; Li, H.; Zhai, T., 2D Ternary Chalcogenides. *Adv. Opt. Mater.* **2018,** *6* (14), 1800058.

9. Kong, F.; Ren, Z.; Norouzi Banis, M.; Du, L.; Zhou, X.; Chen, G.; Zhang, L.; Li, J.; Wang, S.; Li, M.; Doyle-Davis, K.; Ma, Y.; Li, R.; Young, A.; Yang, L.; Markiewicz, M.; Tong, Y.; Yin, G.; Du, C.; Luo, J.; Sun, X., Active and Stable Pt–Ni Alloy Octahedra Catalyst for Oxygen Reduction via Near-Surface Atomical Engineering. *ACS Catal.* **2020,** *10* (7), 4205-4214.

10. Jiang, X.; Han, Y.; Zhang, H.; Liu, H.; Huang, Q.; Wang, T.; Sun, Q.; Li, Z., Cu-Fe-Se Ternary Nanosheet-Based Drug Delivery Carrier for Multimodal Imaging and Combined Chemo/Photothermal Therapy of Cancer. *ACS Appl. Mater. Inter.* **2018,** *10* (50), 43396-43404.

11. Amiri, A.; Shahbazian-Yassar, R., Recent Progress of High-entropy Materials for Energy Storage and Conversion. *J. Mater. Chem. A* **2021,** *9* (2), 782-823.

12. Lin, Y.; Massa, W.; Dehnen, S., Controlling the Assembly of Chalcogenide Anions in Ionic Liquids: From Binary Ge/Se through Ternary Ge/Sn/Se to Binary Sn/Se Frameworks. *Chem. Eur. J.* **2012,** *18* (42), 13427.

13. Wu, K.; Yang, Z.; Pan, S., Na_2BaMQ_4 (M=Ge, Sn; Q=S, Se): Infrared Nonlinear Optical Materials with Excellent Performances and that Undergo Structural Transformations. *Angew. Chem. Int. Ed.* **2016,** *55* (23), 6713-6715.

14. Zhang, G.; Ming, K.; Kang, J.; Huang, Q.; Zhang, Z.; Zheng, X.; Bi, X., High Entropy Alloy as A Highly Active and Stable Electrocatalyst for Hydrogen Evolution Reaction. *Electrochim. Acta* **2018,** *279*, 19-23.

15. Liu, J.; Liu, X.; Shi, H.; Luo, J.; Wang, L.; Liang, J.; Li, S.; Yang, L.-M.; Wang, T.; Huang, Y.; Li, Q., Breaking the Scaling Relations of Oxygen Evolution Reaction on Amorphous NiFeP Nanostructures with Enhanced Activity for Overall Seawater Splitting. *Applied Catalysis B: Environmental* **2022,** *302*, 120862.

16. Zheng, J., Seawater Splitting for High-efficiency Hydrogen Evolution by Alloyed PtNix Electrocatalysts. *Applied Surface Science* **2017,** *413*, 360-365.

17. Zhang, Y.; Li, P.; Yang, X.; Fa, W.; Ge, S., High-efficiency and Stable Alloyed Nickel Based Electrodes for Hydrogen Evolution by Seawater Splitting. *Journal of Alloys and Compounds* **2018,** *732*, 248-256.

18. Gayen, P.; Saha, S.; Ramani, V., Selective Seawater Splitting Using Pyrochlore Electrocatalyst. *ACS Applied Energy Materials* **2020,** *3* (4), 3978-3983.

19. Lv, Q.; Han, J.; Tan, X.; Wang, W.; Cao, L.; Dong, B., Featherlike NiCoP Holey Nanoarrys for Efficient and Stable Seawater Splitting. *ACS Applied Energy Materials* **2019,** *2* (5), 3910-3917.
182. Jin, H.; Liu, X.; Vasileff, A.; Jiao, Y.; Zhao, Y.; Zheng, Y.; Qiao, S. Z., Single-Crystal Nitrogen-Rich Two-Dimensional Mo_5N_6 Nanosheets for Efficient and Stable Seawater Splitting. *ACS Nano* **2018,** *12* (12), 12761-12769.
20. Wu, L.; Yu, L.; Zhang, F.; McElhenny, B.; Luo, D.; Karim, A.; Chen, S.; Ren, Z., Heterogeneous Bimetallic Phosphide Ni_2P-Fe_2P as an Efficient Bifunctional Catalyst for Water/Seawater Splitting. *Advanced Functional Materials* **2020,** *31* (1), 2006484.
21. Bigiani, L.; Barreca, D.; Gasparotto, A.; Andreu, T.; Verbeeck, J.; Sada, C.; Modin, E.; Lebedev, O. I.; Morante, J. R.; Maccato, C., Selective Anodes for Seawater Splitting via Functionalization of Manganese Oxides by a Plasma-assisted Process. *Applied Catalysis B: Environmental* **2021,** *284*, 119684.
22. Niu, X.; Tang, Q.; He, B.; Yang, P., Robust and Stable Ruthenium Alloy Electrocatalysts for Hydrogen Evolution by Seawater Splitting. *Electrochimica Acta* **2016,** *208*, 180-187.
23. Yu, L.; Wu, L.; McElhenny, B.; Song, S.; Luo, D.; Zhang, F.; Yu, Y.; Chen, S.; Ren, Z., Ultrafast Room-temperature Synthesis of Porous S-doped Ni/Fe (oxy)hydroxide Electrodes for Oxygen Evolution Catalysis in Seawater Splitting. *Energy & Environmental Science* **2020,** *13* (10), 3439-3446.
24. Ke, S.-C.; Chen, R.; Chen, G.-H.; Ma, X.-L., Mini Review on Electrocatalyst Design for Seawater Splitting: Recent Progress and Perspectives. *Energy & Fuels* **2021,** *35* (16), 12948-12956.
25. Yao, Y.; Gao, X.; Meng, X., Recent Advances on Electrocatalytic and Photocatalytic Seawater Splitting for Hydrogen Evolution. *International Journal of Hydrogen Energy* **2021,** *46* (13), 9087-9100.
26. Li, H.; Tang, Q.; He, B.; Yang, P., Robust Electrocatalysts from an Alloyed Pt–Ru–M (M = Cr, Fe, Co, Ni, Mo)-decorated Ti Mesh for Hydrogen Evolution by Seawater Splitting. *Journal of Materials Chemistry A* **2016,** *4* (17), 6513-6520.
27. Guan, X.; Chowdhury, F. A.; Pant, N.; Guo, L.; Vayssieres, L.; Mi, Z., Efficient Unassisted Overall Photocatalytic Seawater Splitting on GaN-Based Nanowire Arrays. *The Journal of Physical Chemistry C* **2018,** *122* (25), 13797-13802.

28. Li, Y.; Wang, R.; Li, H.; Wei, X.; Feng, J.; Liu, K.; Dang, Y.; Zhou, A., Efficient and Stable Photoelectrochemical Seawater Splitting with TiO_2@g-C_3N_4 Nanorod Arrays Decorated by Co-Pi. *The Journal of Physical Chemistry C* **2015,** *119* (35), 20283-20292.
29. Liu, G.; Xu, Y.; Yang, T.; Jiang, L., Recent advances in Electrocatalysts for Seawater Splitting. *Nano Materials Science* **2020**.
30. Zhang, J.; Hu, W.; Cao, S.; Piao, L., Recent Progress for Hydrogen Production by Photocatalytic Natural or Simulated Seawater-splitting. *Nano Research* **2020,** *13* (9), 2313-2322.
31. Wang, C.; Shang, H.; Jin, L.; Xu, H.; Du, Y., Advances in Hydrogen Production from Electrocatalytic Seawater splitting. *Nanoscale* **2021,** *13* (17), 7897-7912.

General conclusions and prospects

Hydrogen with high energy density could be recognized as a perfect energy source, which is green and sustainable. Up to now, the methods of producing hydrogen for industrialization are deeply depended on the preservation of fossil energy, such as the pyrolysis of fossil oil and Methanol hydrogen. Among these methods, the shortage of fossil energy and environmental pollution limit the long-time development. Recently, hydrogen evolution from electrochemical water-splitting received great attention, which is high efficiency and sustainable development. However, the most effective electrocatalysts of OER and HER are precious metals, such as Ru, Ir, Pt. The high price and rare reserve on the earth limit them for large-scale usage. Transition metals have properties of low-cost, various variety, and high electrocatalytic activity, which had been widely used for the HER and OER catalysts. However, the transition metal electrocatalyst with bifunctional electrocatalytic activity is few reported and rarity. Multimetallic electrocatalysts could satisfy the requirement of the bifunctional electrocatalytic activity, which possess OER and HER activity by chelating different active metal elements. Therefore, developing multimetallic electrocatalyst is promised a prospective approach to prepared high effective and low-cost catalysts toward electrochemical water-splitting reaction.

Firstly, a bimetal heterojunction Fe_xS_y/WS_2 Ns with petal-like structure were prepared by hydrothermal method. The prepared petal-like Fe_xS_y/WS_2 Ns had a large diameter size of ~1 μm and thickness of 8 nm. The developed Fe_xS_y/WS_2 Ns exhibited excellent HER activity with overpotential of 118 mV at 10 mA cm^{-2} and a low Tafel slop of 87 mV dec^{-1} in 0.5 M H_2SO_4, which is much better than that of single Fe_xS_y and WS_2 (> 420 mV at 10 mA cm^{-2}). This advanced HER activity owned to the unique thin structure and more exposed active sites provided by defects

between crystal interface of Fe_xS_y and WS_2. Furthermore, the Fe_xS_y/WS_2 Ns as bifunctional electrocatalyst could achieve energy-saving water-splitting by replacing oxygen evolution reaction of urea oxidation reaction to decrease the applied voltage of 147 mV.

Secondly, a quinary metal NiFeCoMnCu high entropy alloys (HEAs) were synthesized by a facile citric acid chelating method. The prepared NiFeCoMnCu HEAs possessed an fcc single-phase structure and dispersed uniformly on the carbon structure with a diameter size of ~ 80 nm. Benefiting from the high-entropy effect, the NiFeCoMnCu HEAs exhibited outstanding oxygen evolution reaction (OER) and hydrogen evolution reaction (HER) activity with an overpotential of 240 mV and 165 mV at 10 mA cm^{-2} in 1.0 M KOH, respectively. The enhancement of electrocatalytic activity with the sequence of increasing metal species number demonstrated that the synergy effect between metal elements in HEAs resulted in the excellent activity.

Thirdly, the quinary NiFeCoMnCu HEAs as the bifunctional electrocatalyst exhibited superior water-splitting performance with a low 1.53 V to reach 10 mA cm^{-2}, which was much lower than that of Pt/C-RuO_2 electrocatalyst (1.65 V). In addition, the bifunctional NiFeCoMnCu HEAs electrocatalyst also enabled a highly effective and stable seawater-splitting process with 10.5 mA cm^{-2} at 1.8 V for 10 h.

In summary, the developed multimetallic electrocatalysts exhibited outstanding electrocatalytic activity toward HER and OER, which was attributed to the various active metal species. Experiments had confirmed that the synergy effect between different metal element play important role for increasing conductivity, promoting electrocatalytic activity and exposing more active sites. In addition, the prepared bifunctional electrocatalysts also enable a high effective electrochemical water-splitting process with high stability for 10 h continuous reaction. Moreover,

a stable seawater-splitting reaction could also be enabled by the prepared bifunctional electrocatalysts.

Prospects

Hydrogen evolution form the electrochemical water-splitting is significant for the developing green and suitable energy source. Especially the seawater-splitting technology also provides positive opportunity for generating hydrogen at arid area. The developed multimetallic electrocatalysts with properties of high efficiency and low-cots will be expected to promote the development of hydrogen on the whole world. In addition, the concept of chelating different active metal element will also provide new sight to design multifunctional electrocatalysts. This is also the point we will focus on in the future.

Achievements

Publications

1. **Hanlin Chen**, Yanqiang Li, Huiyong Huang and Tingli Ma, Petal-like Fe_xS_y/WS_2 Heterojunction Nanosheets as an Electrocatalyst for Highly Effective Hydrogen Evolution Reaction, Energy & Fuels, 36, 9, 4888-4894, 2022. DOI: 10.1021/acs.energyfuels.2c00483.
2. **Hanlin Chen**, Qiaoling Kang, Huiyong Huang and Tingli Ma, Direct Synthesis of Catalytically NiFeCoMnCu High Entropy Alloys for Highly Effective overall Water-Splitting, Chemical Engineering Journal, Under view.

Conference

1. **Hanlin Chen**, Tingli Ma and Yanqiang Li, Petal-like Fe_xS_y/WS_2 Heterojunction Nanosheets as Electrocatalyst for Highly Effective Hydrogen Evolution Reaction, The 89^{th} Electrochemical Society of Japan (JSEC), March 2022.

Acknowledgements

It's the third time to write the acknowledgement. I would like to express my lofty respect to my supervisor, Professor Tingli Ma. The professional knowledge and earnest work of Prof. Ma impressed me deeply. During the past three years, Prof. Ma given me innumerable and valuable assistances, which not only include the scientific advice in experiment, but also the meticulous care in the daily life. The conscientious attitude and dedicated spirit form Prof. Ma will always inspire me in the future.

Meanwhile, I would be grateful to the help and valuable comments from the Prof. Shuzi Hayase, Prof. Sham S. Pandey, and Prof. Naoya Murakami.

In addition, I would to thanks for my classmates and graduates in Ma lab. They given me great help in experiment and daily life, which help me to finish the doctor program favorably.

Moreover, I would like to thank for my families, who provide me the integral support. Thanks for the help form my friend Along Liu. Particularly thanks for my girlfriend, Min Zou, who encouraged me and accompanied me to get through it all.